UNIVERSITÀ DEGLI STUDI DI BARI
DIPARTIMENTO INTERATENEO DI FISICA
"Michelangelo Merlin"

DOTTORATO DI RICERCA IN FISICA XXXI CICLO
Settore Scientifico Disciplinare FIS-01

Development of a beam monitor for the calibration of Super-Kamiokande

Dottorando:
INTONTI Rosaria Annalisa

Supervisori:
Prof. BERARDI Vincenzo
Dott. RADICIONI Emilio

Coordinatore:
Prof. IASELLI Giuseppe

ESAME FINALE 2020

Alla mia famiglia di origine
e a quella che mi sono creata
con Michele, Gaetano…
e Francesca… che sta arrivando!!!

Contents

Introduction

The research activity of my PhD program was carried out as part of the T2K-SK experiment, a "long baseline" neutrino oscillation experiment that aims to measure the oscillation parameters. In T2K an almost pure beam of ν_μ with 600 MeV/c peak energy is produced in the research accelerator complex, called J-PARC (Tokai village on the east coast of Japan); after being sufficientely characterized by a set of detectors placed in the so-called Near Detector (ND280) in order to measure the flow of neutrinos before the oscillation process takes place, it is subsequently intercepted at a distance of 295 km by the Super-Kamiokande detector . The latter is located in Japan in the Kamioka mine (the current name from the city is Hida), an inactive zinc mine within Mount Ikenoyama. Its stainless steel tank, 41 meters high and with a diameter of 39.3 meters, contains 50,000 tons of ultra pure water, so transparent that the light must cross about 70 meters before losing half its intensity. The inner part has a volume of about 32 kton (22 ktons fiducial) and it is surrounded by approximately 11129 PMTs with a diameter of 50 cm, which cover about 40% of the surface: the photomultipliers record the Cherenkov light produced by the secondary particles of the interactions between a neutrino and water.

From the incidence time on the wall of PMT (the temporal resolution is a few ns) it is possible to reconstruct the interaction vertex of and the particles direction while the total number of photoelectrons makes it possible to trace its energy.

The external part has a mass of about 18 kton and is equipped with 1885 PMT with a diameter of about 20 cm that look outwards: it works as a screen and veto for environmental radioactivity and allows to identify cosmic rays and muons produced by neutrino interactions outside the detector or those events that are not completely contained within the fiducial volume.

The possibility to measure the direction and energy of the neutrino at energies

lower than 20MeV is heavily limited in the Cherenkov's Water, due to the Coulomb multiple scattering. An accurate calibration of the detector in this energy range is therefore fundamental.

The Super-Kamiokande (SK) detector, described in the chapter 2 is sensitive not only to the interactions of neutrinos coming from JPARC, but also to those generated for example inside the sun and/or by SuperNovae. In particular, with a threshold set near 3.5 MeV, SK is currently the largest and most sensitive observatory to these phenomena. This reason why the calibration response to electrons generated by the interactions of neutrinos with an energy in 5-20 MeV range, is particularly important for its impact on these measures.

The calibration response to electrons in Super-Kamiokande, is carried out periodically thanks to a LINAC that accelerates known energy electrons in predetermined positions in the water volume. It is necessary to rebuild these electrons position while evaluating the corresponding energy resolution obtained. Unfortunately, the current system suffers from many limitations due both to the insufficient precision in aligning and steering of the electron source beam, and to the long times required to obtain it. As part of my thesis activity I took part to the latest calibration campaigns carried out with the current system (ch.3).

Since a typical campaign expects to use different energy values and numerous positions, it takes a long time as well as heavy work: for example, the one in the summer of 2017 required four weeks of data collecting during which the SK could not gather data in optimal conditions. Many of the elements the LINAC is made of, such as some collimators, are located near the so-called outer detector, an essential element that helps to define which events are completely contained in the fiducial volume; the beam scraping on the collimators generates a background noise of X radiation that is considered excessive. This forces SK to operate in a reduced configuration with the outer detector off. This configuration prevents the measurement of the higher energy neutrino interactions with the

usual efficiency, including atmospheric interactions and makes it virtually impossible to record data with the T2K beam. For this reason, calibrations with the LINAC are always carried out during beam shutdown periods.

So far, for all these reasons, calibration campaigns have been few and on average separated over time by at least 2 years. Specifically in this context, my research activity includes not only the study and active participation, in the current detector calibration procedures, but at the same time the simultaneous development of a new LINAC monitor for Super-Kamiokande (responsibility of the INFN group). By introducing the use of beam monitors with position measurement, the steering of the beam can be fast and accurate, these are fundamental conditions to obtain an optimal calibration of the electron response in the detector by solving the current limitations and particularly by considerably shortening the time required.

During the activity work of my PhD, I carried out the analysis of the data recorded during the calibration campaign I took part in and, at the same time, I developed further new simulation codes for the monitor we are building and that will be installed in Super-Kamiokande, finalizing the design which has been studied with all the optimal parameters required (ch.4).

Chapter 1

Neutrinos are suspected to be the second most abundant particle in the universe (after photons) and yet remain some of the most elusive: the neutrino physics is one of the most important field of particle physics. The following sections will cover the development of neutrino physics starting from the neutrino discovery to the current and future generation of neutrino experiments. It will also be discussed the inclusion of neutrino masses in the Standard Model and the neutrino oscillation phenomenon.

1.1. A brief neutrino's history

The existence of the neutrino was first postulated by Wolfgang Pauli in 1930: he proposed a solution to explain the continuous spectrum of β decay and the problem of spin of some nuclei.

In the β-decay of a nucleus (A, Z), the process can occur via electron emission in the nuclear transition (A, Z) -> (A, Z + 1)+e^-.

If (A, Z) decays in the rest frame, according to the conservation energy law of a two body decay, the energy of the emitted electron should have a fixed value. Instead, a continuous electron energy spectrum, peaked at energy E_e^{Max} was experimentally observed, extremely close to the predicte E_e-, as in figure 1.1:

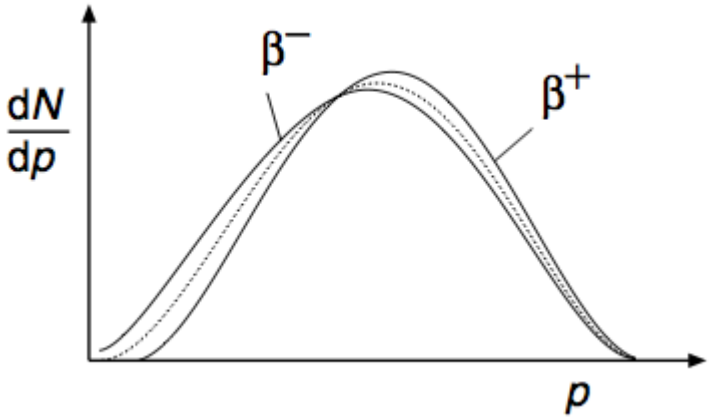

Fig. 1.1: Schematic appearance of the electron spectrum in β-decay.

Pauli understood that, under the condition of energy-momentum conservation, the only possibility to explain the continuous β-spectra, was to assume the existence of a new, neutral particle which was emitted with the electron, not detected in the experiment. Pauli inferred that this particle should be: electrically neutral (in order to conserve charge), with spin 1/2 to conserve angular momentum and weakly interacting. Finally, it is needed that this new particle has a mass lighter than the electron and called the new particle "neutron". Enrico Fermi developed this idea in 1934 and built the first theory of the β-decay of nuclei, based on Pauli assumption. In particular, Fermi's theory assumed that nuclei are bound states made of proton and neutrons. Fermi explained the β-decay process as the electron-proton scattering with the assumption that the electron-neutrino pair is produced in the quantum transition of a neutron in a proton (Figure 1.2) [1].

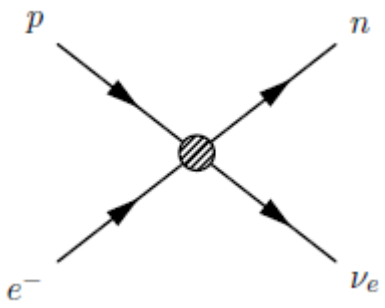

Fig. 1.2: Fermi's explanation of β-decay.

Today we know that β-decay occurs with the exchange of the intermediate boson W, and the Fermi theory is the low energy limit of this process.

Due to the elusive nature of the neutrino, it took another twenty-five years before the first neutrino was actually observed by Frederick Reines and Clyde Cowan of the Los Alamos National Laboratory, who, in 1955 discovered the electron anti-neutrino observed in $\bar{\nu}_e$+p->e^++n at the Savannah River reactor[2]. In 1957, Bruno Pontecorvo proposed the idea of neutrino oscillations between neutrinos and antineutrinos [3] to explain the missing neutrinos: Pontecorvo had suggested that neutrinos could oscillate between flavor (described in 1.2) states as they propagate, thereby reducing the electron neutrino flux at the Earth but maintaining the total neutrino flux. Pontecorvo had even suggested that "from the point of view of [neutrino oscillation] detection possibilities, an ideal object is the sun". In 1962 Z. Maki, M. Nakagawa and S. Sakata formulated the theory for neutrino flavor oscillation [4]. which combined with the theory of matter effects on neutrinos proposed by Mikheyev, Smirnov and Wolfenstein (the so-called MSW effect) could account for the observed discrepancies in the solar neutrino flux.

In 1998 the Super-Kamiokande (SK) [5] experiment provided evidence for neutrino oscillations, when it detected a disbalance between up-going muons neutrinos, produced by neutrinos with a longer flight length through the Earth, in comparison to down-going muons neutrinos. Looking at the zenith angle it was possible to reconstruct the path distance travelled by the neutrinos from the production in the upper atmosphere to the detection point. The deficit showed a dependence in this distance that could be explained by the theory of neutrino oscillations.

In 2001 the SNO experiment measured the flux of all the 3 flavours of neutrinos and found results consistent with the prediction of the Standard Solar Model [6].

In conclusion, neutrinos are fermions belonging to the lepton sector of particles and are electrically neutral, naturally produced neutrinos originate from cosmic ray

interactions in the atmosphere and pp and CNO (the carbon nitrogen oxygen cycle) reactions in the Sun (as well as all other stars, including supernovae and relic neutrinos from the formation of the universe). They are also produced in beta decays, in nuclear reactors and at accelerators and thanks to the discoveries of the last years, that established the existence of neutrino oscillations, started the contemporary neutrino oscillation experiments era.

1.2. Neutrino mass

The Standard Model (SM) is the theory that has unified the weak and electromagnetic interactions and this theory was developed in the middle of the 20th century.

The Standard Model (SM) of Particle Physics is one of the most successful theories in science, explaining a number of observed experimental results at its inception and making precise predictions that were later confirmed. According to the Standard Model (SM), there are three "flavors" of neutrino, named after its charged lepton counterparts: electron (e), muon (μ) and tau (τ), each with their equivalent anti-particle. The flavor states $|\nu_\alpha\rangle$, are superpositions of mass eigenstates $|\nu_k\rangle$:

$$|\nu_\alpha\rangle=\sum_i U_{\alpha k}|\nu_k\rangle \text{ , } (\alpha= e, \mu, \tau), (k = 1; 2; 3)$$

where $U_{\alpha k}$is the unitary mixing matrix defined in 1.3.1.

The key ingredient of the SM is the symmetry breaking, usually called Higgs mechanism. Such a process is responsible for the bosons masses, whose values are related to the Weinberg angle ϑ_W, and the Fermi constant G_F. In the case of quarks and leptons, this mechanism is also responsible for their masses, but it does not provide their value. In particular, in the case of the ν, the SM model can not predict their masses.

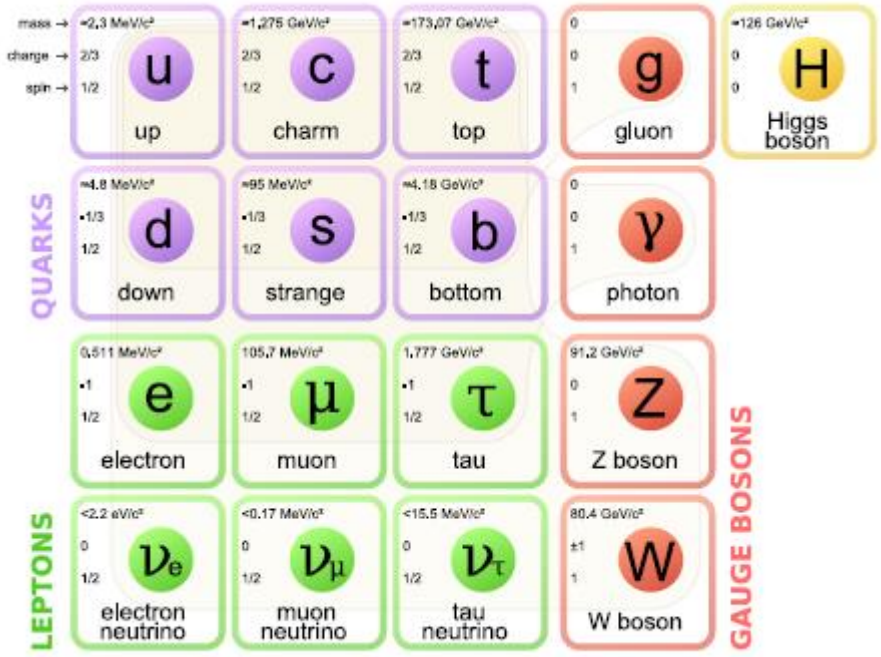

Fig. 1.3 Electroweak Standard Model scheme after symmetry breaking

The neutrino mass was experimentally known to be small. The observation suggests that neutrinos are massless, and the results of any direct mass measurements to date by precision kinematic measurement of various weak decay processes are consistent with zero mass. However, the discovery of neutrino oscillations has proven that neutrino mass is, in fact, not zero, which contradicts the assumption made in the Standard Model in which neutrinos are massless.

However neutrino masses can be introduced into the theory by the use of two mechanisms: the Dirac and Majorana mechanisms.

In the Dirac mechanism, the neutrino mass is introduced in the SM via the Higgs mechanism [7], [8], identically to the quark and charged lepton mass origin process, in the Majorana mechanism, the neutrinos can be identified with its own antiparticle since they have no charge.

The question about the neutrino's nature, Majorana or Dirac, is currently a subject of an intense experimental investigation. Both mechanisms diverge only for the case of massive neutrinos, which has been proven by the measurement and discovery of ν oscillation phenomenon that is described in the next section.

However the kinematic effects for Dirac and Majorana neutrinos are the same and thus, as a consequence, can not be searched for through the neutrino oscillations directly.

The neutrino mass eigenvalues are significantly smaller than those of other elementary particles including the other fermions from the same generation. The absolute values of neutrino masses have not been measured yet, however the upper limits have been determined and are shown in Table 1.1.

Neutrino Flavour	Upper Mass Limit	Experimental Method
$\overline{\nu}_e$	2 eV	Tritium
ν_μ	0.19 MeV	π decay at rest
ν_τ	18.2 MeV	τ decay

Tab.1.1 Measurements of neutrino upper mass limits from the Particle Data Group (PDG)

The electron neutrino mass limit was determined using-decay and gave the result of $m_{ve} < 2$ eV at a 95% confidence level. The muon neutrino mass was measured from charged pion decay to be $m_{v\mu} < 190$ keV at a 90% confidence level. The lowest precision up to date has been achieved in assessing the tau neutrino mass. The tau neutrino mass is currently less than 18.2 MeV at a 95% confidence level.

The fact that the mass eigenstates are different from the flavor eigenstates can lead to neutrino flavor changes $\nu_\alpha \leftrightarrow \nu_\beta$. In the case of a coherent superposition of the mass eigenstates, the flavor of the neutrino can change as a function of the distance. This is called neutrino oscillation. Oscillation is then possible, if neutrinos, in a certain flavor state, are a linear superposition of mass eigenstate (ν_1, ν_2, ν_3) with definite masses (m_1,m_2,m_3) different from the mixed one, with mass differences smaller than the typical quantum uncertainty in the process, as realized by Pontecorvo, Maki, Nakagawa, and Sakata[9].

There is now an overwhelming body of evidence that neutrinos have a small but non-zero mass [10,11,12,13,14]. This evidence comes from observations of flavour

change in neutrinos produced in nuclear reactions in the Sun, cosmic ray interactions in the atmosphere, and in man-made accelerator-based neutrino beams and nuclear reactors. Neutrinos produced in the atmosphere and from man-made sources have been shown to change flavour as a function of their production flavour, energy, and the distance travelled between production and observation.

1.3. Neutrino Oscillation

1.3.1 Neutrino Oscillations in Vacuum

The idea that neutrinos oscillate was first proposed separately by Pontecorvo and by Maki, Nakagawa and Sakata. In the 1960's and was later a good explanation for the disappearance of both solar and atmospheric neutrino observed by several experiments. Neutrino oscillation relies on the fact that the mass eigenstates are not identical to the flavor eigenstates.

Neutrino oscillations occur because the three flavour eigenstates, ν_e, ν_μ, ν_τ , are not the same as the energy, or propagation, eigenstates, ν_1, ν_2, ν_3. The relationship between the two bases is contained in the Pontecorvo-Maki-Nakagawa-Sakata matrix, $\mathbf{M}_{PMNS}$, and can be expressed as:

$$\begin{pmatrix} \nu_e \\ \nu_\mu \\ \nu_\tau \end{pmatrix} = \begin{bmatrix} U_{e1} & U_{e2} & U_{e3} \\ U_{\mu 1} & U_{\mu 2} & U_{\mu 3} \\ U_{\tau 1} & U_{\tau 2} & U_{\tau 3} \end{bmatrix} \begin{pmatrix} \nu_1 \\ \nu_2 \\ \nu_3 \end{pmatrix}$$

In other words, this mixing of states means that a neutrino created in some flavour state and observed sometime later will have a finite chance of being measured as a different flavour state.

This 3×3 unitary matrix can be expressed in terms of three real angles, θ_{12}, θ_{13}, θ_{23}, and one phase, δ_{CP}. The phase factor is associated with two discrete symmetries: charge conjugation C that changes particles to antiparticles and parity P which

reverses the spatial components of the wave function. P flips the direction of the particles but not the spin, hence the particle handedness is transformed.

This matrix can be parameterised as:

$$\mathbf{M}_{\text{PMNS}} = \begin{bmatrix} 1 & 0 & 0 \\ 0 & C_{23} & S_{23} \\ 0 & -S_{23} & C_{23} \end{bmatrix} \begin{bmatrix} C_{13} & 0 & S_{13}\, e^{-i\delta_{CP}} \\ 0 & 1 & 0 \\ -S_{13}\, e^{+i\delta_{CP}} & 0 & C_{13} \end{bmatrix} \begin{bmatrix} C_{12} & S_{12} & 0 \\ -S_{12} & C_{12} & 0 \\ 0 & 0 & 1 \end{bmatrix},$$

where $C_{ij} = \cos \theta_{ij}$ and $S_{ij} = \sin \theta_{ij}$ and θij is the mixing angle between the i and j mass states. This parametrisation neatly splits the PMNS matrix into three rotations, which can be roughly associated with the neutrino sources that can be used to measure them.

Explicitly, atmospheric and beam neutrinos provide sensitivity to θ_{23}, beam and reactor neutrinos are used to measure θ_{13}, and solar neutrinos probe θ_{12}. These associations are due to the leading term in the neutrino oscillation probability in each case but this is not the only factor that determines the sensitivity of individual experiments. The ratio of an experiment's baseline to the energy of the observed neutrinos and the mass squared splitting between the two neutrino states govern the oscillation probability, which will ultimately determine the sensitivity of the experiment to both the dominant and sub-dominant mixing angles.

The factor δ_{CP} is related to the charge-parity (CP) symmetry in the lepton sector. It can be demonstrated that if $\delta_{CP} \neq 0$, CP is not conserved.

As for all fermions and taking into account the PMNS matrix, the wave function of a neutrino in the flavor eigenstate α can be written as:

$$\psi_{\alpha}(\bar{x},t) = \sum_i U_{\alpha i}\, e^{-ixp_i}\, \nu_i = \sum_i U_{\alpha i}\, e^{i\bar{x}p_{\nu} - itE_i}\, \nu_i .$$

Since the masses of the neutrinos are very small,

$$Ei \approx p\nu + \frac{m_i^2}{2p_\nu}$$

therefore:

$$\psi_\alpha(\bar{x},t) = e^{(x-t)ip_\nu} \left(\sum_i U_{\alpha i}\, e^{-\frac{m_i^2}{2p_\nu}}\right)\nu_i .$$

A neutrino produced at the source at a time t = 0 will evolve following the Schrödinger equation. So that after a time t and a distance travelled L, there is a non-zero probability of finding the neutrino in a different flavour eigenstate.

Assuming that a neutrino of flavor α is traveling at the speed of light c for a distance L, we can write its probability to be in a flavor eigenstate β at time t as:

$$P(\nu_\alpha \rightarrow \nu_\beta) = \left|\sum_i U_{\alpha i} U^*_{i\beta}\, e^{-\frac{i m_i^2 t}{2p_\nu}}\right|^2$$

The probability of a neutrino oscillating from a neutrino of flavour α to a neutrino of flavour β, in a vacuum, occurs according to the formula:

$$P(\nu_\alpha \rightarrow \nu_\beta) = \sin^2 2\vartheta \sin^2\left(\frac{\Delta m_{\alpha\beta}{}^2 L}{4E}\right)$$

where $\Delta m_{\alpha\beta}{}^2 = m^2_{1\alpha} - m^2_{2\beta}$ (1 and 2 indicate the mass eigenstates), E and L are the neutrino energy and the distance from where the neutrino is produced to its detection point, respectively. While Δm^2 and ϑ are the physical parameters that we want to measure, E and L depend on the experiment performed.

1.3.2 Neutrino Oscillations in Matter

Matter effects can greatly affect the probability of neutrino oscillations: neutrinos that travel throuth the matter can interact with the particles along their way, and this interactions are able to modify their propagation.

Up until now, neutrinos have been considered as propagating without disturbance from matter, but in reality most neutrino experiments involve neutrinos

propagating through the Earth. This can make a substantial difference to neutrino oscillation physics.

In particular, when neutrinos travel through matter, their propagation is modified by the coherent forward scattering from particles they encounter, consequently changing their oscillation probability[15].

By considering this extra-potential, we obtain an oscillation probability that is dependent on the mass hierarchy. The oscillation probability from ν_μ to ν_e in accelerator experiments is expressed, to first order in the matter effect, as the sum of five terms:

$$P(\nu_\mu \rightarrow \nu_e) = T_{leading} + T_{CPC} + T_{CPV} + T_{solar} + T_{matter}$$

where $T_{leading}$ is the leading term, T_{CPC} is the CP conserved term, T_{CPV} is the CP violating term, T_{solar} is the CP solar term, and T_{matter} is the matter term.

This is of the same form as equation for vacuum but the original mixing angle and the mass splitting ϑ and Δm^2 are now replaced by the effective values in matter ϑ_M and Δm^2_M. This is the matter effect, and the oscillation amplitude and the frequency are changed from the case in vacuum due to the particular interactions with matter shifting the energy levels.

Neutrinos are electrically neutral and colorless (color is the charge associated to the strong interactions), so they do interact neither via electromagnetic interactions, nor via strong interactions. Neutrinos can only interact via weak interactions. There are two type of weak interactions: Charged Current (CC) and neutral current (NC) interactions.

Neutrino oscillations are a quantum mechanical phenomenon that may be observed over large distances, even astronomically large. In such cases, neutrinos pass through a significant amount of medium, electrons and nucleons, which results in a modification of the oscillation probability.

This is called the matter effect and it occurs due to the neutrino neutral current (NC) and charged current (CC) coherent forward elastic weak scattering. The NC scattering can appear for every flavor, however the CC scattering affects only the electron flavor as matter consists of e, but not μ and τ.

In figure 1.2, theese both mechanisms for neutrinos to interact without the neutrino converting into a charged lepton: neutral-current scattering from an electron, proton or neutron or charged-current scattering of an electron and a neutrino:

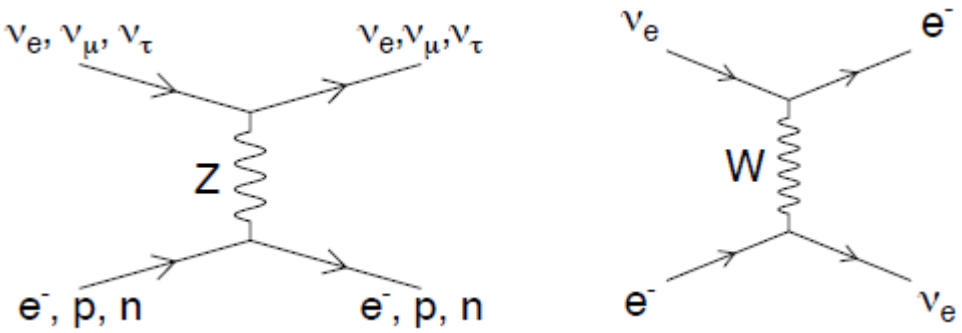

Fig. 1.2 Feynman diagrams of the neutrino forward elastic scattering for the neutral current interaction (left) through Z exchange, and charged current interaction (right) through W exchange.

1.4. Neutrino oscillation experiments

Neutrinos were created at the beginning of the Universe and they fill the entire space, similarly to the microwave background (relic neutrinos). Additionally, they are produced in the celestial bodies, the Earth's atmosphere and man-made machines such as nuclear reactors or accelerators. The neutrino cross sections are distinctively small and as a consequence they can travel long distances through matter without interacting, unlike other particles. Therefore, the message they carry contains important information about the sources that produce them, even the most distant. This can be achieved by examining neutrino phenomena such as the oscillation of neutrino flavours or the charge parity (CP) violating phase in the

leptonic sector, which is thought to help explain the matter-antimatter asymmetry in the Universe.

Current neutrino oscillation experiments can use sources of neutrinos that are natural (solar and atmospheric experiments) or artificial (reactor and accelerator experiments).

1.4.1. Solar experiments

The first experiments to prove the existence of solar neutrinos were Homestake [15], SAGE [17] and GALLEX [18], Super-Kamiokande [19], SNO [20] and they are most sensitive to ϑ_{12} and Δm^2_{21}.

Solar experiments detect low energy (in the MeV scale) ν_e produced in nuclear reactions in the core of the sun.

The Sun is the most powerful neutrino source. The energy source of the Sun light is a fusion reaction in the center of the Sun. Four hydrogen nuclei (i.e. protons) form a helium-4 nuclei (two protons and two neutrons) via the fusion reaction, in which fusion energy, two positrons and two electron neutrinos are also released.

$$4p \rightarrow He + 2e^+ + 2\nu_e + \text{fusion energy}$$

The electron neutrinos generated in this reaction are called as "solar neutrinos". The solar neutrino flux, on the Earth, per one second, per one square centimeter, is about 66 billion.

Observation of solar neutrinos begun with Homestake experiment by R. Davis and so on from the late 1960s in US. In the Homestake experiment, solar neutrino flux was measured via the production rate of argon atoms from the neutrino reaction of chlorine atoms. It was impossible to measure the neutrino direction.

The Standard Solar Model (SSM) [21] predicts that the solar flux contains neutrinos with energies up to 30 MeV, which majority is below 0.4 MeV. As a results of the experiment, the observed production rate was about 1/3 of the

expected value from Standard Solar Model (SSM). This problem was called as "solar neutrino problem". In 1988, the solar neutrino results other than the Homestake experiment was firstly reported from the Kamiokande experiment group. Kamiokande, which was the former experiment of Super-Kamiokande, was able to measure neutrino coming direction in real time. It was firstly shown by Kamiokande that the observed neutrinos were coming from the direction of the Sun. However, the observed solar neutrinos flux was about half of the expected value from SSM. Therefore, the solar neutrino problem still remained.

In June 2000, Super-Kamiokande has reported the observation result of the solar neutrino flux with a highest accuracy than ever before. As a result, the observed solar neutrino flux was about 45% of the expected flux in SSM with more than 99.9% confidence level, suggesting the solar neutrino problem was caused by a neutrino oscillation. Furthermore, measuring energy distribution of solar neutrinos and time variation of the solar neutrinos in day time and night time with high accuracy, a large limit on the neutrino oscillation parameter (mass difference and mixing angle) area was obtained. It was also shown that the mixing between neutrinos are large. In June 2001, a combined analysis of solar neutrino observations between Super-Kamiokande and SNO experiment in Canada, showed a reliable evidence that a neutrino oscillation really occurred. In addition, it was confirmed at the same time that the neutrino flux calculated from SSM was correct. Although the problem that observed solar neutrino flux looked smaller than SSM was solved by neutrino oscillation, there are still unsolved questions in nature of neutrinos or the burning mechanism of the Sun (SSM). For example, they are true values of the solar neutrino oscillation parameters (mass difference and mixing angle), confirmation of the Earth's matter effect on solar neutrinos, elucidation of the chemical composition of the solar interior, and so on.

1.4.2. Atmospheric experiments

Atmospheric experiments detect the neutrinos produced by the interactions of cosmic rays with nuclei in the upper atmosphere. Decays of pions, kaons, muons and electrons produce respectively ν_μ , $\bar{\nu}_\mu$, ν_e and $\bar{\nu}_e$ at energies from MeV to TeV. Super- Kamiokande and MINOS [22] are examples of atmospheric neutrino experiments that are mainly sensitive to ϑ_{23} and Δm^2_{32}: these parameters are called the "atmospheric" parameters as initially they were determined from the observation of the neutrinos produced by cosmic rays in the Earth's atmosphere.

Cosmic rays are a radiation of high energy particles arriving at the Earth from the Universe. In the GeV/nucleon energy region, these cosmic-ray particles are mostly protons, about 5% are Helium nuclei and a still smaller fraction of heavier nuclei. Electrons and photons also compose a part of the cosmic rays. However, a proton entering the atmosphere produces a shower of hadrons which produce pions, which decay to produce neutrinos via the following reactions: a π^+ decays to a muon (μ^+) and a ν_μ. The produced muon (μ^+) is also unstable and decays to a positron (e^+), a $\bar{\nu}_\mu$ and a ν_e. A similar decay processes occur for π^- and K mesons. In this way, neutrinos are produced when a cosmic-ray particle enters an atmosphere. These neutrinos are called atmospheric neutrinos[23].

The ratio consequential to the above reactions can be written as:

$$R=\frac{\nu_\mu+\bar{\nu}_\mu}{\nu_e+\bar{\nu}_e}$$

and is expected to be 2 at moderate energies (the spectrum peak is at 1 GeV).

However, the Super-Kamiokande experiment, along with other experiments, measured a lower value which was known as the Atmospheric Neutrino Anomaly.

Additionally, SK analysed the direction of incoming neutrinos and observed a large deficit of up-going muons neutrinos, produced by neutrinos with a longer

flight length through the Earth, in comparison to down-going muons neutrinos. This was explained in the context of neutrino oscillations hypothesis and was an evidence of ν_μ disappearance. Later, this measurement was confirmed by the accelerator generated neutrino experiments.

1.4.3. Accelerator experiments

In accelerator experiments neutrinos are produced via the same reactions as in the atmosphere. The main difference is that the energy and kinematics of the particles within the focused beam can be controlled in the accelerator experiments. The typical energy of accelerator neutrinos is of the order ~ GeV.

Long baseline accelerator experiments, like MINOS, T2K and NOνA [24] use GeV muon neutrinos produced by pion decay in an accelerator complex and consist of a far detector, positioned close to the oscillation maximum, and a near detector, positioned just after the neutrino beam production point, to constrain the properties of the neutrino beam. These experiments are mostly sensitive to ϑ_{13}, ϑ_{23} and Δm^2_{32}.

As already mentioned, the probability of neutrinos having oscillated away from their original flavour state depends on their energy and distance travelled. Modern accelerator-based long baseline neutrino oscillation experiments, such as T2K and NOνA, exploit this by utilising a proton accelerator to produce a - predominantly muon- neutrino beam spread over a few GeV neutrino energy and observe the change in the flavour composition of the beam over a few hundred kilometres, where neutrino oscillations are maximal.

In general, neutrino oscillation experiments detect the products of the neutrino interactions, and therefore it is fundamental to understand neutrino interactions to infer any neutrino property.

Future experiments, like Hyper-Kamiokande [25] and DUNE [26], could also lead to the measurement of δ_{CP} : it is difficult to measure a δ_{CP} phase as it requires the mixing angles to be determined with a high precision. Otherwise, the current

uncertainties associated with the oscillation parameters measurement would cover the effects of δ_{CP}.

However, the nearest future experiments have the relevant sensitivity and required accuracy to evaluate the phase factor based on the groundwork of current generation experiments.

1.4.3.a The T2K experiment

T2K (Tokai To Kamioka) [27] is a long-baseline neutrino oscillation experiment which aims to characterise the mixing of muon neutrinos with other neutrino flavours. T2K consists of a predominantly muon (or antimuon) neutrino beam produced at the J-PARC (Japan Proton Accelerator Research Complex) facility; the INGRID and ND280 near detectors placed at 280 m downstream from the target used to produce the beam and the Super-Kamiokande (SK) water Cherenkov far detector located a further 295 km away. The layout of the T2K experiment is summarised in figure 1.3.

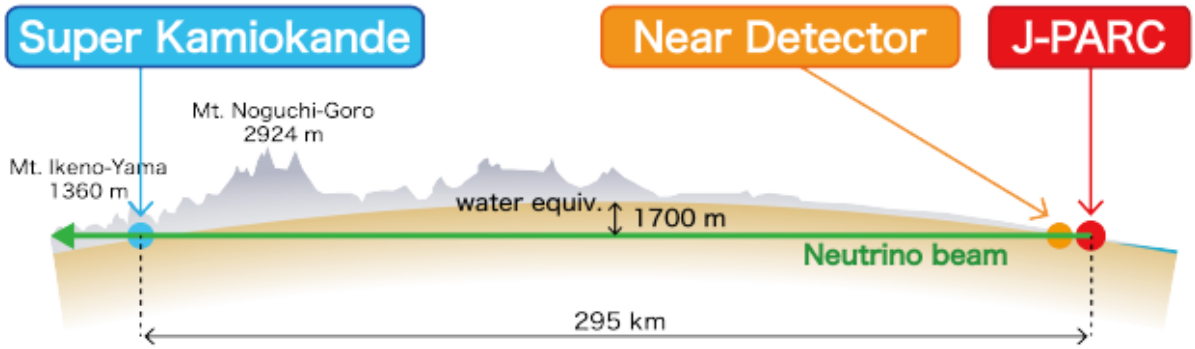

Fig.1.3 The layout of the T2K experiment

Specifically, a high purity ν_μ beam is produced at J-PARC in Tokai-mura (Ibaraki). The energy spectrum and beam profile are measured at the near detector complex at 280m from production.

Next, the neutrino beam arrives at SK detector in Kamioka (Gifu), with an energy peak of 0.6~GeV and SK detects the oscillated neutrinos. Both SK and the ND280 near detector are placed 2.5° off-axis from the beam center.

1.4.3.b The J-PARC neutrino beam

J-PARC is a newly constructed accelerator facility consisting of three accelerators: a linear accelerator to accelerate a H^- beam to 400 MeV (LINAC), a rapid-cycling proton synchrotron which begins with charge stripping foils to create a proton beam that is then accelerated to 3 GeV (RCS) and the main ring synchrotron which further accelerates some portion of the protons (MR) (Fig. 1.4).

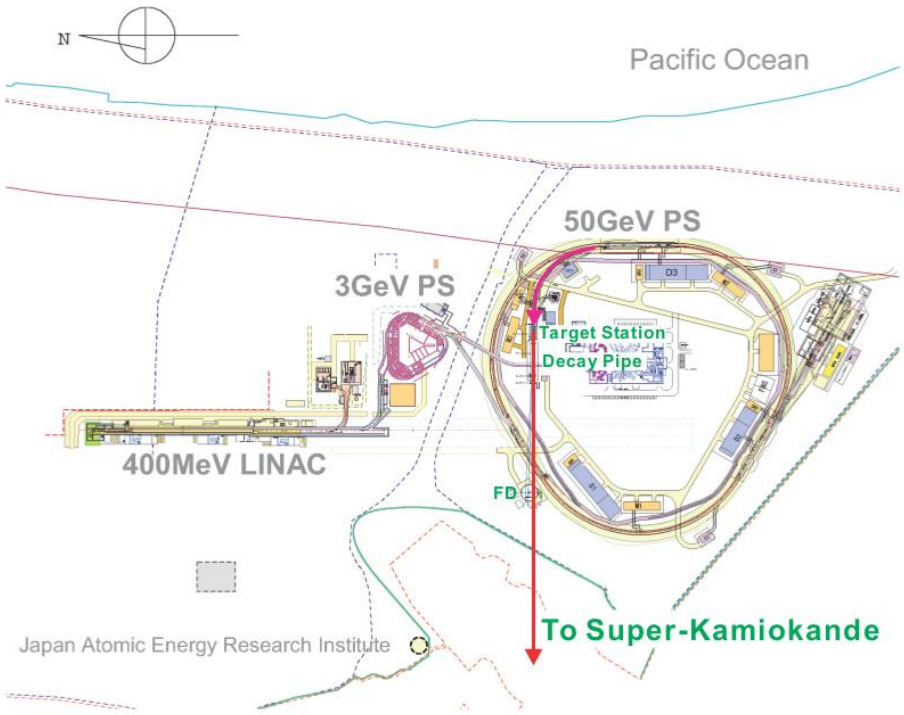

Fig. 1.4 The J-PARC accelerator complex

The proton synchrotron produces this proton beam fast-extracted in a single turn and accelerated up to 30 GeV against a graphite target to produce pions and kaons. In a cycle of the proton beam, there is a chain (called spill) of 8 bunches of the

protons and the proton beam is transported to the neutrino beamline with conserving the spill structure: this is called fast-extraction (figure 1.5).

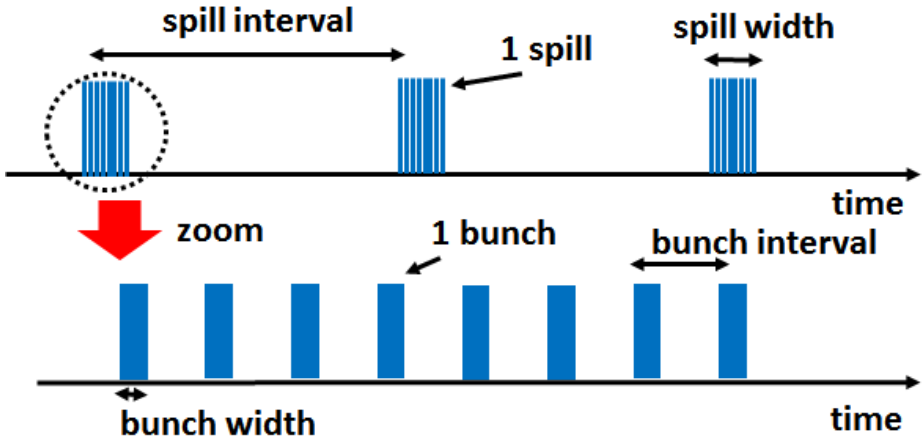

Figure 1.5 Beam structure for the T2K experiment. Protons are contained in each bunch.

The hadrons produced in proton interactions in the target are charge-selected and focussed by electromagnetic horns to the decay pipe to produce muons that then decay to muon neutrinos which point toward Kamioka: this is the primary neutrino beamline. By switching the polarity of the magnetic horns the charge of the mesons focussed by the horns is also reversed, thereby allowing the production of a predominantly neutrino or antineutrino beam.

The impinging protons stimulate the production of mesons in the target that are then, in the secondary neutrino beamline, charge selected and focussed into a decay volume by magnetic horns. Surviving hadrons are stopped in the beam dump and through-going muons are sampled by the muon monitor, which is used to provide pulse-by-pulse monitoring of the properties of the secondary beam (Figure 1.6).

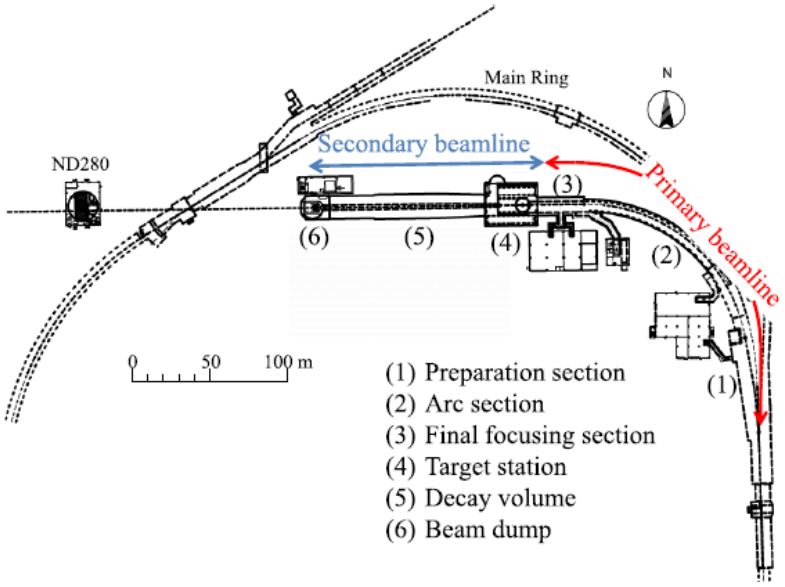

Fig.1.6 Schematics of the primary and secondary beamlines that are involved in the production of the J-PARC neutrino beam

As in all neutrino beam experiments, stable and well tuned beam operation is vitally important to produce both a high intensity and consistent neutrino beam.

The primary beamline is equipped with 96 separate instruments for measuring the position, intensity, profile and loss of the beam. In particular, the current transformers (CT) are 50-turn toroids around the beam pipe that are used to measure the intensity of the beam (figure 1.7)

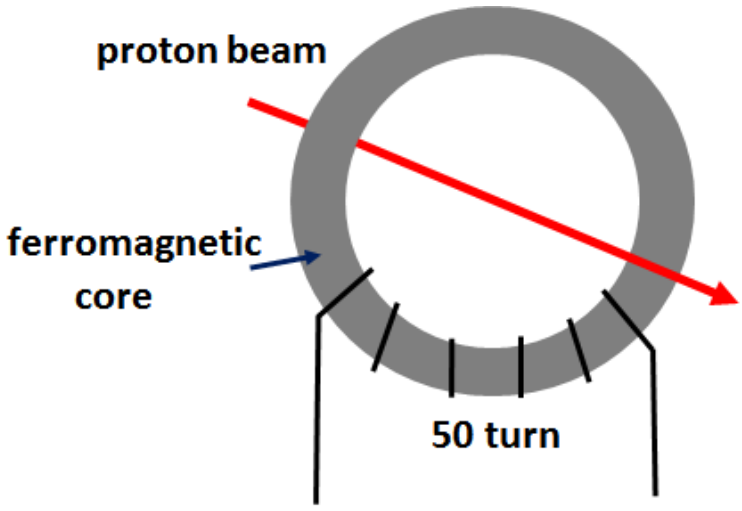

Figure 1.7 Illustration of the CT.

The induced current in the CT is measured when each bunch passes through the coil and is converted into the number of protons in the spill. The final CT, CT5, is located just before the protons reach the target, and it is used to determine the number of protons on target (POT) delivered. The secondary beamline consists of the graphite target, three magnetic horns to focus the secondary pions, a decay volume for the hadrons to decay into neutrinos and other particles, and a beam dump to absorb the non-neutrino products. The target is a graphite cylinder, 91.4 cm long and with 2.6 cm of diameter, surrounded by a 2 mm thick graphite sleeve and a 0.3 mm thick titanium casing and is cooled by helium gas flowing between each layer. Protons interact within the graphite, creating large numbers of secondary mesons, the majority of which are pions. The target sits within the inner conductor of the first magnetic horn, which collects these mesons (fig. 1.8).
The second and third horns then focus these mesons to produce a meson beam.
Whilst the focussed mesons are in the 96 m long decay volume, most decay to muon neutrinos (or antineutrinos) via the following processes:

$$\pi^+ \rightarrow \mu^+ + \nu_\mu$$
$$\pi^- \rightarrow \mu^- + \bar{\nu}_\mu$$
$$K^+ \rightarrow \mu^+ + \nu_\mu$$
$$K^- \rightarrow \mu^- + \bar{\nu}_\mu$$

However, imperfect horn focussing allows some contamination and some of the subsequent muons also decay to produce a small (anti)electron neutrino: this forms a muon neutrino beam with a peak energy of approximately 600 MeV, contaminated with additional antineutrinos and electron neutrinos, which originate from kaon and other pion parents. All the hadrons and muons below 5GeV/c are stopped by the beam dump placed 110 m downstream from the target. Behind the beam dump, there is a muon monitor (MUMON) that monitors the direction of the beam and provides a real-time measure of the beam direction and intensity to an

accuracy of 0.25 mrad and monitor the neutrino beam intensity to a precision of 3%.

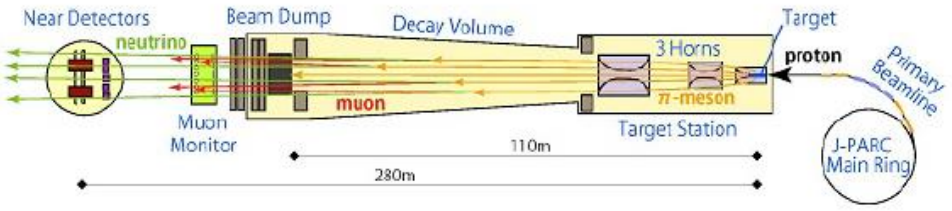

Fig 1.8 Neutrino J-PARC beamline facility.

The integrated number of neutrinos which pass through both the near detector ND280 and far detector Super-Kamiokande is proportional to the number of protons on target (POT). The generated beam power can be expressed by the statistical measure unit, POT, and beam energy:

$$\text{Beam Power} = \frac{(\text{POT in Spill}) \text{x} (\text{Beam Energy})}{\text{Spill Period}}$$

The source of neutrino flux uncertainties that are related to the beam direction and horn currents can be determined from the beamline and muon monitoring system. The expectation is to deliver $7.8 \text{x} 10^{21}$ protons on target in total for the T2K data physics analysis. There are two near detectors (INGRID on-axis and ND280 off-axis) 280 metres from the start of the beam at JPARC, which is used to characterise the beam near its origin.

The partly oscillated beam is finally detected by the far water Cherenkov detector ‘Super-Kamiokande’ (figure 1.9).

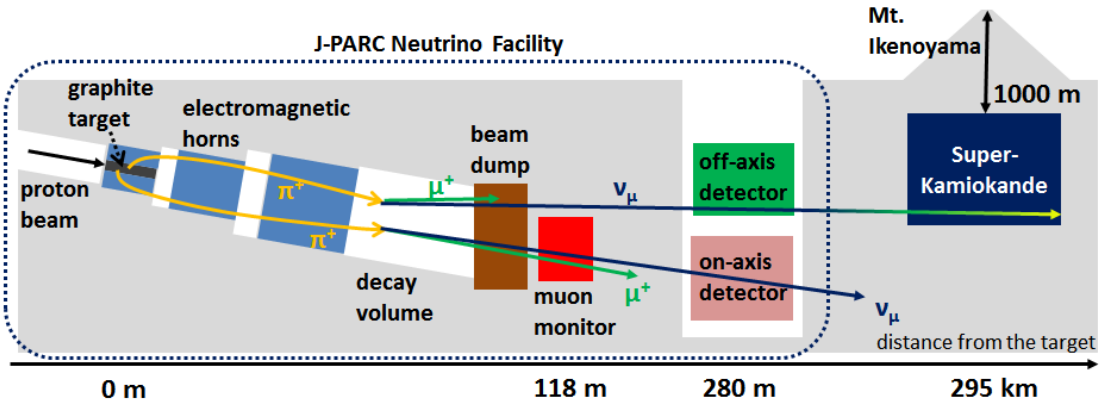

Fig. 1.9 A The beam and the detectors involved in T2K experiment

1.4.3.b The far detector Super-Kamiokande

The far detector, Super-Kamiokande (SK), is located in the Kamioka Observatory, and has been successfully taking data since 1996. The detector was also used as a far detector for the K2K experiment. SK is the world's largest land-based water Cherenkov detector; it is a 50,000 tons water Cherenkov detector located at a depth of 1,000 m (2,700 meters water equivalent) in the Kamioka mine in Japan. During its four major running periods (SK I to SK IV) Super-Kamiokande contributed results in the field of flavor oscillations of atmospheric, solar and accelerator-produced neutrinos, as well as setting the world-leading limits on the proton lifetime.

The primary strategy to measure the flavor composition of the T2K neutrino beam at SK, and thereby observe the oscillation of ν_μ to either ν_e or ν_τ is to count charged current quasi-elastic (CCQE) interactions for muon and electron neutrinos, both of which produce leptons of their respective flavor.

The relativistic charged particles, produced in these neutrino interactions, travel through the detector with a speed faster than the speed of light in water. The thereby polarized water molecules rapidly turn back to their ground state and emit Cherenkov light, which is detected by the ID PMTs.

For both ν_μ and ν_e CCQE signals the starting position of the leptons is required to be fully contained in the fiducial volume, which is defined to be more than 2m away from the ID wall for a total fiducial.

The pulse hight and timing information of the PMTs are fitted to reconstruct the vertex, direction, energy, and particle identification of the Cherenkov rings. A typical vertex, angular and energy resolution for 1 GeV muons is 30 cm, 3° and 3%, respectively. The typical ring shape, which is obtained from fully contained charged particles with an energy above the Cherenkov threshold, allows to infer the vertex position and the momentum of the charged particles. A very good discrimination between fuzzy electron like Cherenkov rings and sharp edged rings from muons enables to separate ν_e from ν_μ interactions. The fuzzy electron like ring is due to the multiple scattering which is more likely to occur for electrons than for muons because of the electron smaller mass and almost always an electron induce electromagnetic showers at the energies relevant to SK. A typical rejection factor to separate muons from electrons (or vice versa) is about 100 for a single Cherenkov ring event at 1 GeV. The electrons and muons are further separated by detecting decay electrons from the μ decays. A typical detection efficiency of decay electrons from stopping cosmic muons is roughly 80%. A 4π coverage around the interaction vertex provides an efficient π^0 detection. Interactions of neutrinos from the J-PARC accelerator are identified by synchronizing the timing between the beam extraction time at the accelerator and the trigger time at Super-Kamiokande using the Global Positioning System (GPS). A quantity ΔT_0 is defined, which is the timing between the beam extraction time at the accelerator and the trigger time at SK.

Chapter 2

Super-Kamiokande is located inside the Kamioka mines (in the Alpine chain overlooking the Japanese Sea), it is made of 50 ktons of ultra-pure water and it allows the measurement of muons, electrons and pions produced in the interactions of neutrinos with the water itself, all of this using the Cherenkov effect.

The Super-Kamiokande (SK) detector is sensitive not only to the interactions of neutrinos coming from JPARC, but also to those generated for example inside the sun and/or by SuperNovae. In particular, with a threshold set near 3.5 MeV, SK is currently the largest and most sensitive observatory to these phenomena.

2.1 History and construction of Super-Kamiokande detector

The Super-Kamiokande Collaboration was organized as a Japan–US collaboration in 1992 but the detector was originally proposed by M. Koshiba and the Kamiokande Collaboration in 1984.

Since the start of operations in 1996, Super-Kamiokande has gone through four data taking periods, SK-I, -II, -III, and –IV(Tab. 2.1)

		SK-I	SK-II	SK-III	SK-IV
Observation	Start	Apr. 1996	Oct. 2002	Jun. 2006	Sep. 2008
	End	Jul. 2001	Oct. 2005	Aug. 2008	May 2018
Live time (days)		1489.2	798.6	518.1	3509.6
Number of PMTs	ID	11146	5182	11129	11129
	OD	1885	1885	1885	1885
Photo Coverage		40%	19%	40%	40%
FRP & Acrylic Case		No	Yes	Yes	Yes
Electronics	ID	ATM	ATM	ATM	QBEE
	OD	OD QTC	OD QTC	OD QTC	QBEE
Trigger		Hardware	Hardware	Hardware	Software

Table 2.1 SK epochs

The differences between the detector setups from different epochs must be taken into account when analyzing data, developing algorithms or building Monte Carlo (MC) samples. Generally speaking, the extension of procedure successfully validated for one epoch to data or simulated samples related to another epoch is not a trivial subject, it may require modications and it must pass additional validation in order to be accepted.

Though the basic configuration the detector is similar across the phases there are a few important differences. At the start of the SK-IV period in 2008 the front-end electronics were upgraded to a system with an ASIC based on a high-speed charge-to-time converter [28]. The new system allows for the loss-less data acquisition of all PMT hits above threshold and has improved the tagging efficiency of delayed Michel electrons from muon decay from 73% in SK-III to 88%. Further, following a period of detector maintenance and upgrades at the end of SK-I (1996-2001), the implosion of a single PMT at the bottom of the detector on November 12, 2001, created a shock wave and chain reaction that went on to destroy 6,665 ID and 1,027 OD PMTs. The detector was rebuilt the following year with nearly half of the photocathode coverage (19%) in the ID (5,137 PMTs) and the full complement of OD PMTs for the SK-II period (2002- 2005). Since that time all ID PMTs have been encased in fiber-reinforced plastic shells with 1.0 cm thick acrylic covers to prevent further chain reactions. This resulted in an increased threshold of 7.0 MeV in SK-II compared to 5.0 MeV in SK-I. In 2006 the detector underwent a second upgrade in which the remaining ID PMTs were replaced and additional optical barriers were added to the top and bottom portions of the OD to improve separation with its barrel region. Both SK-III (2006-2008) and SK-IV (2008-present) were operated with the full 40% photocathode coverage in the ID.

The Super-Kamiokande detector (SK) has been successfully taking data since 1996[28].

T2K uses the Super-Kamiokande detector as its far detector, which is situated 295 km from J-PARC in a zinc mine 1 km underground, close to the town of Kamioka in the prefecture of Gifu, Japan. It is part of the Kamioka neutrino observatory which is operated by the Institute for Cosmic Ray Research (ICRR) of the University of Tokyo.

The neutrinos reaching SK are from many sources: the core of the sun; produced by cosmic-rays in the atmosphere; created in accelerators and from astrophysical sources such as supernovae. Solar neutrinos have low energies in the order of a few MeV. While atmospheric neutrinos arrive at the SK site from the atmosphere surrounding the entire globe and have an energy range from a couple of MeV to multiple TeV. SK has been the Far Detector of the first neutrino beamline experiment KEK-to-Kamioka (K2K) [29] which produced accelerator neutrinos by the collision of accelerated protons on a target and focusing the interaction and decay products that include neutrinos. SK is currently acting as the Far Detector of the neutrino beamline experiment Tokai-to-Kamioka (T2K) [30], the successor to K2K and offering a higher intensity and precise neutrino beam.

2.1.1 Detector Overview

The detector consists of a cylindrical stainless steel tank (41.4 m in hight and 39.3 m in diameter), holding 50 kt of ultra-pure water, and the photomultiplier tubes (PMTs) lining the tank interior detect the Cherenkov radiation which is produced by charged particles which propagate in the water (figure 2.1). The primary purposes of the detector are nucleon decay searches and the detection of neutrinos from various sources: solar neutrinos, astrophysical neutrinos such as the ones from supernovae, atmospheric neutrinos and accelerator neutrinos in long-baseline neutrino oscillation experiments such as K2K and T2K.

There are two concentric cylinders inside the tank; the inner detector (ID) and the outer detector (OD). The ID is a main detector which contains 32 kton of

water with 36.2 m in height and 33.8 m in diameter, whereas the OD is a cosmic ray muon veto detector which covers the region surrounding the ID with the thickness of about 2 m. Both detectors are optically separated by opaque materials, two layers of polyethylene terephthalate sheets, referred to as “black sheets" mounted on each side of the structure that holds the PMTs.

The OD is also used to prevent backgrounds from the surrounding rock such as neutrons and gamma rays.

The combination of the ID and OD allow Super-Kamiokande (SK) to determine which interaction vertices originate from within the detector, and which are due to particles and radiation entering from outside the detector.

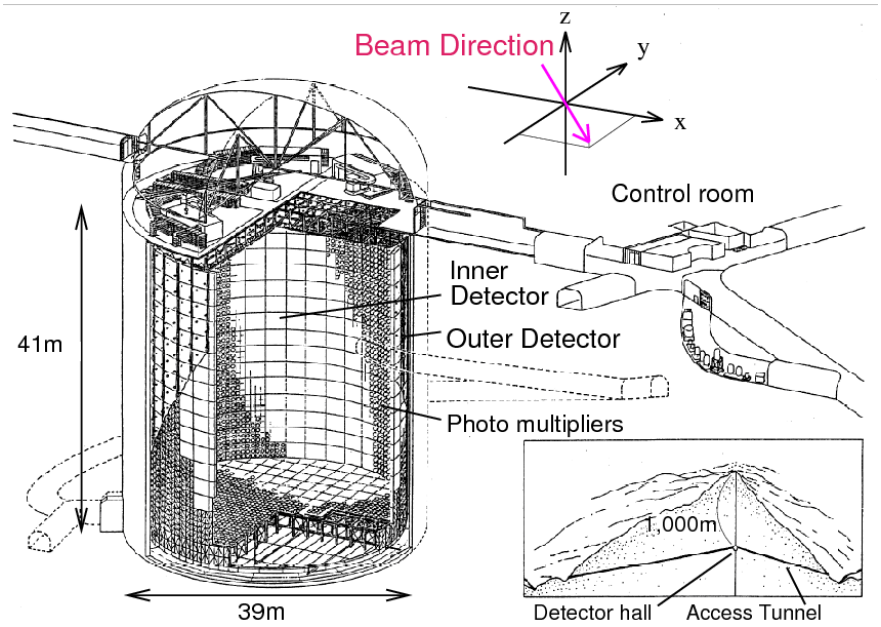

Fig. 2.1 ND280 The Super-Kamiokande detector.

The ID currently houses along its inner walls 11,129 inward-facing 50 cm diameter PMTs: each PMT has a 70.7 cm grid spacing for a 40% cathode surface coverage while the OD contains along its inner walls 1,885 outward-facing 20 cm diameter PMTs. Wavelength shifter plates are attached to the OD PMTs as it was done in the IMB experiment [31]. This increases their collection efficiency by about a factor of 1.5 but the wavelength shifter plates also broaden the timing resolution of the OD PMT by about 2 ns. This is a

reasonable price to pay for the gain in collection efficiency since the main purpose of the OD is to act as a veto counter.

All the PMTs are mounted on the same stainless steel structure and the inner PMTs are facing inwards and the outer PMTs outwards (figure 2.2).

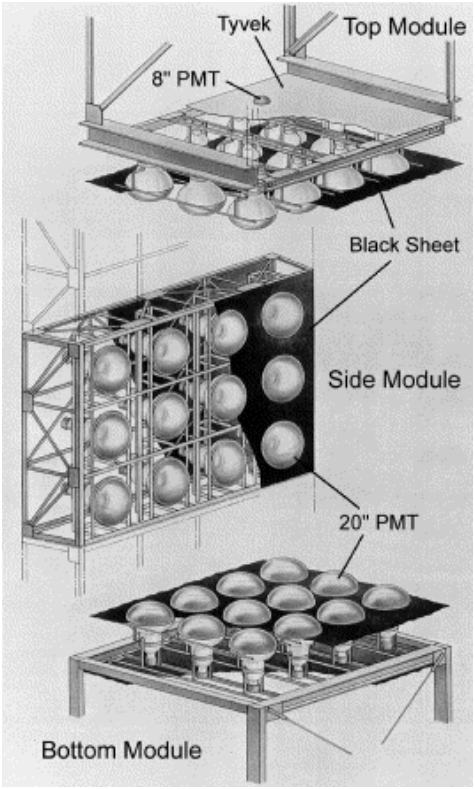

Fig. 2.2 Details of the stainless steel structure, and mounting of the PMT

Each PMT in the ID and OD is connected via a single cable to high voltage supplies and signal processing electronics: the cables end in four electronic huts built on the upper tank cover, which are accessible during normal operation of the detector via a tunnel from the control room. These huts contain electronic racks and front-end acquisition electronics and must be routinely checked for malfunctions at least once a day by the operators taking the morning shift in the mine.

Another hut on the top of the tank is the “Central Hut", it contains electronics for triggering, housekeeping and Global Positioning System (GPS) time

synchronization systems. The trigger rate is checked during the morning shift and reported on a blackboard in the control room for monitoring purposes.

An event produced in the ID is tagged as Fully Contained (FC) if it doesn't trigger a significant response indicating entering or exiting charged particles in the OD. Events triggering such a response in the OD are tagged as Partially Contained (PC). The official Fiducial Volume (FV) is defined as a cylindrical volume with surfaces 2 meters inwards from the ID PMT plane. The fiducial mass is 22.5 ktons, corresponding to 7.5 x 10^{33} protons.

Super-Kamiokande can detect events in a range from 4:5MeV to up to 1TeV in energy. A LINear ACcelerator (LINAC) is available in the dome for calibration purposes.

The cables that connect the PMTs to the electronic huts located on the top of the detector pass through 12 cable holes. Four of these twelve holes are above the ID and would prevent Cherenkov light from being seen in the OD.

Since the PMTs are sensitive to magnetic fields, 26 Helmholtz coils line the wall of the tank and reduce the geomagnetic field to ~50 mG.

2.2 A Water Cherenkov Detector

Super-Kamiokande is able to make physical measurements primarily by observing Cherenkov radiation using PMTs: Cherenkov radiation is an electrodynamic phenomenon which is analogous to the sonic boom produced by an object travelling faster than the speed of sound.

When an electro-magnetically charged particle travels faster than the speed of light in a given medium, a cone of Cherenkov light is emitted(Figure 2.3):

$$v \geq \frac{c}{n}$$

where v is the velocity of the charged particle, c is the velocity of light, and n is the index of refraction of the medium.

This phenomenon is named “Cherenkov effect", and the light emitted is known as “Cherenkov radiation".

The Cherenkov cone has its opening angle ϑ_C which satisfies,

$$\cos\vartheta_c = \frac{1}{n\beta}$$

In the case of water, where n = 1,34 in the visible range, ϑ_C is 42° for highly relativistic particles, with β~1.

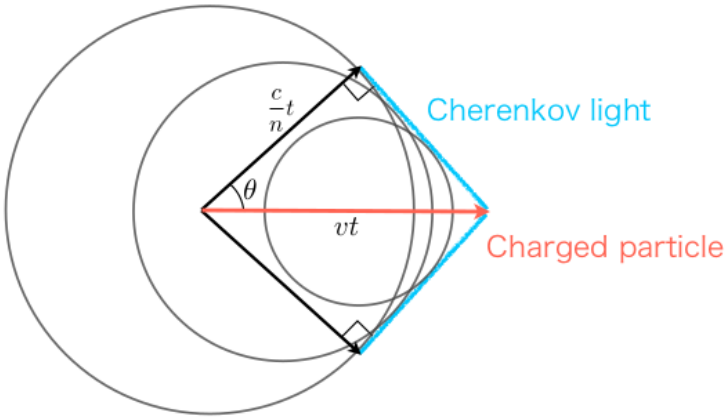

Figure 2.3: A schematic drawing of Cherenkov radiation.

The momentum threshold for the Cherenkov radiation is derived from the condition of β > 1/n and table 3.1 summarizes the Cherenkov threshold for various charged particles in water.

	e	μ	π^+	p
Momentum (MeV/c)	0.57	118	156	1052

Table 3.2 Momentum thresholds of the Cherenkov radiation in water for various charged particles assuming n = 1.34.

The number of Cherenkov photons, N, emitted as a double derivative with respect to the wavelength λ and charged particle trajectory, x, is given by:

$$\frac{d^2N}{dxd\lambda} = \frac{2\pi\alpha}{\lambda^2}\left(1 - \frac{1}{n^2\beta^2}\right)$$

where α is the fine structure constant. For the wavelength between 300 nm and 600 nm, 340 photons are emitted per unit cm by the particle with β~1in water. In Super-Kamiokande, neutrinos are detected when they interact with the water and produce charged particles above the Cherenkov threshold, and the cone of light emitted by a charged particle is observed as a ring by the PMTs on the detector wall. For each event the time of the first photon arrival as well as the integrated charge at each PMT is recorded, and from that information the type and the kinematics of the particles are inferred.

In the Super-Kamiokande detector, if an event is fully contained inside the inner detector, a Cherenkov cone appears as it can be seen in Fig. 2.4. The axis of the cone corresponds to the direction of the particle, and by measuring the number of photoelectrons detected in the photomultiplier tubes (PMTs), we are able to reconstruct the energy of the particle.

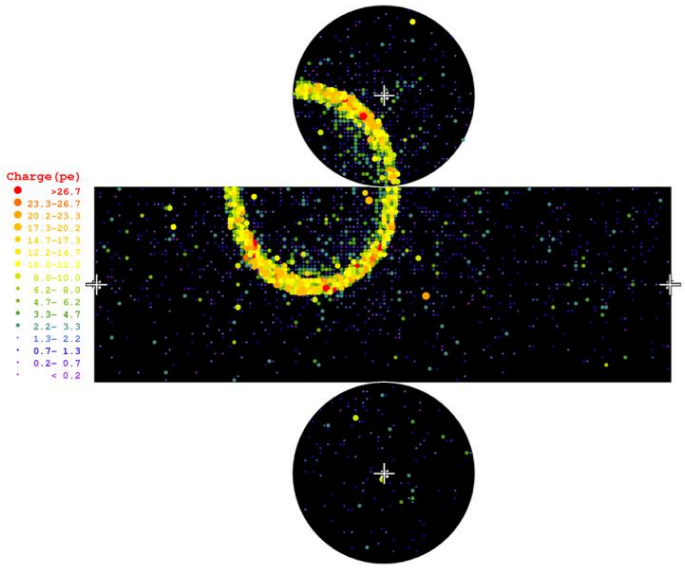

Figure 2.4: Example a Cherenkov ring created by a 1 GeV muon in the Super-Kamiokande detector

In this fashion, SK can detect various charged particles and reconstruct physical variables by the analysis of Cherenkov rings. Electrons or high energy gamma-rays create fuzzy rings (“shower”) since they produce electromagnetic shower and are deflected by the multiple scattering, whereas muons or charged pions create sharper rings (“non-shower”) since they do not produce electromagnetic shower. Not only the particle type, the kinematics of particle such as the vertex, direction and momentum are determined by using the Cherenkov light arrival time and its amount received at each PMT: when a muon neutrino interacts it produces a single muon, which then produces concentric rings of photons as it travels through the water, producing a clear “sharp” ring pattern on the wall of Super-Kamiokande. An electron neutrino interaction, on the other hand, produces an electron which subsequently showers to produce more electrons, all of which then produce Cherenkov showers which overlap to produce a fuzzy ring on the wall of the detector. This process is shown in Figure 2.5.

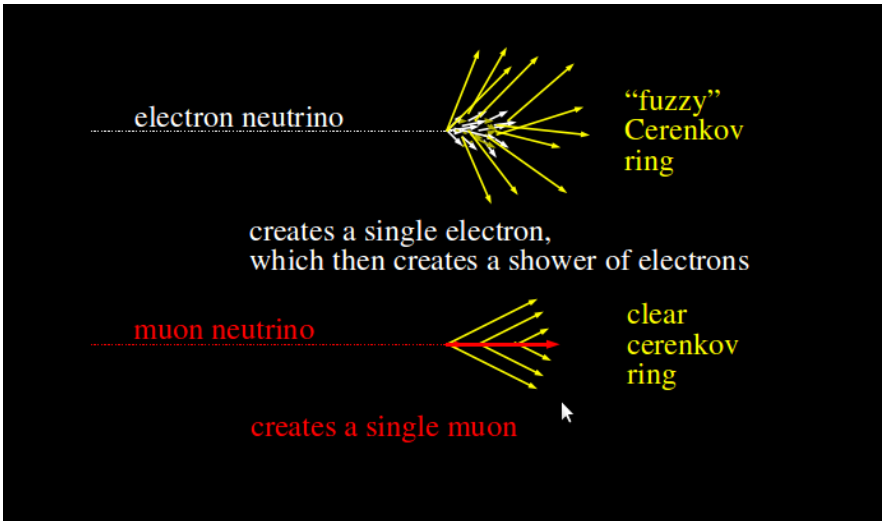

Fig. 2.5 a: Cherenkov light produced by an electron neutrino (white) and by a muon neutrino (red)

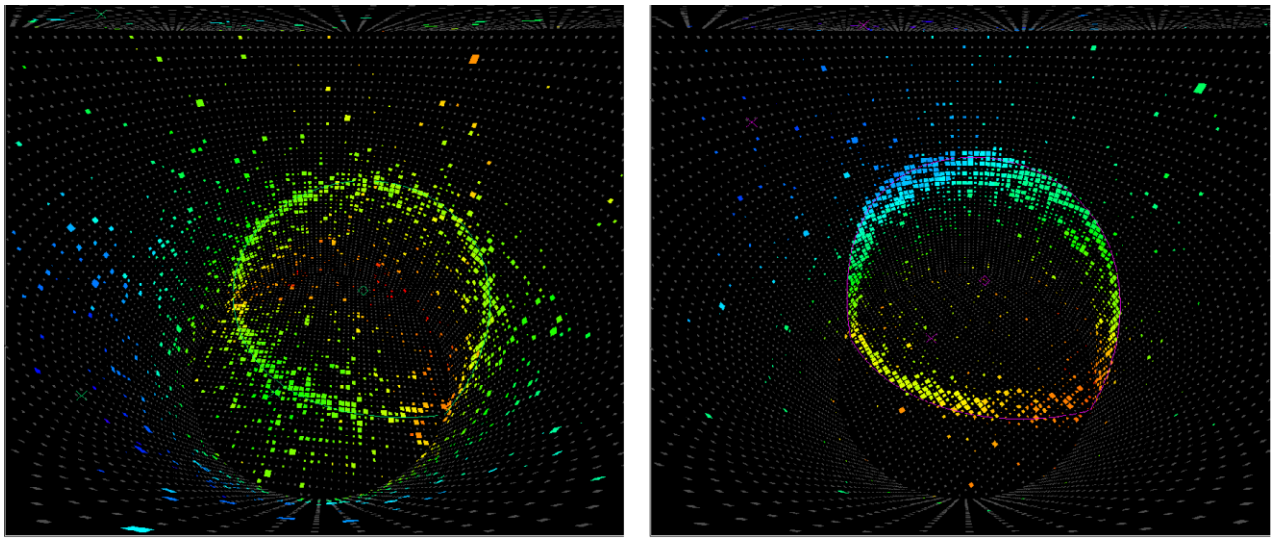

Fig. 2.5 b The ring on the left has a fuzzy ring made by an electron.
The ring pattern on the right was created by a muon neutrino.

2.3 Water and Air Purification

The purify of the water is crucial for this experiment: as Cherenkov light needs to travel tens of metres in the detector water before reaching the PMTs to be detected, it's necessary a high transparency of the water.

So, the original source of the Super-Kamiokande water, spring water in the mine, is highly purified by the water system circulating at a rate of about 30 tons/hour to maintain high water transparency and to remove radioactive isotopes such as Radon (Rn) and Radium (Ra). Such isotopes are significant backgrounds for low energy analyses, in particular for the study of solar neutrinos.

The water purification system mainly consists of several filters, a UV sterilizer and two degasifiers in order to remove particles larger than 0.2 μm, bacteria and radon dissolved in water, respectively (figure 2.6). The water temperature is controlled at around 13°C by heat exchangers in order to reduce PMT dark noise and suppress bacteria growth. The resistivity of the water flowing out of the detector for purification is about 11 MΩ·cm and averages at 18.20 MΩ·cm after purification, approaching the chemical limit. The light attenuation length

is about ~100 m, and particles larger than 0.2 nm are reduced to 6 particles/cc [32].

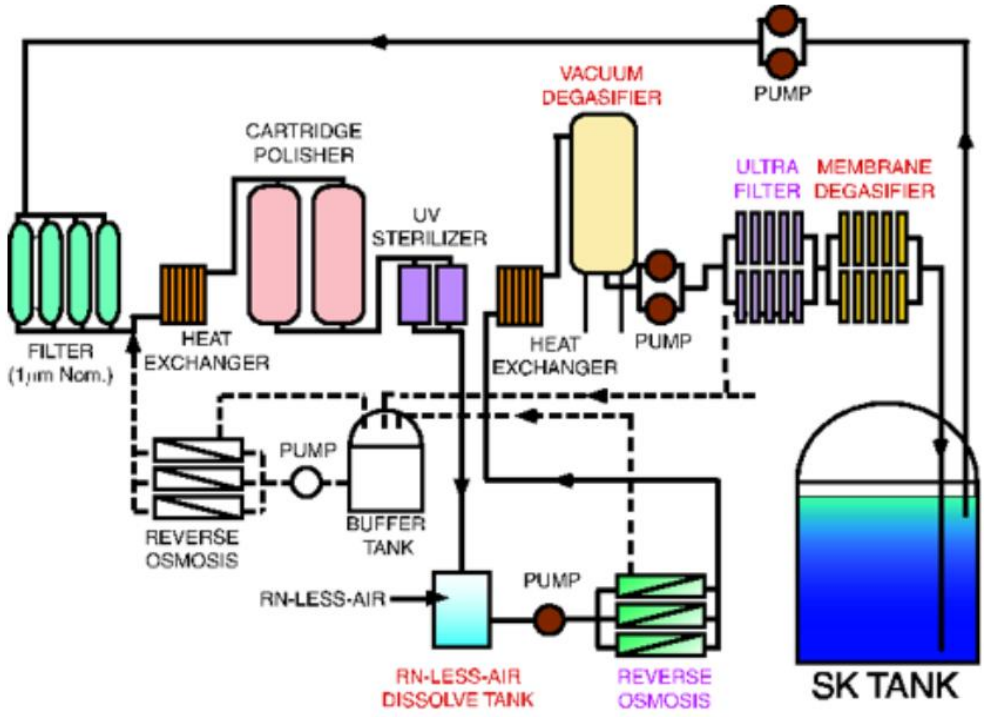

Fig. 2.6: Water System

As the rock in the mine has high radon content, the air in the mine is naturally rather high in radioactivity. In order to reduce the radon level in the air especially so that it does not contaminate the detector water, filtered Rn-free air is continuously supplied from outside of the mine into the experimental area, keeping the area at positive pressure (figure 2.7). The winter levels, where cool air flows in from outside, are comparably low at ~100–300 Bq/m3, however the summer levels, where air flows from deep within the mine, are ~2,000–3,000 Bq/m^3. Firstly fresh air is pumped into the SK dome area at a rate of 10m^3/minute, resulting in a typical radon concentration of ~20–30mBq/m^3 at the SK dome and control room. This system pumps the purified air into the SK tank, above the water level at a positive pressure to prevent any Radon present in the dome air from dissolving in the highly purified water [33]. The resulting radon concentration in the radon-free air is less than 3mBq/m^3.

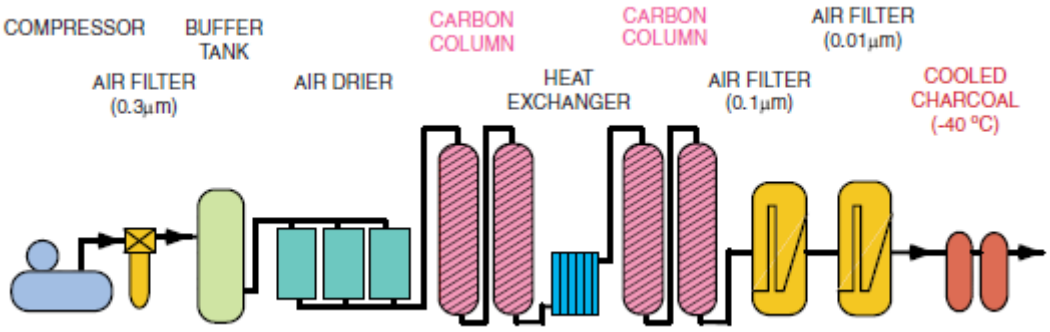

Fig. 2.7: Air purification System

2.3.1 Water properties measurement

Since the Cherenkov radiation emitted by particles inside the tank travels in water before detection, the optical properties of the water inside the tank must be accurately measured, especially for simulation purposes.

The water attenuation is modeled as:

$$I(\lambda) = \exp(-l/L(\lambda))$$

where $I(\lambda)$ is the intensity of light at wavelength λ and l is the distance traveled in water. $L(\lambda)$ is the attenuation length in water at wavelength λ and it's defined as:

$$L(\lambda) = \frac{1}{\alpha_{sym}(\lambda) + \alpha_{asy}(\lambda) + \alpha_{abs}(\lambda)}$$

The coefficient $\alpha_{sym}(\lambda)$ represents the amplitude of the symmetric scattering which takes into account the effects from Rayleigh scattering and symmetric Mie scattering, and it has the angular distribution of the form $1 + \cos^2(\vartheta)$ where ϑ is the photon scattering angle. $\alpha_{asy}(\lambda)$ represents the asymmetric scattering which accounts for forward Mie scattering, and it has the angular

dependence of cos ϑ in the forward direction while there is no backward scattering. Finally, $\alpha_{abs}(\lambda)$ is for absorption. These coefficients are empirical functions of the wavelength λ which are determined based on the calibration data from a laser injector system as shown in Figure 2.8:

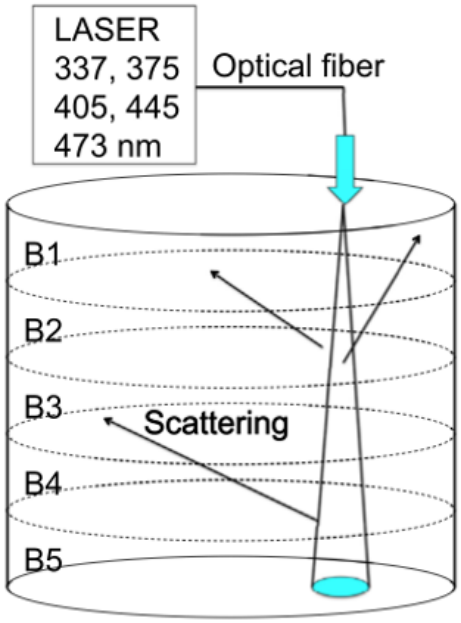

Figure 2.8: A schematic view of the laser injector system for measuring the water property and the reflectivity of the PMTs.

In the setup, a collimated laser beam is injected at the top of SK vertically down toward the bottom, and the light scattered in water and reflected from the bottom is detected by the PMTs on the side and the top wall of the detector. The TOF-subtracted hit time distribution, i.e. the PMT hit timing distribution after subtracting the time required for photons to travel from the beam spot at the bottom to each PMT, for the PMTs in each detector region as indicated in Figure 2.8 is shown in Figure 2.9. The sharp peaks on the right between 1830-1900 ns are due to the photons reflected at the beam spot from the bottom of the detector, whereas the hits at earlier times are caused by photons which

scattered in water before reaching the bottom and arrived at the side or the top wall.

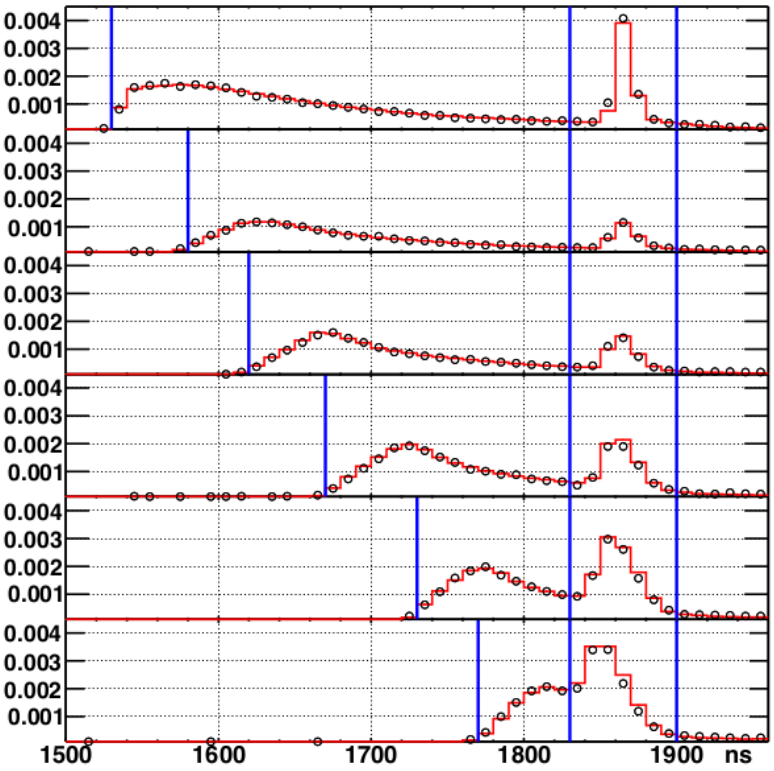

Figure 2.9: The TOF-subtracted hit time distributions for the laser injector data taken at 405 nm. The top plot is for the PMTs on the top wall, and the following five plots correspond to the five regions on the barrel as indicated in Figure 2.8. The black circles represent the measured data and the red histograms are the result from the laser injector simulation after tuning the water properties and PMT reflectivity to data.

2.4 Photosensors

2.4.1 Inner PMTs

For the Cherenkov light detection in the Inner Detector(ID), PMTs manufactured by Hamamatsu Photonics K.K. (R3600) are used and have a diameter of 50cm (20inch). The dynamic range of the ID PMTs goes from a single photoelectron (pe) to about 300 pe. The peak quantum efficiency is about 21% at 360-400nm and the collection efficiency is 70% at the first dynode. The collection efficiency of the first dynode, gain, transit time spread and dark noise rate are over 70%, 107, 2.2 ns (1σ) for a single photoelectron and 3 kHz at 0.25 photoelectrons threshold, respectively. A schematic view of the 20 inch ID PMT is presented in Fig. 2.10.

The geomagnetic field at the detector site is about 450mG, while a magnetic field above 100mG affects the photoelectron trajectories in the PMTs, reducing the timing resolution. To compensate for this, 26 sets of horizontal and vertical Helmholtz coils were set up around the perimeter of the tank reducing the magnetic field in the PMTs to around 50 mG.

In November 2001, during the refilling operation that followed the upgrade, there was an accident where around 60% of the PMTs were destroyed by a chain reaction initiated by the implosion of one of the bottom ID PMTs: for this reason, an acrylic cover was designed for the PMTs, the Fiber Reinforced Plastics (FRP). The acrylic is 12 mm thick and UV-transparent, while the side of the PMTs are protected with a fiberglass casing. There are also holes in the casing to allow water to flow inside. The effect on the photon detection is small because the transparency of the cover for a normal incident photon in water is over 96% at 350 nm.

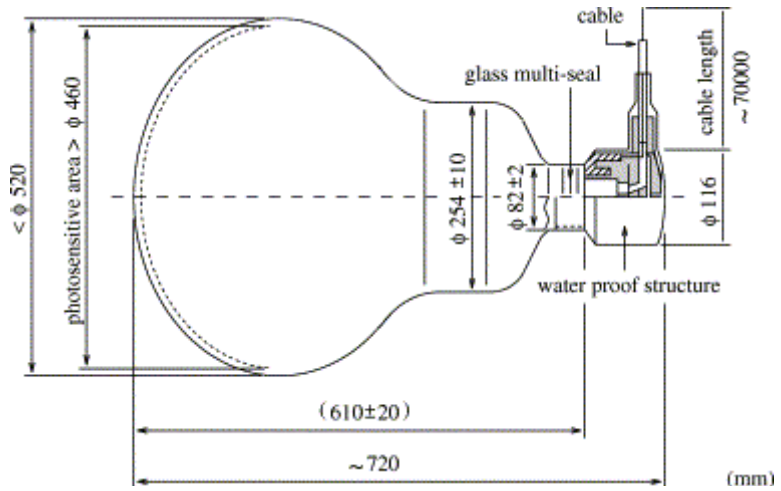

Figure 2.10: Schematic of a 20 inch ID PMT

2.4.2 Outer PMTs

The OD contains 1,885 8-inch PMTs, which are mostly Hamamatsu R1408 PMTs and some are reused from the IMB experiment [34]. In order to increase the photon collection efficiency, a 1.3 cm thickness 60 cm square wavelength shifting plate (ultra-violet light →blue-green light) is equipped to each OD PMT. The light collection efficiency is increased by 60% even if the timing resolution of the OD PMT (Fig. 2.11) gets worse from 13 ns to 15 ns in FWHM , due to the reemission process of the plate: however, in the OD, observing the extra photons is of much more importance than better timing resolution.

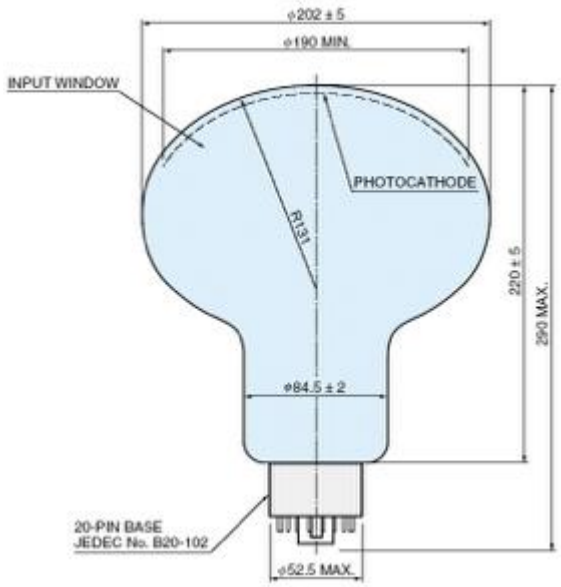

Figure 2.11: Schematic of a OD PMT

In order to better distinguish between entering, exiting and through-going particle events, the barrel region of the OD is optically separated from the top and the bottom regions by Tyvek.

Using the measured quantum efficiency, the PMT photocathode surface is simulated as part of the detector geometry. To determine the collected charge, the single p.e. distribution is summed for each photoelectron emitted and smeared by the timing resolution of the PMT. As well as this, properties of the electronics are simulated like the timing window and charge threshold.

The thickness of the supermodules defines a dead space filled with water surrounded with light-proof lining, from which in principle light cannot escape. The PMTs are connected to their power supply and data cables in this space: these connection must be water-proof since this dead volume is filled with water.

The OD PMTs are mounted in water-proof housings which e effectively block light from the dead space. However, because the ID PMTs are not fully covered in back, some light generated in this region is still detected by the ID PMTs.

2.4.3. Failing PMTs

The failure of PMTs is something that should be taken into account during the operation of SK, since mainteinance and replacement of any PMT of the detector is not a trivial and can be performed only when the tank is empty. A very common reason for PMT failure is the flooding of the water-tigh housing of their electrical connections.

Sometimes a PMT becomes a flasher: it develops internal electrical discharges which emit substantial optical radiation and electrical noise, requiring the PMT to be shut down.

The rest of failing PMTs show a wide variety of electrical and other problems.

Failed PMTs, once recognized, are just left in place waiting for the next maintenance period to be replaced, and their status is registered along with event data.

2.5 PMTs Calibration

It is necessary for any physics analysis to keep the charge and time response of each PMT are the same for the same intensity and timing of the incident light. Thus, the detector calibration is important.

The Super-Kamiokande ID performs two kinds of direct measurements on a PMT-per-PMT basis: it measures integrate charge and timing of the PMTs output responses through an electronic front-end. In order to make these measurements accurate, the response of each PMT must be accurately calibrated: the charge and time response of each PMT must be the same for the same intensity and timing of the incident light.

A proper calibration is required to have reliable data and for simulation purposes, e.g. transport of photons inside the water tank has to be precisely characterized, and, as it will be evident in the hybrid sample construction section, a proper calibration allows to make some useful assumptions about the

detector, e.g. the symmetry of the detector response under rotations around the cylindrical tank axis.

SK has its own coordinate axis system: all data and simulations use it as an implicit standard. The origin of the coordinate system is the exact center of the SK tank. The z axis is parallel to the cylindrical tank axis and points upwards, towards the mountain surface. The x axis is perpendicular to the z axis and points toward the SK access tunnel that connects the dome experimental area to the Atotsu mine tunnel. The y axis is set accordingly to the right hand rule applied to the other two axis.

The first step of calibration consists in setting the high voltage (HV) for each PMT in such a way that the output charge of each PMT is the same for the same light intensity.

A scintillator ball installed at the tank center and fed via an optical fiber with the light of a xenon lamp filtered with an ultra-violet filter is used as calibration source. The calibration source is isotropic by construction: since the SK ID is cylindrical, there is a dependency between the PMT location and the intensity of calibration light arriving at it.

2.5.1. Relative differences of gain

In order to compensate for this geometrical effect 420 standard PMTs had been pre-calibrated and were mounted in the tank at specific locations just before the beginning of the SK-III epoch, as shown in Figure 2.12. Then the HVs for these PMTs were adjusted to output the same charge for the same light intensity. The reproducibility of the observed charge for all standard PMTs with respect to their reference values was checked and evaluated as 1.3% RMS.

The HV of each other PMT in the tank is adjusted in order to match the output charge to that of the nearest standard PMT having a similar geometrical relationship with the calibration source.

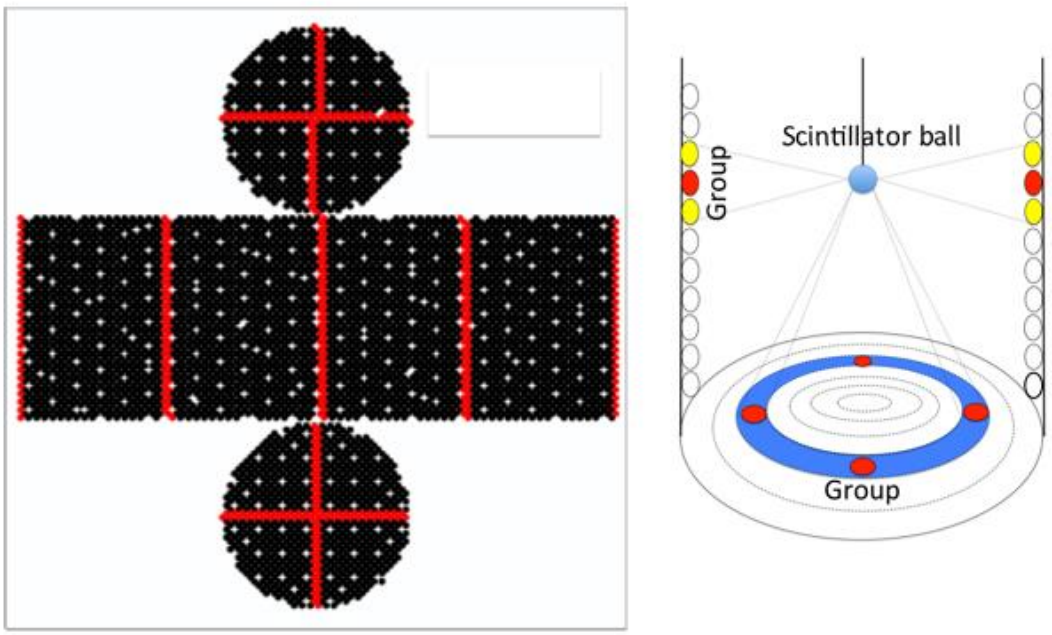

Figure 2.12: The location of standard PMTs inside the SK inner detector (left). The red points indicate the locations of the standard PMTs. These PMTs served as references for other PMTs belonging to the same group with similar geometrical relationship to the light source (right).

In order to interpret the output charge from the PMTs in number of photo-electrons, it's necessary to determine the gain for each PMT. This is done in two steps.

The first step is to determine the relative gain differences among PMTs. The calibration source for this relative gain calibration is a nitrogen laser (USHO KEC-100, a pulse width of 0.4 ns in FWHM at a wavelength of 337 nm). The output light is monitored by a faster response 2-inch PMT (Hamamatsu H2431-50, rise time: 0.7 ns). The wavelength of this light is shifted to 398 nm with a pulse width of 0.2 ns by a dye, and the light is passed through neutral filters and injected into an isotropic diffuser ball placed in near the tank center via an optical fiber. This apparatus is shown in Figure 2.13.

This shifted wavelength corresponds to the maximum of the convoluted response with Cherenkov spectrum, light absorption spectrum and quantum efficiency of the PMTs. By using this laser system, two measurements are conducted. The first one uses high-intensity (I_H) flashes, such that every PMT is reached by a suitable number of photons, and records the average observed charge $Q_{ob}s(i)$ for each PMT *i* which is given as:

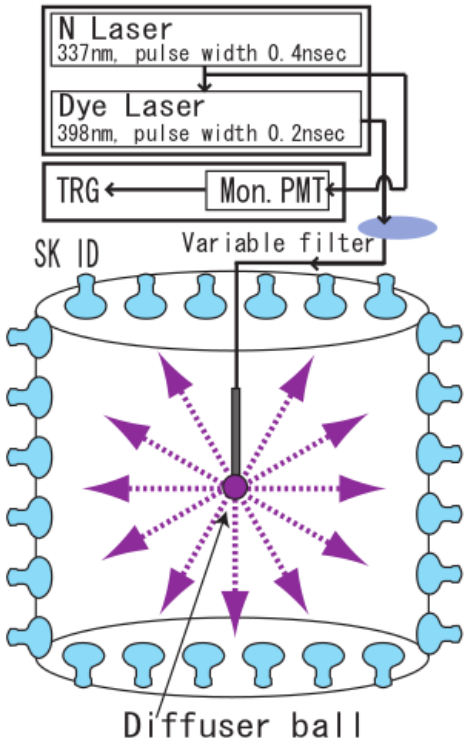

Figure2.13: The apparatus used for PMT relative gain and timing calibration. A set of neutral filters is used to adjust the output intensity.

$$Q_{obs}(i) \propto I_H(i) \times a(i) \times \varepsilon(i) \times G(i)$$

where $a(i)$ is the PMT light acceptance, $\varepsilon(i)$ is the PMT quantum efficiency and $G(i)$ is the PMT gain.

The second one uses low-intensity (I_L) flashes, such that only a few PMTs are hit per single flash, making the assumption that only one photoelectron is detected by each PMT reasonable, and counts the number of times that each

PMT *i* is hit normalized to the number of flashes ($N_{obs}(i)$) , i.e. the hit probability, which is given as:

$$N_{obs}(i) \propto I_L(i) \times a(i) \times \varepsilon(i)$$

Then, the gain of each PMT is obtained by taking the ratio of the above two equations:

$$G(i) \propto Q_{obs}(i) / N_{obs}(i)$$

The relative gain for each PMT is calculated by normalizing Gpiq to the average gain over all PMTs, and is used as a PMT-by-PMT correction factor in conversion from the output charge to the number of photoelectrons. The RMS of the relative gain distribution is 5.9%.

2.5.2. Absolute PMT gain calibration

The absolute gain, which relates the measured charge to the number of detected photoelectrons at a PMT, is obtained by a calibration measurement using a nickel source: a low energy gamma ray source made of a sphere of nickel which emits 9 MeV gamma rays isotropically upon capturing the neutrons emitted from a ^{252}Cf neutron source which is placed at the centre.

The source is placed at the centre of the ID and produces on average 0.004photoelectons/event at each PMT, and more than 99% of the produced hits will therefore be single photoelectron hits. After correcting for the relative gain variation for each PMT, the observed charge distribution for the single photoelectron hits produced by the nickel source is obtained by accumulating the hits from all PMTs. From the average of this distribution, the conversion factor between the observed charge and the number of photoelectrons is

determined to be 2.658 pC/photoelectron for SK-IV. The obtained single photoelectron charge distribution is also used in the detector simulation.

2.5.3 Determination of quantum efficiency

The quantum efficiency varies between different PMTs: measuring it is important since it's a parameter used by detector simulation algorithms.
The same nickel source as in the absolute gain measurement can be used: since the source intensity is low enough to assume that a single photoelectron is produced per hit, the hit probability $N_{obs}(i)$ for the *i* PMT can be expressed by Equation 1.7.
Since the light acceptance a (i) cannot be expressed in closed form, the quantum efficiency for each PMT has been determined by simulating the nickel source events assuming no individual variations for the quantum efficiency and comparing the simulation to the observed data.

$$N_{obs}(i) \propto I_L(i) \times a(i) \times \varepsilon(i)$$

2.5.4. Relative PMT timing calibration

The time interval between the time a photoelectron is initially produced at a PMT and the time the signal from the PMT is registered as a hit by the electronics varies between the PMTs due to many factors: the difference in the length of the cables connecting the PMTs to the electronics and the dependency of electronic processing time on the observed charge (time-walk effect) are the major contributors.

In order to measure these differences for each PMT the apparatus shown in Figure 2.13 is used. For each PMT, time-of-flight (TOF) is calculated as the time it takes for a photon to reach it from the position of the monitor PMT, used as a time reference, through the diffuser ball.

The TOF is subtracted from the response time, giving for each PMT the relative timing correction. Since the signal timing depends on the observed charge, the same measurement is repeated for each PMT at different laser intensities.

The result is plotted for each PMT as a 2D distribution known as TQ plot, as shown in Figure 2.14.

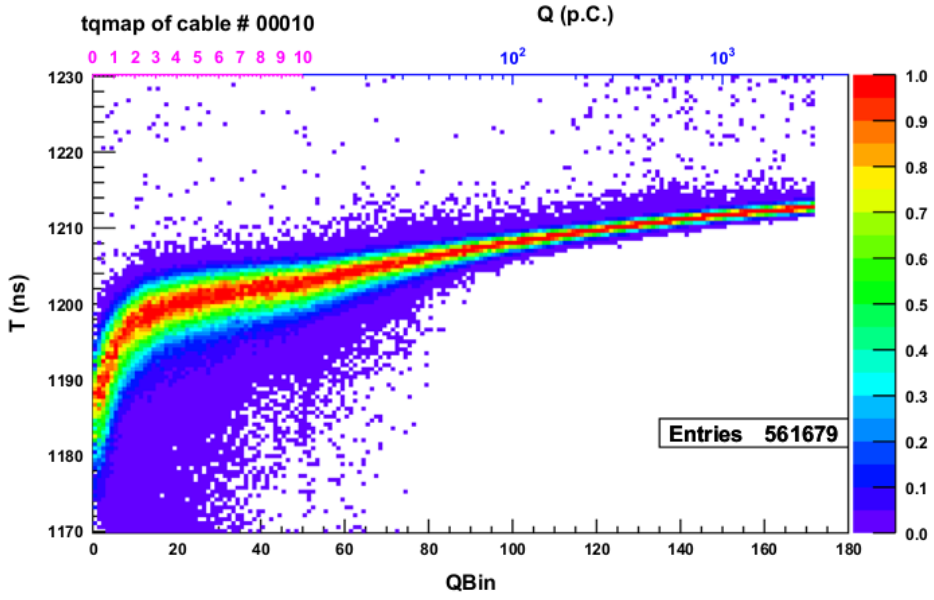

Figure 2.14: Example of the TQ plot for an ID PMT. The vertical and horizontal axes represent to the TOF subtracted hit timing and the hit charge,respectively.

Once the TQ distribution is obtained for each PMT, the distribution is fitted by an asymmetric gaussian in each charge bin, and the peak position of the gaussians is then fitted by a polynomial as a function of charge. The fitted peak position of the TQ distribution, named the TQ map, is saved into a database for each PMT and is then used to correct the hit timing as a function of charge on an individual PMT basis. This ensures that the time response of the PMTs in the entire detector is synchronized.

2.6. Electronics and data acquisition

Each PMT output in SK is connected to an electronic acquisition front-end channel via a 70 m long RG58 coaxial cable, one channel per PMT. If the negative signal pulse height fed into this input exceeds the trigger threshold level, the related PMT is considered as hit. The trigger threshold for a PMT hit is set at -1 mV, which is equivalent to 0.25 photoelectrons. If the number of hit PMTs exceeds an event threshold, the corresponding event trigger is issued. The event consists of the time and charge of the hit PMTs within a given time window around the trigger timing. There are several event triggers depending on the visible energy: the Super Low Energy (SLE) trigger, the Low Energy (LE) trigger, High Energy (HE) trigger, Outer Detector (OD) trigger and so on. Since the data acquisition (DAQ) system which was used in SK-I to SK-III was upgraded for SK-IV, they must be discussed separately.

2.6.1. DAQ in SK-I to SK-III

The front-end electronics of the ID PMTs for SK-I to SK-III is the analog timing module (ATM) [35]. One ATM has 12 channels of the charge-to-analog converters (QACs) and time-to-analog converters (TACs): they record the integrated signal charge and signal arrival time for each channel, respectively. A total number of 960 ATMs for the ID PMTs were used.

For each hit PMT, a 200 ns rectangular pulse with a 15 mV pulse height is generated by a discriminator stage. The ATM outputs the analog sum of all the rectangular pulse (HITSUM). Then, an event trigger is issued if the sum of HITSUMs from all ATMs exceeds a trigger threshold. Once the event trigger has happened, each ATM starts to digitize and record the time when the hit PMTs signal surpasses the threshold and the charge integrated in a 400 ns time window around the PMT trigger timing.

In order to avoid missing successive events such as Michel electrons, two switching pairs of both the QAC and TAC are prepared for each channel and managed by a channel control chip, as shown in Figure 2.15, because the process time for one channel is 5.5 μs. The time window for events is 1.3 μs wide centered around the event trigger in a [-400 ns, +900 ns] fashion, where 0 ns corresponds to the event trigger.

The signal arrived from 400 ns to 900 ns after the hit is neglected in order to ignore a known cable reflction pulse caused by an impedance mismatch between ATMs and PMTs.

The ADC/TDC output data have 12 bit (4096 channel) resolution. The ATM has about 450 pC dynamic range for charge, with a resolution of 0.2 pC, and about 1300 ns dynamic range in timing, with a resolution of 0.4 ns. To maintain accuracy of the timing and charge information, conversion tables are used (instead of fitted linear functions) to convert ADC and TDC counts to pC and ns, respectively.

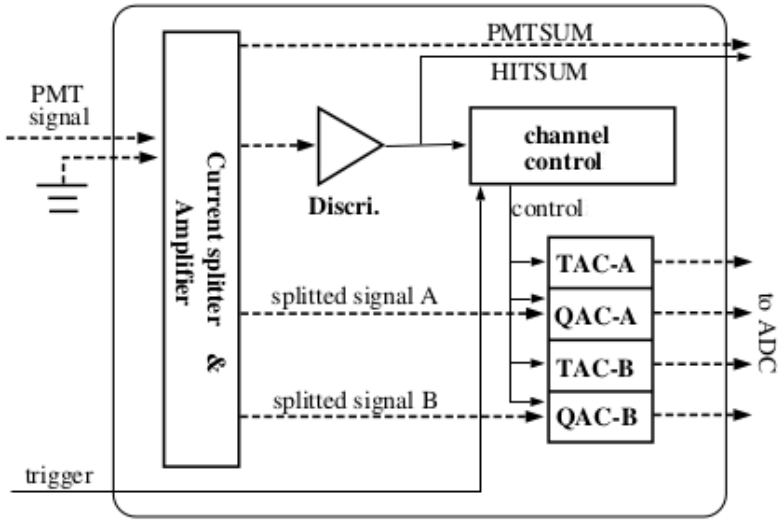

Figure 2.15: Schema of the analog input block of a single ATM channel. Dashed arrows show the PMT signal, its split signals, and accumulated TAC/QAC signals. Solid arrows show the logic signals which control the processing of the analog signals.

The temperature dependence of ADC and TDC pedestals (offsets) is linear and less than 3 count/C (0.6 pC/°C) and 2 count/°C (0.8 ns/°C), respectively, in the typical ambient temperature range. To correct for the temperature dependence of

the ADCs and TDCs, pedestal data are taken every 30 min in Super-Kamiokande and the measured pedestal values are used to convert ADC and TDC counts within each half-hour period. Ambient temperature is kept at about 27 °C±0.5 °C in the electronics huts. The inaccuracies introduced by temperature dependence are estimated to be less than 0.3 pC and 0.4 ns for the charge and timing information, respectively. Similar to the ATM system, signals from OD PMTs are processed by charge-to-time converter modules. When an event trigger happens, the time and charge information are converted to digital by multi-hit time-to-digital converter modules (LeCroy 1877).

2.6.2 DAQ in SK-IV

Since the ATM has an electronics dead time and a cable reflection issue, a new QTC-Based Electronics with Ethernet (QBEE) was developed and installed for both the ID and OD PMTs. One QBEE module has 24 channels, and each channel consists of a custom charge-to-time converter (QTC) and a multi-hit time-to-digital converter (TDC). The timing and charge resolutions of the QTC are 0.3 ns for 2 pC and about 0.2 pC for below 50 pC, respectively. The charge dynamic range of the QTC is 0.2 - 2500 pC, and the charge non - linearity is better than 1% for the overall range. The QTC records all the hits and immediately integrates the charge from the signals in a 400 ns time window for each hit, and TDC converts the QTC output into the digitized time and charge. The digitized time and charge are recorded only after a software trigger has been issued. The software trigger is issued when the number of hit PMTs in a 200 ns sliding time window (N_{200}) exceeds a threshold. In this system, the SLE, LE and HE triggers are defined as well as in the previous epochs. In addition to these triggers, Special High Energy (SHE) and After Trigger (AFT) triggers were introduced: the AFT trigger is issued only for an event triggered by a SHE trigger without an OD trigger and saves an additional 500 μs of data. A summary of SK-IV software triggers is shown in Table 2.3.

Trigger type	N_{200} threshold	Time window (μs)
SLE	34 $\rightarrow$ 31	-0.5 $\sim$ +1.0
LE	47	-5 $\sim$ +35
HE	50	-5 $\sim$ +35
SHE	70 $\rightarrow$ 31	-5 $\sim$ +35
LE	47	-5 $\sim$ +35
AFT	SHE without OD	+35 $\sim$ +535
OD	22 in OD only	-5 $\sim$ +35

Table 2.3: Software triggers used in SK-IV. The thresholds for the SLE and SHE triggers were lowered in May 2015 and September 2011 respectively.

Chapter 3

The calibration response to electrons in Super-Kamiokande, is carried out periodically thanks to a LINAC that accelerates known energy electrons in predetermined positions in the water volume. It is necessary to rebuild these electrons position while evaluating the corresponding energy resolution obtained. Unfortunately, the current system suffers from many limitations due both to the insufficient precision in aligning and steering of the electron source beam, and to the long times required to obtain it. As part of my thesis activity I took part to the latest calibration campaigns carried out with the current system.

3.1 Calibrations

The detector calibration is important: SK is calibrated via a number of sources, all of which are essential for its stable operation. Water transparency is monitored using a titanium–sapphire laser to illuminate a diffuser-ball light source, and measuring signals recorded by a CCD camera. Later in the experiment light scattering and absorption parameters are measured by a set of dye/N2 lasers.

The relative gain of individual PMTs is monitored using a scintillator ball illuminated by a Xe lamp. Relative timing is calibrated by a fast pulsed nitrogen laser light source connected to a diffuser ball. The diffuser ball is carefully designed to minimize time spread of emitted light. In addition to elementary calibrations of PMT performance, a number of calibrations are required to fix the absolute energy scale and other parameters needed for the various physics analyses. For this purpose several independent calibration systems are used [36][37]. Particularly, the solar neutrino data analysis requires precise knowledge of energy scale, resolution and detection efficiency for low energy (few MeV) electrons. A linear accelerator (LINAC) was installed at SK to

provide precise detector calibration with single electrons of known energy and direction at various positions in the detector volume.

3.1.1 LINAC description

SK's predecessor, Kamiokande, used gamma-rays from the Ni(n,γ)Ni reaction for the calibration of its absolute energy scale. Uncertainties in branching ratios and the neutron absorption cross sections for different nickel isotopes limit the accuracy of such an energy calibration to 1–2%. Nickel calibration also provides no information on the angular resolution of the detector and only limited information on energy resolution. The angular resolution as a function of energy is used to fit the distribution of event directions with respect to the direction to the Sun. This fit is fundamental to the solar neutrino analysis in SK.

The LINAC offers the means to study the detector response to electrons, its position dependence and angular resolution in situ. It allows the injection of single electrons of well-controlled energy at various positions in the ID. The LINAC covers the energy range of solar neutrino events and provides an excellent calibration of the absolute energy scale.

The very precise energy calibration is available in LINAC calibration, however, the setting of LINAC is a hard task and the beam direction is only downward. The LINAC employed at SK is a Mitsubishi ML-15MIII produced for medical purposes in 1978. It was used at the hospital of Miyazaki Medical University until its installation at the SK detector in 1996. Certain modifications were necessary to adapt the LINAC to its new purpose. It is now mounted on a solid support structure in a tunnel to the side and slightly above the top of the steel tank containing the water Cherenkov detector.

Single electrons are needed in the detector. A special electron gun reduces the number of electrons entering the acceleration tube to appropriate levels. Its output current is adjustable, allowing control of the beam intensity.

Electron from the electron gun are accelerated in the tube. Manipulating the input power and frequency of the microwave changes the average beam momentum. The electron energy can be adjusted in a range from 4 to 18MeV, well matched to recoil electron energies from solar neutrinos.

The beam pipe is evacuated to less than 10^{-7} torr, and the desired beam size and momentum are obtained by collimators and magnets: after the accelerating tube, the electron beam is rather divergent and spans a modest momentum range.

Mono-energetic electrons are selected from this spectrum by an arrangement of collimators surrounding D1, the first 15° bending magnet (Fig. 3.1).

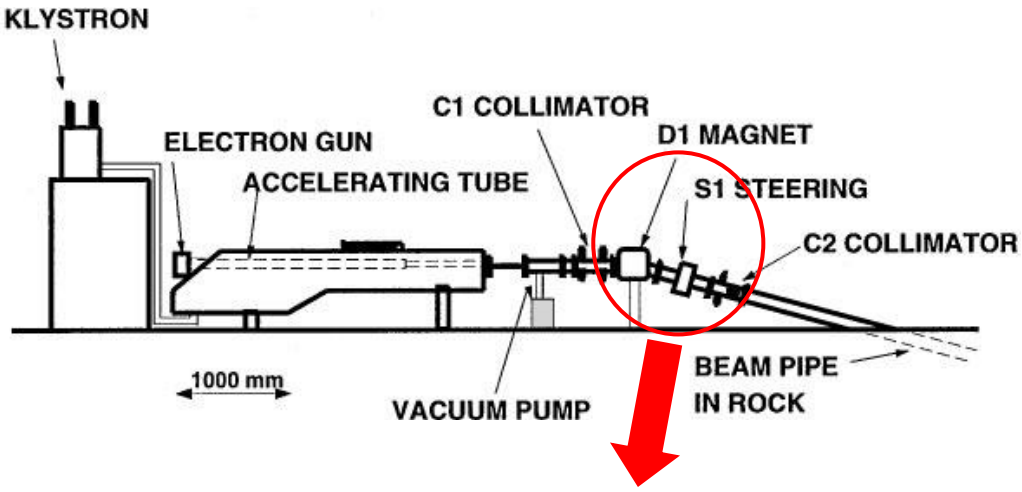

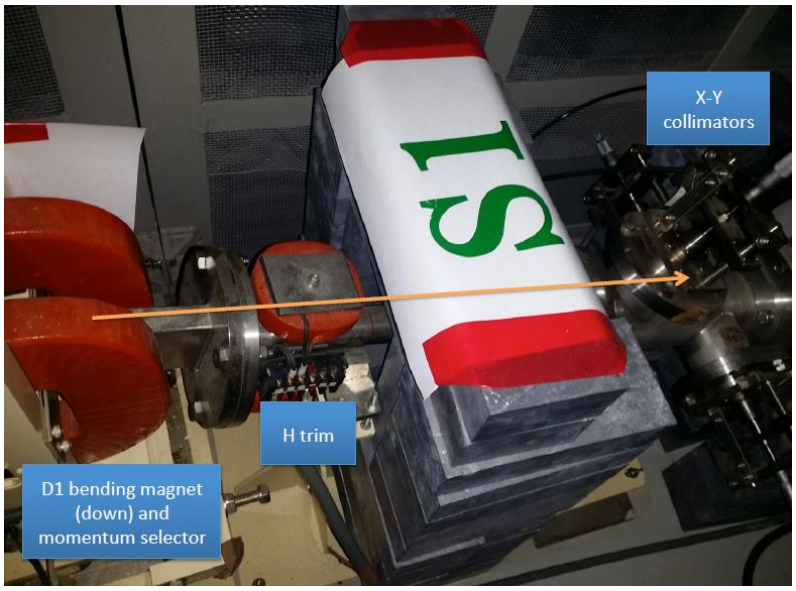

Fig. 3.1 Beamline detail: First bending magnet (D1) and associated collimators.

After the C3 collimator (Fig. 3.2), the beam momentum spread is reduced to 0.5% at FWHM. Steering magnets S1 and S2, installed after D1 and D2, respectively, are adjusted to keep the beam on the pipe axis (Fig. 3.2), (Fig. 3.3).

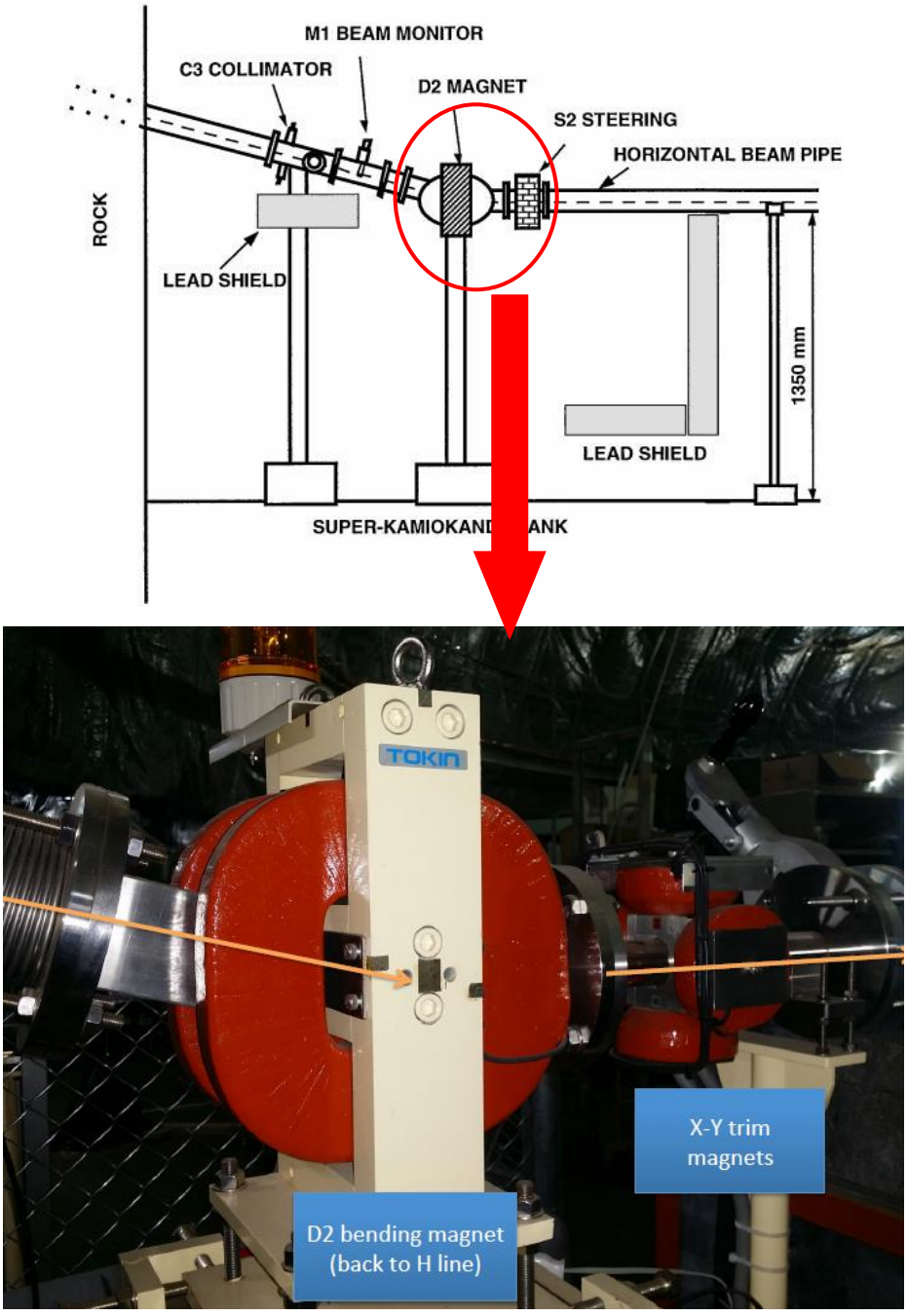

Fig. 3.2 Beamline detail: returning the beam to horizontal after momentum selection.

Constraining beam momentum and divergence reduces the beam intensity from ~10^6 to a few electrons per microwave pulse. Thus almost the entire beam intensity is either dumped into collimators or deflected out of the beamline by the magnet. If any gammas generated in this process were to reach the ID, additional light from their Compton electrons would produce correlated background, altering the energy calibration.

To shield the detector from this radiation, the beam pipe passes through 9 m of rock after the 15° downward bend in D1 before it emerges on top of the SK detector. There it is bent back to horizontal by D2, also a 15° bending magnet (Fig. 3.2). Gammas travelling towards SK in the inclined section of the beampipe before D2 are absorbed in a lead shield. After D2, the electrons travel in a horizontal beam pipe along the top of SK.

A 90° bending magnet, D3, bends the horizontal beam into this vertical beam pipe. Before and after D3, sets of quadrupole-magnets (Q-magnets) focus the beam onto the endcap of the vertical beam pipe in the tank (Fig. 3.3) [39].

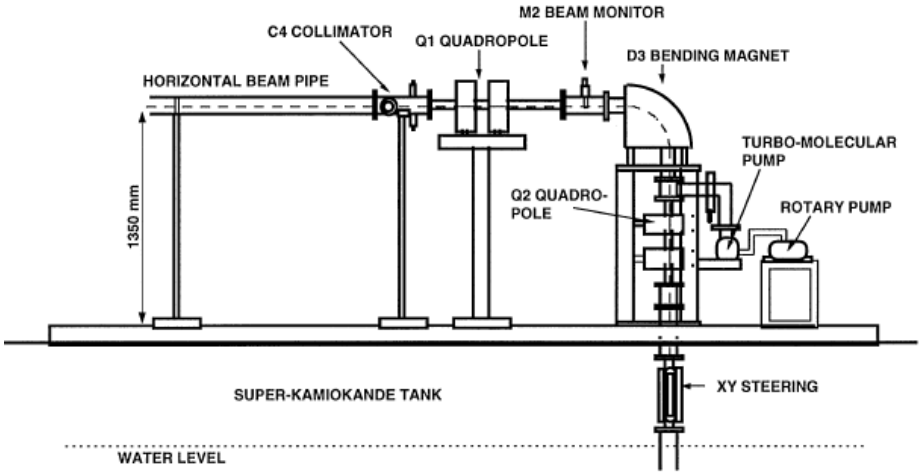

Fig. 3.3. Beamline detail: 90° bending and focussing of the beam.

The endcap of the beam pipe is closed by a 100 μm thick titanium window of 3 cm diameter. Plastic scintillators acting as a trigger counter and veto counters are placed at the end of the beam pipe as shown in Fig 3.4. A 1 mm thick, 24

mm diameter plastic scintillator (the trigger counter), is mounted 17 mm above the titanium window and supplies a trigger signal. LINAC triggers are issued if a trigger counter hit coincides with a LINAC microwave pulse. Four scintillators of 1 cm thickness surround the beam 80 cm above the trigger counter. They are used when steering the beam onto the trigger counter.

The beam intensity is adjusted to 0.1 electron per bunch so that almost all events are single electron events. The maximum rate of bunches is 60Hz.

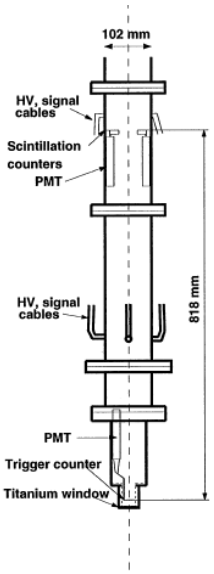

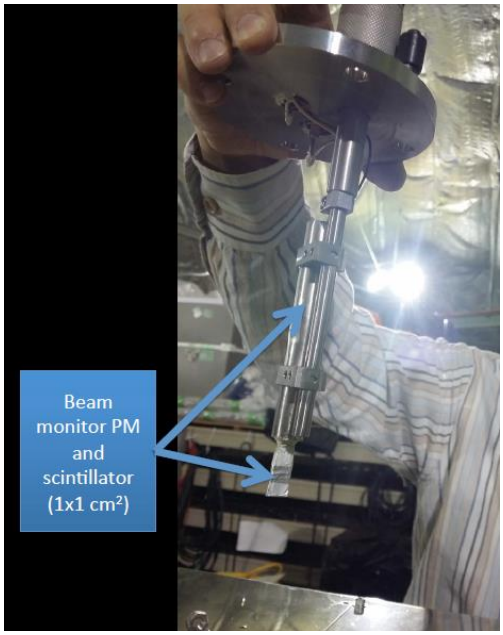

Fig.3.4 Beamline detail: endcap

Calibration holes reaching through the OD into the ID at regular intervals allow insertion of a vertical beam pipe of variable length (Fig.3.5) : on the top of the Super-Kamiokande tank holes are welded every 2.1m along the x-axis. The vertical axis of the detector is the z-axis and the origin is placed at the center of the ID.

Fig.3.5 Beamline detail: the vertical pipe sections

The calibration holes are offset from the radial x-axis by one PMT spacing (0.707 m). Only three of these holes were used in the current SK calibration.
The vertical beam pipe is inserted into the detector through these, and the length of the vertical beam pipe is variable, so we can do LINAC calibration at various positions in the inner detector (Fig. 3.6).

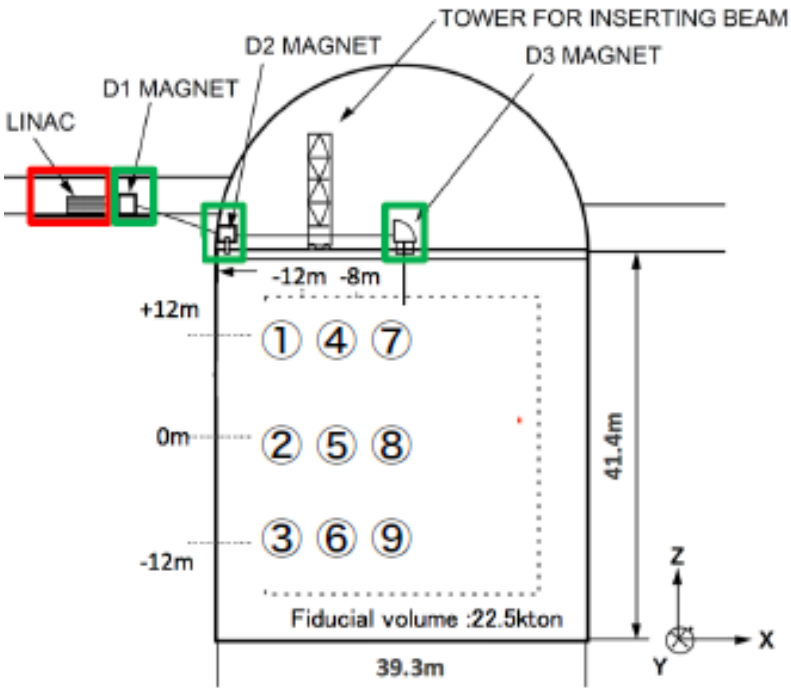

Fig. 3.6. The LINAC and its beam line at the SK detector.
The fiducial volume for the solar neutrino measurement is indicated by a dashed line. Black dots indicate where in the fiducial volume calibration data were taken with the LINAC

For each position data are taken at seven different beam momenta between 5 MeV and 18 MeV/c.

3.1.2 Beam energy calibration

For analysis using the solar neutrino energy spectrum, the systematic error of absolute energy scale must be less than 1%. In Super-Kamiokande, the advantage of the LINAC is that the electron energy is monochromatic and can cover the full energy range relevant for solar neutrinos, 5-18 MeV. Another advantage is that a direct calibration is available using electrons.

The LINAC calibration system injects single monoenergetic electrons into SK in the downward direction. Momentum-selected is precisely measured, in a second phase, by a Ge detector using an exact replica of the last part of the beam pipe.

The germanium detector used in the calibration is a Seiko EG&G Ortec GMX-35210-P, which has a germanium crystal of 57.5 mm diameter and 66.4 mm depth. The resolution of this germanium detector is 1.92 keV for the 1.33 MeV gamma-rays of ^{60}Co. The germanium detector is connected to a Seiko EG&G multi-channel-analyzer 7700. The germanium calibration system (crystal, electronics and multi-channel-analyzer (MCA)) is calibrated each time it is used. A variety of gammaline sources, spanning an energy range from 0.662 MeV for a 137Cs source to 9.000 MeV from the Ni(n, γ)Ni reaction, establishes the relationship between energy and MCA channel.

So, after data are taken at a certain position, the D3 magnet is removed and the vertical beam pipe pulled out of the tank. To calibrate beam energy, the last section of the vertical beam pipe (containing the trigger counter) is connected directly to the horizontal beam pipe, so that it lies horizontally rather than hangs vertically as in the tank. The germanium detector is placed right after the titanium window, and D1 is set to the same value as for the measurement in SK. Ge calibration relates D1 magnet settings to beam energies.

To determine the energy scale, data are compared to simulated events[38]: a MC simulation is used to evaluate the impact of energy loss and multiple scattering in the trigger counter, the titanium window, the beryllium window and the passive layer of the Ge crystal.

In Fig. 3.7, spectra recorded in the MCA are displayed for various beam momenta, as selected by the setting of the D1 magnet. Tails towards lower energies are due to electrons that are not contained in the Ge crystal. The simulation reproduces the width of the spectra to better than 10 keV.

Ge data were taken after each data position and energy. The reproducibility of the relationship between D1 magnet setting and beam energy is better than 20 keV.

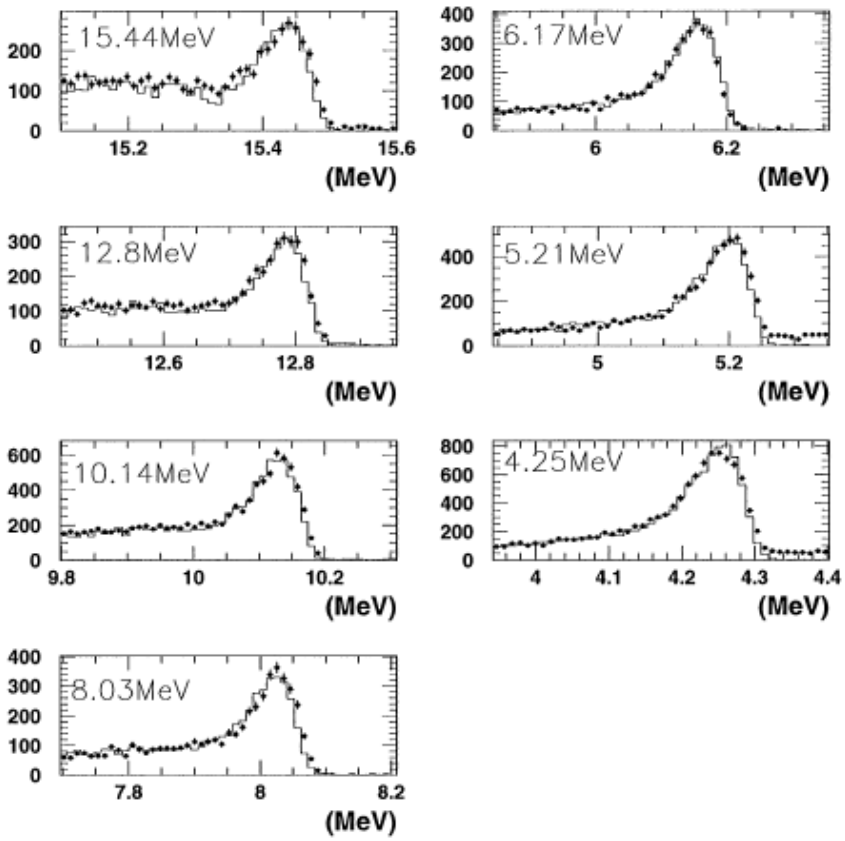

Fig. 3.7. Ge calibration data (points) and MC simulation (histogram) for LINAC beams of various energies: one bin corresponds to 10 keV.

3.2 Super-Kamiokande energy calibration by LINAC

The LINAC calibration system injects single monoenergetic electrons into SK in the downward direction. The energy of the momentum selected electrons is precisely measured by a germanium (Ge) detector using a thin titanium window similar to that used under the water (2.3.1).

To determine the energy scale, electron data are compared to simulated events: we cross-check the energy scale obtained from the LINAC energy with ^{16}N β/γ decays, which originate from the (n,p) reaction of ^{16}O with neutrons produced by a deuterium-tritium (DT) fusion neutron generator.

Also shown are the corresponding projections onto the x and z axes. To select the calibration data from this data set, one additional cut is applied to these LINAC trigger data to reject events with multiple electrons. If the timing information for the event is corrected for the time of flight (TOF) from the end of the beampipe, electrons that left the beampipe at times different by only a few tens of nanoseconds can be clearly separated. Examples for such TOF subtracted timing distributions are shown in Fig. 3.8. Events are rejected if multiple peaks of more than 30% of the expected signal are found more than 30 ns apart in a single event. About 5% of the LINAC trigger events are rejected by this cut.

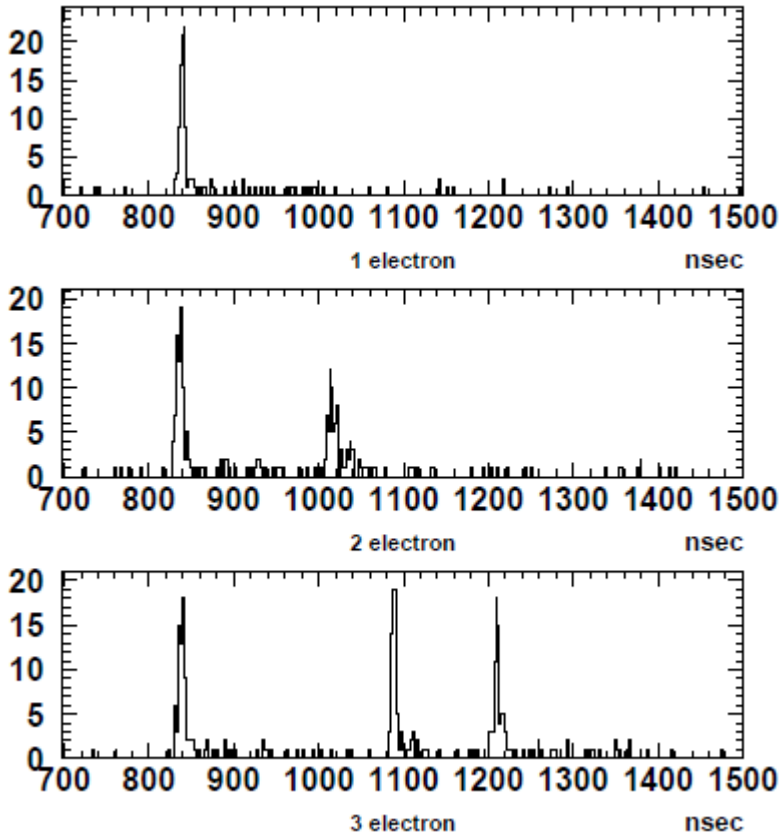

Fig. 3.8. Examples for TOF subtracted timing information for LINAC events containing one, two and three electrons.

The resulting set of LINAC calibration data for the various positions and energies is used in two ways. First, it is used to tune parameters in the detector simulation; second, it is used to evaluate systematic errors from the remaining discrepancies. While the LINAC provides samples of data for limited sets of

positions and energies and (until now) only one fixed direction, a single MC description covers the whole range of solar neutrino events. LINAC calibration data and MC simulation output, from now on will be referred to as LINAC and MC. MC simulation is based on GEANT version 4.10.5 [41].

Calibration equipment is included in this simulation. All MC shown in the figures uses the current best set of tuned parameters. New insights in details of the detector response may change this MC description and the derived parameters.

An example of MC and LINAC vertex distributions in terms of distance from the beampipe end position to the reconstructed vertex is shown in Fig. 3.9.

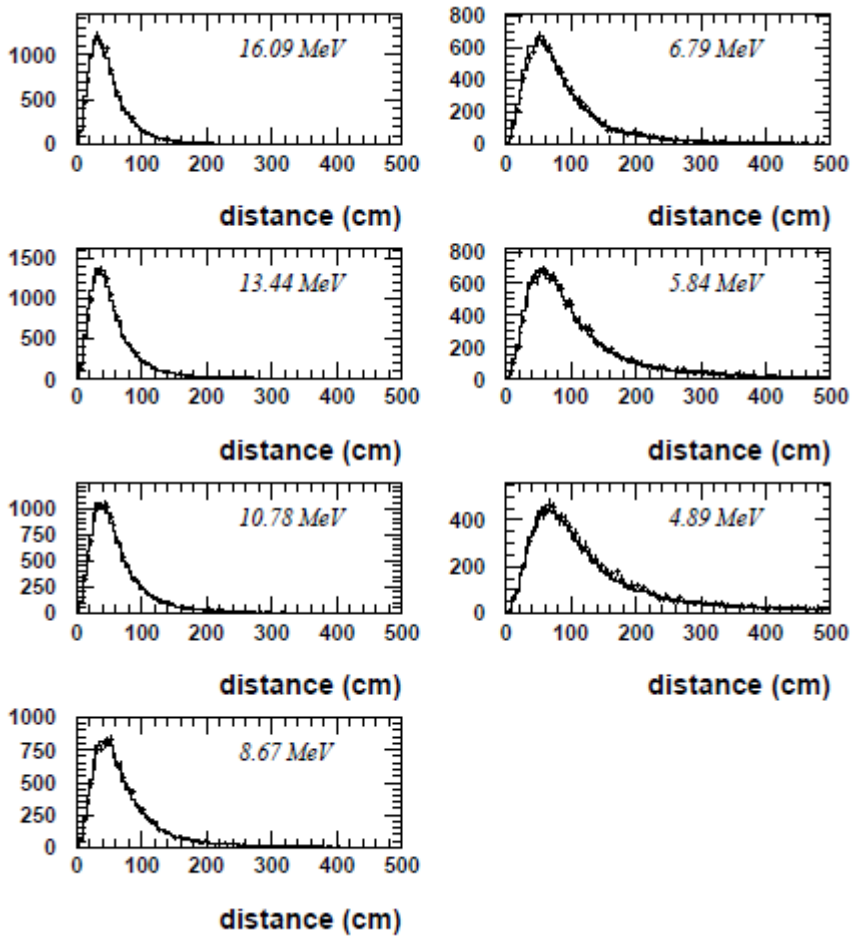

Fig. 3.9. Vertex distributions for (x,z)=(-12m,+12m). Histogram is MC, points LINAC

Fig. 3.10 shows the vertex resolution for all positions as a function of energy and the relative differences between MC and LINAC. Vertex resolution is defined as the radius of the sphere around the beampipe end position that contains 68% of the reconstructed vertices. Errors in the position averaged diagram reflect the spread (RMS) of values deduced for the individual LINAC positions.

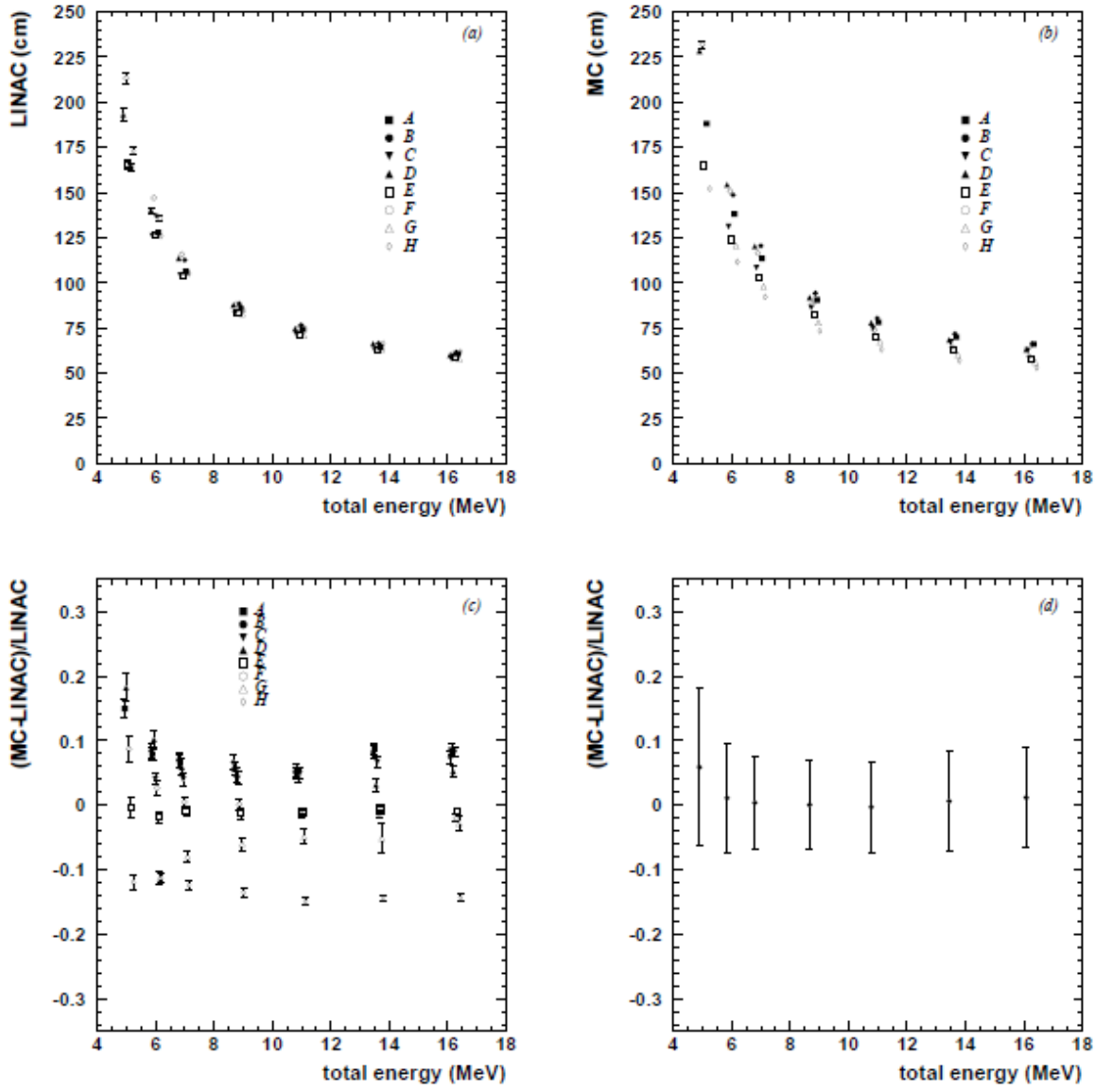

Fig. 3.10. Vertex position resolutions of (a) LINAC and (b) MC. A–H. (c) shows relative differences for all positions over momentum, (d) averages over position. Errors in (a)-(c) are statistical, while in (d) it is the RMS of the spread over positions in (c).

Many MC parameters have influence on the energy scale. Its position dependence is mostly affected by Cherenkov light attenuation, while the overall scale is adjusted by the PMT collection efficiency. At short wavelengths, the attenuation length is limited by scattering. MC tuning fixes it at 59.4 m for 380 nm. The same result is obtained from a direct measurement in the SK tank, yielding 59.4±1.6 m at this wavelength. PMT quantum efficiency and the reflectivities of various detector materials are put into the simulation from direct measurements. MC and LINAC reconstructed energy distributions overlaid for one position in the tank are shown in Fig. 3.11.

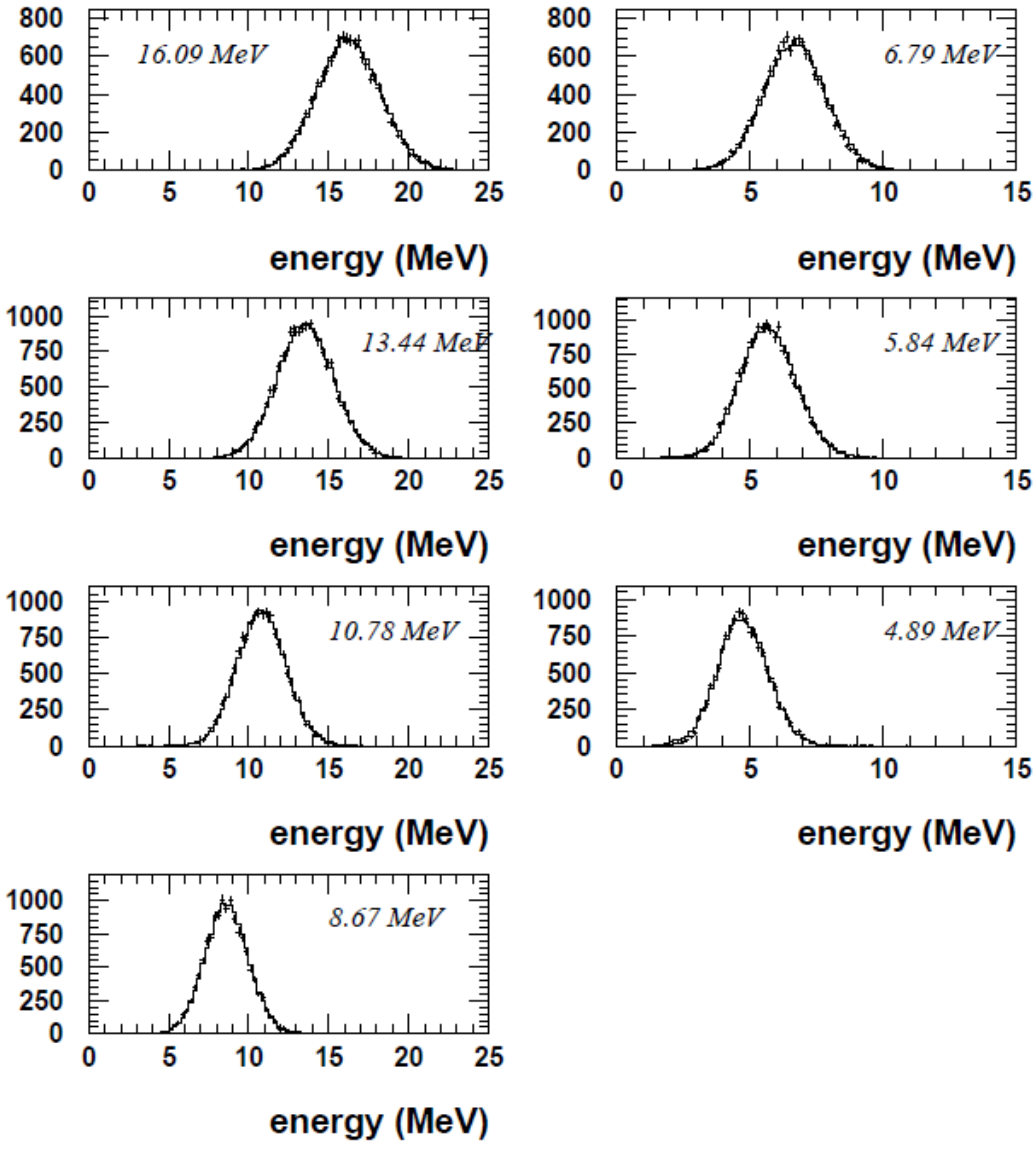

Fig. 3.11. LINAC (crosses) and MC (histogram) energy distributions for (x,z)=(-12m,+12m).

Fig. 3.12 compares absolute energy scales as a function of both energy and position.

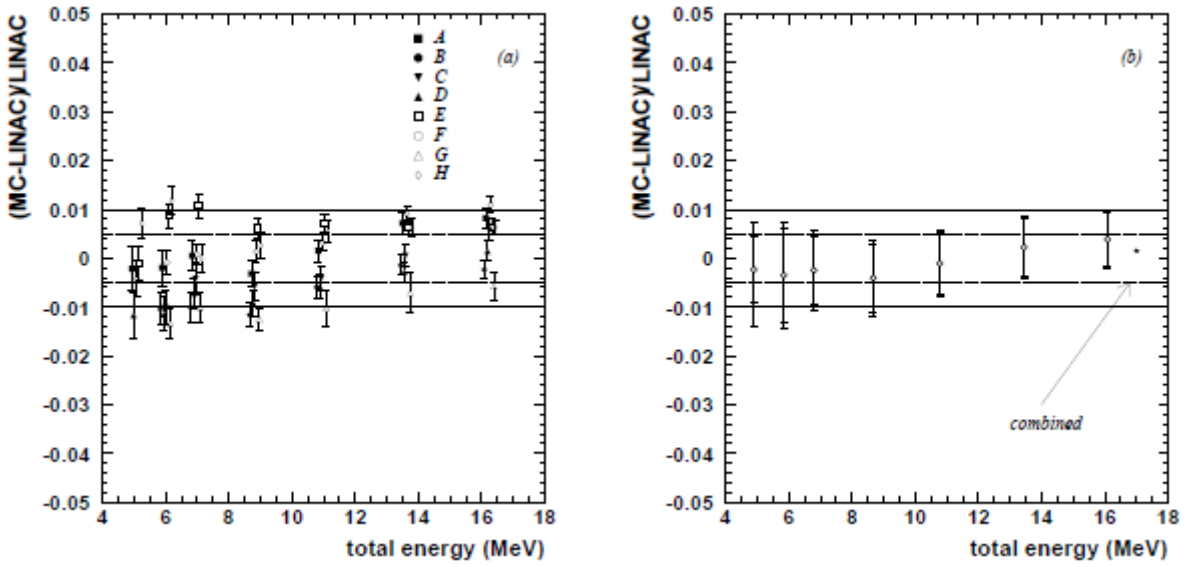

Fig. 3.12. Comparison of absolute energy scales for LINAC and MC:
(a) Only statistical errors. (b) The position averages.

For this comparison, MC and LINAC distributions, like the ones shown in Fig. 3.11, are reduced to peak value and width by a Gaussian fit around the center. In Fig. 3.12 within errors, the central value is always within ±0.5%. This increase in error is due to uncertainties in the reflectivity of the beampipe endcap's materials. The most serious difficulty is the reflectivity of the endcap. At 5 MeV, about 5% of the Cherenkov photons emitted by an electron leaving the beampipe will hit the endcap: recent tests revealed that there is some danger for a bubble of air to be trapped within the rim closing the seal of the titanium window. Thus, although the reflectivity of the steel beampipe and the titanium window were measured, the presence of a bubble of air of unknown size in front of it would change the situation significantly.

Estimates for the systematic error of the absolute energy scale are given in Tab. 3.1. With uncertainties of the energy loss in the beam pipe endcap estimated to be 2 keV, and 1.5 keV from the calibration of the germanium detector, the

reproducibility of the momentum selection in D1 with 20 keV dominates the uncertainty in the LINAC beam momentum.

beam momentum (MeV/c)	fraction hitting beam pipe	error due to reflectivity	total systematic error
5.08	4.7%	±0.68%	±0.81%
6.03	3.3%	±0.40%	±0.55%
7.00	2.2%	±0.28%	±0.44%
8.86	1.3%	±0.18%	±0.33%
10.99	0.88%	±0.11%	±0.27%
13.65	0.67%	±0.08%	±0.24%
16.31	0.51%	±0.06%	±0.21%

Tab.3.1. Systematic errors at the various LINAC momenta. The first column shows beam momentum, the second the fraction of Cherenkov photons hitting the beam pipe, the third the systematic error due to uncertainty of the reflectivity of the endcap, and the last the resulting total systematic error in the derived absolute energy scale.

Angular resolution is another quantity that is not tuned directly. Fig. 3.13 shows the opening angle between the reconstructed particle direction and the direction of beam injection for MC and LINAC at a chosen position.

Angular resolution is defined as the opening angle of a cone around the beam direction which contains 68% of the reconstructed directions.

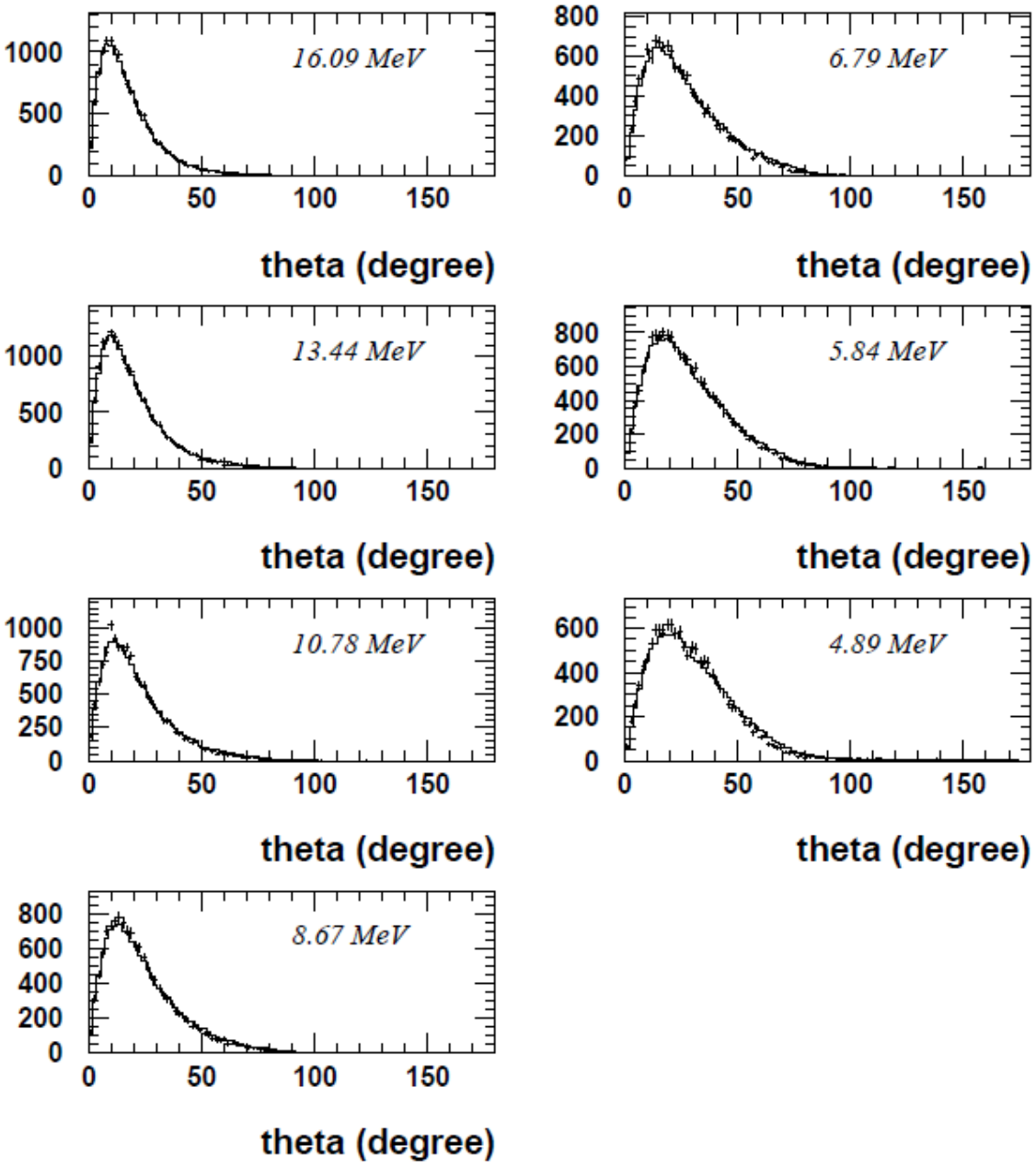

Fig. 3.13 Angular distributions for (x,z)=(-12m,+12m). Histogram is MC, points LINAC.

3.2.1 Results for the year 2018 on the analysis of data relating to the calibration campaign

During the data taking campaign I took part in, electrons were injected in SK according to the following table 3.2.

	Position[cm]			Target beam energy [MeV]					
2017	x [cm]	y [cm]	z [cm]	5	6	8	12	15	18
①	-1237	-70.7	1197	●	-	●	●	●	●
②	-1237	-70.7	-6	●	-	●	●	●	●
③	-1237	-70.7	-1209	●	●	●	●	●	●
④	-813.1	-70.7	1197	●	●	●	●	●	●
⑤	-813.1	-70.7	-6	●	-	●	●	●	●
⑥	-813.1	-70.7	-1209	●	●	●	●	●	●
⑦	-388.9	-70.7	1197	●	●	●	●	●	●
⑧	-388.9	-70.7	-6	-	●	●	●	●	●
⑨	-388.9	-70.7	-1209	●	-	●	●	●	●

Table 3.2: beam positioning in the SK confident limit and LINAC beam energy

A run (corresponding to certain values of position and energy) typically contains a sample of about 25,000 electrons.

The two main sections of the beam pipe are the horizontal one, whose length defines the radius at which the electrons are injected and the vertical one, which determines the depth. The vertical part contains, at the exit point of the electrons, a thin scintillator used as a trigger which is useful during the analysis to identify the calibration events. To minimize straggling phenomena, the electron exit window is a thin titanium diaphragm (100 μm).

After the data have been acquired in a certain position and at a certain energy (from 1 to 9 in figure 3.6), the magnet D3 is turned off and the beam is sent horizontally to a germanium detector; the horizontal exit window reproduces exactly the one that is used in the vertical beam pipe. In this way it is possible to obtain an effective energy measurement of the beam with the best possible accuracy. The LINAC configuration guarantees that the energy spread is

negligible.

LINAC data are reconstructed using the standard solar neutrino analysis chain [40]. A resulting typical two-dimensional projection of the vertex distribution onto the x,z-plane (SK coordinates) for LINAC trigger events is shown in Fig. 3.14: the electron position within the volume (X, Z) is measured using the same reconstruction program (named BONSAI) used for the analysis of solar neutrino events [42].

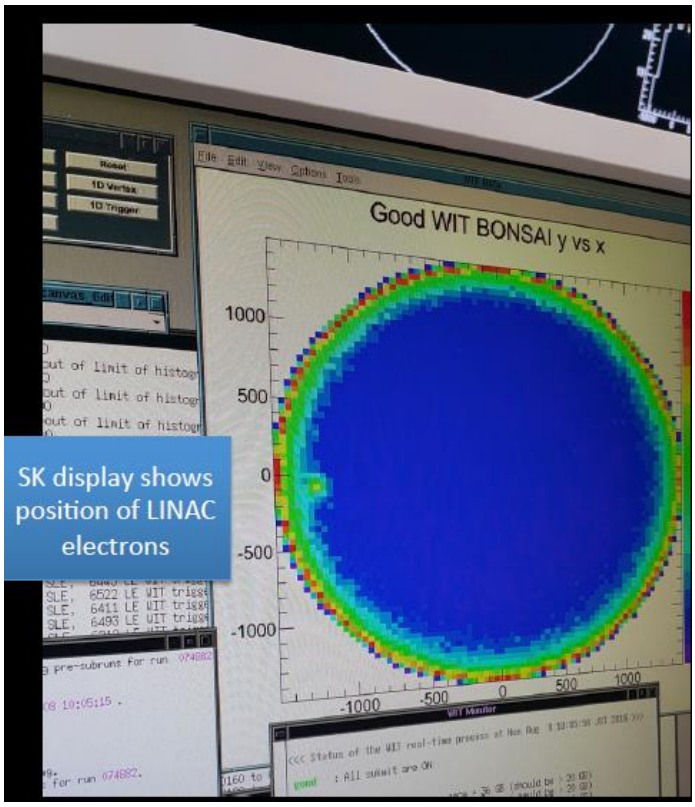

Fig. 3.14: the electron position the reconstruction program BONSAI

After all energy points have been taken at certain position, the D3 magnet is removed and the vertical tube extracted from the tank, in order to insert in the next position. For each position and at the energies shown in the table 3.2, I was therefore able to create a series of two-dimensional distributions such as those shown in Figure 3.15, which show the typical distribution of the vertices on the x, z plane of the events generated by the LINAC. The distributions width allows us to make a first estimation of the spatial resolution obtainable by the instrument, while the position of the peaks, coinciding with the nominal value,

indicates that the possible biases are small or negligible because they are compatible within one sigma with the nominal position.

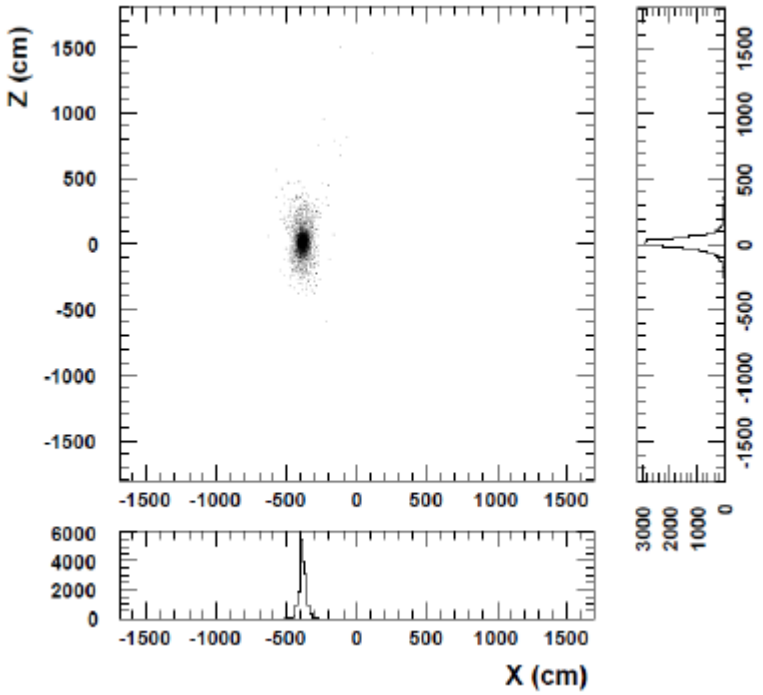

Fig. 3.15 position vertex a (x,z)=(-4m,0m), beam energy to 15MeV/c

Then using the official collaboration Monte Carlo based on GEANT it has been possible to compare the experimental distributions with those simulated under comparable conditions. For the Monte Carlo, 50,000 electrons were simulated for each position and energy. As can be seen in the example shown in figure 3.16, the comparison was generally satisfactory.

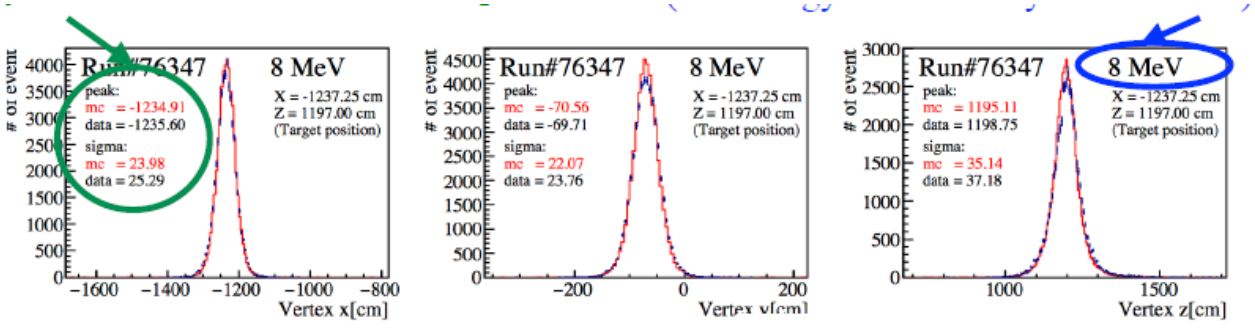

Fig. 3.16: Energy distribution related to a MC per (x,y,z)=(-12m,0m,12m) and to a 8MeV energy.

The top three plots compare the data (in black) and the renormalized MC (in red) relating to a given XZ position of the 8MeV run (nominal energy). Here the agreement is evident.

After the comparison for each energy and each position between the experimental distributions and Monte Carlo simulations, we can check resolution for all positions as a function of energy and the relative differences between MC and LINAC (fig.3.17) where vertex resolution is defined as the radius of the sphere around the beampipe end position that contains 68% of the reconstructed vertices. Errors in the position averaged diagram reflect the spread (RMS) of values deduced for the individual LINAC positions.

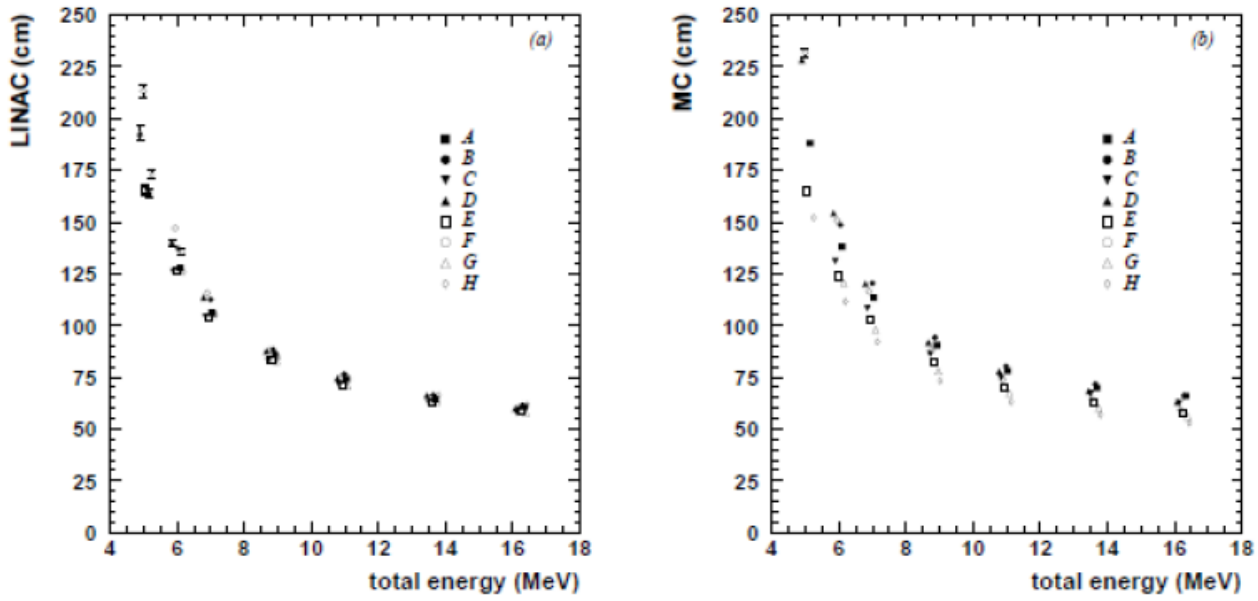

Fig. 3.17. Vertex position resolutions of (a) LINAC and (b) MC

Recording calibration data with the LINAC for the various positions and energies has essentially two purposes: first of all, these data are used to make a precise evaluation of the systematic errors associated with solar neutrino measurements, secondly they allow the best detector modeling response in order to be able to reproduce both the position-energy values directly measurable with the LINAC and the characteristics of any other element of the detector.

In particular, for each energy value the following spatial resolution relative to

the position of the electron beam, shown in the table, has been calculated 3.3:

Total energy (MeV)	Vertex resolution(cm)
5	121±21
6	133±8
8	108±5
12	73±2
15	65±2
18	50±2

Table 3.3: Spatial resolution on the position of the beam depending on the energy scale (experimental values)

The analysis of this last calibration data campaign is not complete yet, but a first estimate has made it possible to evaluate an error to the energy scale equal to 0.46%, in agreement with similar measures carried out in the past.

Chapter 4

As mentioned, one of the problems in the SK detector calibration is the time required for the measurement campaign. It takes about two hours to collect the statistics required for a given energy value and many more for the assembly, movement and reassembly of the beam pipes and the beam realignment between one measurement and another.

The current calibration procedure with the LINAC, described in the previous chapter, is extremely laborious; a lot of time is needed for beam alignment and magnet current tuning. In fact, the very low energies and the poor stability of the beam imply an extreme sensitivity to any small current variation of the magnets. The use of a sequence of detectors able to measure the position and not a simple count (as it happens now), would allow to obtain a beam profile and to understand, much better its optics. This would allow to considerably shorten the time required to set the operating parameters. Information on the profile in different positions would also make it possible to refine the beam simulation.

4.1 Beam monitoring detectors

The LINAC beam is generated behind a 9m-thick rock wall on a side of the SK cavern; the beam-line traverses the rock wall in a downward direction before a dipole magnet steers it in the horizontal direction above the SK tank.

Beam steering typically requires manipulating the D1, D2 dipoles and Q1 quadrupoles in an upstream-to-downstream order. To assist the steering the M1 and M2 beam-monitoring scintillators can be moved inside the beam path. Once the beam is collimated and centered on M2, the D3 bending magnet is set to steer the beam in the vertical direction. The Q2 quadrupoles and X-Y magnets are then used to center the beam on the trigger scintillator; in this last stage, which requires pointing the beam some tens of meters away from the last

available magnet and measurement point, the only available tools are the trigger scintillator itself and 4 veto-counters designed to intercept electrons hitting the beam-pipe wall. Given the small rigidity of the beam, the steering represents a sizeable fraction of the time dedicated to the LINAC calibration which - it is worth mentioning - obliges the SK detector to operate in a non-standard fashion. The M1 and M2 monitors are 1x1 cm^2 scintillators connected to a photomultiplier tube; this assembly is mounted on a vacuum flange through a rotary manipulator allowing to move the scintillator in the beam path when required. In its present form the beam monitors only provide indirect information on the beam shape and position by counting hits during an X-Y steering scan.

A position-sensitive and somewhat larger device would provide a complete characterization of the beam shape, envelope and position in real-time; these tools would likely shorten the beam-steering significantly. In addition a similar device placed in the final section of the vertical beam pipe, i.e. a hypothetical M3 monitor, would give a measurement point with much better lever arm than in the present situation.

For the reasons described above, during 2016 a new Position Sensitive Monitor (PSM) from LINAC was proposed and approved to be used it in Super-Kamiokande (SK) for electron calibration.

This project, carried out in jointly with the INFN groups of Bari and Rome, consists of a set of 3 monitors based on the concept of "gamma camera" (scintillator discs of ~2 cm in diameter with SiPM used as readout). Following this project, in these years of research, I studied simulation codes and measurements on a series of discs of scintillating material of different thicknesses (from 1 to 5 mm), diameter and light collection characteristics, in order to optimize the desired performances.

This is the list of requirements for a position-sensitive device to be installed in the SK LINAC:

- Position resolution: ~1mm
- Moved in and out the beam by a remotely-operated manipulation system, even when mounted in the final (underwater) vertical section
- Amount of material in the beam equivalent to the one of the present monitors, and possibly less
- Minimal cabling for power and data
- Larger active area (~ 2cm diameter)
- Time resolution and triggering capability comparable to the present system.

The most serious challenges posed by the requirements are the routing of several tens of readout channels and the remote operation in the underwater section.

We experimented with disks of 1 to 5 mm thickness, in step of 1 mm, in order to find the best compromise between amount of material, light yield and attenuation length, to optimize the area coverage and number of channels. The proposed detector is sketched in Fig. 4.1. The assembly would fit inside the present beam-pipe, mounted on hinges and remotely moved in and outside of the beam by a stepper motor with end-range switches.

A PCB will hold the front-end electronics and interfaces to the external readout system. A set of silicon photo-multipliers (SiPM) arranged in a circle will collect light from a central scintillator disk. The track position will be determined by computing the barycentre according to the amount of light received by each SiPM.

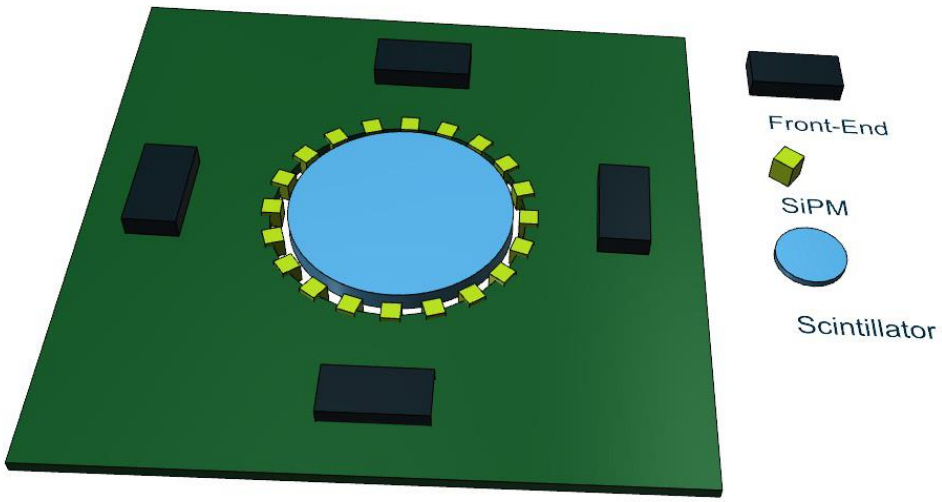

Fig.4.1 Conceptual scheme of a gamma camera as a SK LINAC beam monitor

The features of this kind of beam monitoring system are studied in this thesis with the help of GEANT4 simulations.

The detector consists of a monocrystal disk scintillators of p-terphenyl, read by a silicon photomultipliers. The scintillator may optionally be wrapped in a reflector. In the simulations various properties of the scintillator and the wrapping are varied like the scintillator thickness or the kind of wrapping and its reflectivity. Subsequently, the number of photons arriving at the SiPM is analyzed to determine the influence of the varied properties.

Finally, the results of the simulations are compared to determine the best configuration to use to assemble the monitor.

4.1.1 The p-Terphenyl scintillator

Organic scintillators are among the most common detectors for particles: these materials are capable of stopping electrons and positrons of few MeV within thicknesses of O(cm). Their scintillation light also has short decay times and is peaked in the blue region (400-450 nm), matching the Photomultiplier Tubes' (PMT) spectral sensitivity. Organic scintillators have Light Yields (LY) of few thousand photons per MeV of released energy. This value is lower than what can

be obtained with inorganic scintillators, but availability in large sizes and lower costs make organic scintillators preferrable. Aiming at closing the gap between inorganic and organic scintillators, we studied the properties of p-terphenyl, an organic material commonly used as a dopant for organic scintillators, as the main component of a scintillator for radiation detection. Crystals of this material have a LY that strongly depends on the doping: LY can be significantly increased at the cost of shortening the Light Attenuation Length (λ). P-terphenyl (1,4-diphenylbenzene) is an aromatic hydrocarbon isomer, formed by three benzene rings in ortho position. Pure terphenyl is a white crystalline solid, insoluble in water. Though polychlorinated terphenyls were used as heat storage and transfer agents, p-terphenyl is currently under investigation as a material to be used in opto-electronic devices, such as organic LED devices (OLEDs) and currently used in laser dyes and sunscreen lotions. In particle physics it has been used as a wavelength shifter, exploiting its sensitivity to VUV radiation, to read out scintillation light from liquid Xenon. Pterphenyl has also been used as a doping component for liquid scintillators. We investigated the scintillation properties of poli-crystalline p-terphenyl samples doped by 0.1% in mass of diphenylbutadiene, with respect to organic scintillators. The innovative aspect of our study is that p-terphenyl is the main component and not the doping agent. Due to this, the crystals we studied have short λ, due to reabsorption of scintillation light. A short light attenuation length could be a counter-indication for common uses of scintillators, where the scintillating material is also the transport mean for the scintillation light. However, different approaches could benefit from this property. In particular, deposition of scintillating material on a substrate, coupling to Wavelength Shifting fibers or substrates, or direct coupling to photodetectors will not be affected by the short λ. Moreover, dual-side readout of a crystal with charge-balance method could lead to the localization of the energy deposit along the crystal. The LY and λ parameters are a crucial input to the simulation of any detector built with such materials.

Simulation is particularly critical in this case because the short attenuation length makes the tracing of optical photons compulsory.

For our first experimental measurements, referring to the latest studies regarding new scintillators [43], we chose some discs entirely made up of P-terphenyl, whose main features are:

• Low density, comparable with that of plastic scintillators;

• a high Light Yield (LY);

• a short attenuation length.

Due to the small size of the device, the reason for this choice is that the use of a classic scintillator with a large attenuation length might be a disadvantage. In fact, an attenuation length much larger than the scintillator disk size would produce numerous reflections before the photons are collected at the periphery eliminating the ability to use the barycentre measurement of the signals collected to calculate the position on the disk of the incident electron.

Hence the idea of using pure P-Terphenyl crystals, due to its reduced attenuation length. In fact, this kind of scintillator is excellent for position measurements of low-energy charged particles as it emits a lot of light even if it quickly reabsorbs it. The idea behind using it pure is to have sufficient light in the peripheral SiPMs, despite the reduced absorption length, taking advantage of the attenuation to make the SiPM crown sensitive to the barycentre position.

4.1.2 Experimental setup and λ measurement

The aim of this campaign of experimental measures was essentially to verify that, using a P-Terphenyl scintillator, the collection of light is sufficient for our purposes and that the attenuation length is of the same order of magnitude as the dimension of the monitor that will soon be installed on the SK.

In this phase I had to evaluate the attenuation legth λ of this new material (the P -Terphenyl), in order to reconstruct the source track with the use of SiPMs

crown sensitive to the barycentre position.

These measurements consist in modifying the source position which generated a certain number of photons, moving it to several points and studying the variation in the number of photons arriving at SiPM.

A series of measurements have been carried out considering a very simple geometry: this geometry consists of disc of scintillator of 2.6 cm of diameter and thickness of 4 mm (figure 4.2), simply inserted in a frame equipped with a SiPM positioned on the perimeter; in this way it is possible to count the number of scintillation photons that will arrive on it.

The main parameters of the scintillator we used are listed below:

1. density: 1.23 g / cm^3
2. refractive index: 1.65
3. decay constant: 3.7 ns
4. Light yield 27,000 photons / MeV
5. wavelength of the emitted light: 420 nm

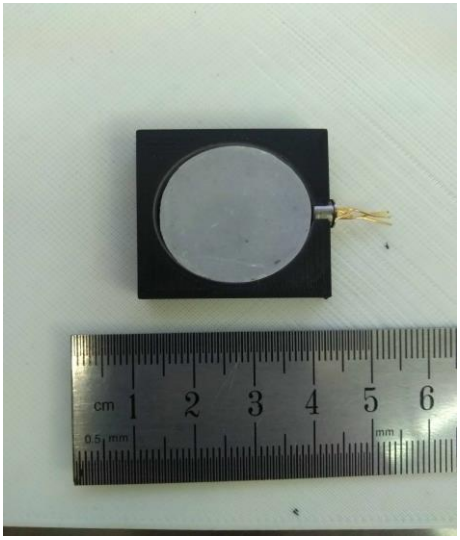

Fig .4.2 P-terphenyl sample of 2.6cm and thickness of 4 mm

P-terphenyl samples have been also combined with BC 630 optical grease to increase the total thickness T traversed by scintillation light.

To collect scintillation light, the samples were optically coupled to a SiPM MicroFC 10035 X18 (fig.4.3):

- 2x2 mm^2 size
- 576 microcell of 35um (fill factor 64%)
- Temp stability 21.5mV/°C
- Breakdown voltage ~24.65V
- Bias over-voltage 1-5 V
- Wavelenght 300-800nm, peak 420nm
- PDE 31%-41%
- Gain $3*10^6$
- Dark current rate 30KHz (<96KHz)

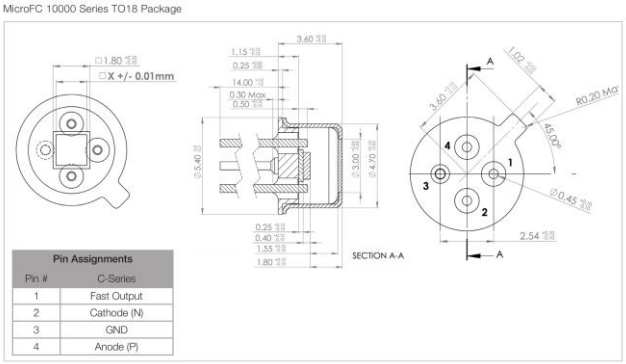

Fi. 4.3 Scheme of a SiPM MicroFC 10035 X18

In order to study the performances of p-terphenyl as a detector for electrons and photons, we exposed the samples to a Sr90-Y90 radioactive source.

The source is placed at various points on its surface: there are three impact points, the CENTER of the scintillator, the CLOSE positioned at the top near the photomultiplier and the one at the bottom, the FAR position, away from SiPM (figure 4.4).

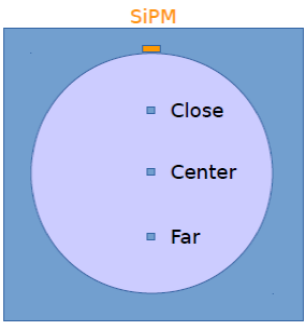

Figure 4.4: source impact point on the p-terphenyl disk

The SiPM was coupled to the perimeter with optical grease, while the other surfaces were covered with aluminized mylar. The source was placed in contact with the scintillator in order to reduce the material traversed by the radiation.

The investigated property of p-terphenyl is the Light Attenuation Length (λ) since it affects all other measurements. In order to measure it, a non penetrating radiation is needed since otherwise the measured quantity would be equal to the convolution between the penetration path distribution and the λ.

Measurements were made at a variable acquisition voltage threshold, from 800 µV to 5 mV set in the oscilloscope.

A first measurement was made without a radioactive source in order to acquire dark current events, and white noise.

Using a source of ^{90}Sr with activities of 74 kBq nominal the dependence of the response on the distance between the SiPM and the point of interaction of the particles was studied.

From the measurements carried out, the following quantities were recorded as a function of the position of the source collimated with respect to SiPM: frequencies with fixed threshold and histogram (therefore efficiency and average uncalibrated light): these measurements were made covering a certain range of thresholds to see how they are populated.

On the oscilloscope histograms have been acquired in which each peak corresponds to the number of photoelectrons that hit a SiPM cell: in particular, excluding the first peak that with auto trigger at 500 µV corresponds to white noise, each successive peak corresponds to a photoelectron, two to three photoelectrons and so on. Obviously, by increasing the threshold, we cut thermal noise and also the first peaks which, as we have said, represent the number of cells corresponding to the arrival of photoelectrons.

Every single cell turns on as soon as it is crossed by a photoelectron (or white noise): that is, it is photon counting, contrary to most photomultipliers.

Below are examples (fig. 4.5, 4.6, 4.7, 4.8) of the data acquired at different thresholds. In particular, counts were acquired for each position (corresponding to the number of times it was illuminated a SiPM cell, upon arrival of a photoelectron) as a function of the voltage per second. For each acquisition the counts were then normalized at the frequency with respect to the highest threshold (5mV), and the data finally presented as a frequency depending on the charge. Finally, the procedure was repeated for each position of the source with respect to the scintillator.

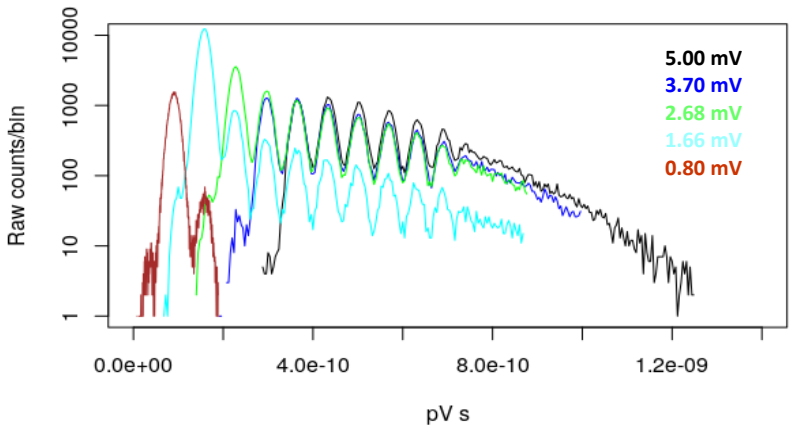

Figure 4.5: RAW COUNTS: Close position to SiPM

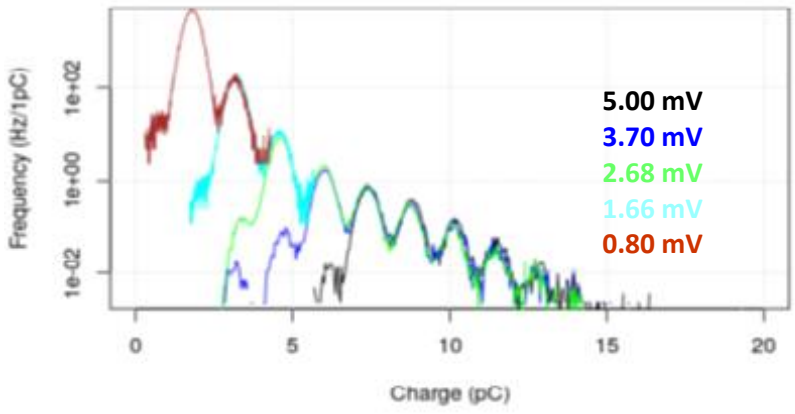

Figure 4.6 Close position (~7mm from SiPM)

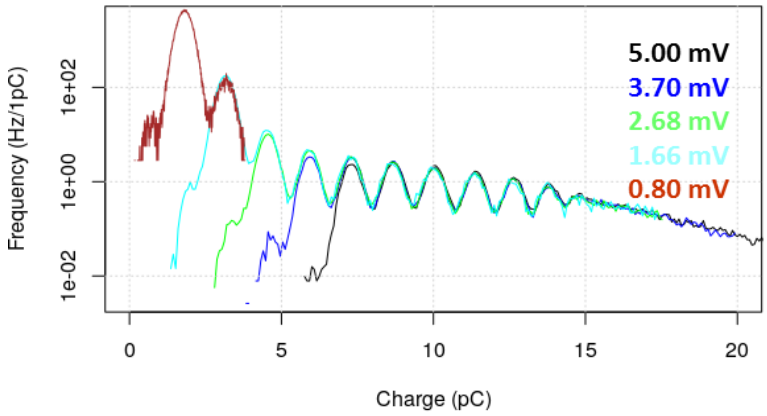

Figure 4.7 Far position (~21mm from SiPM)

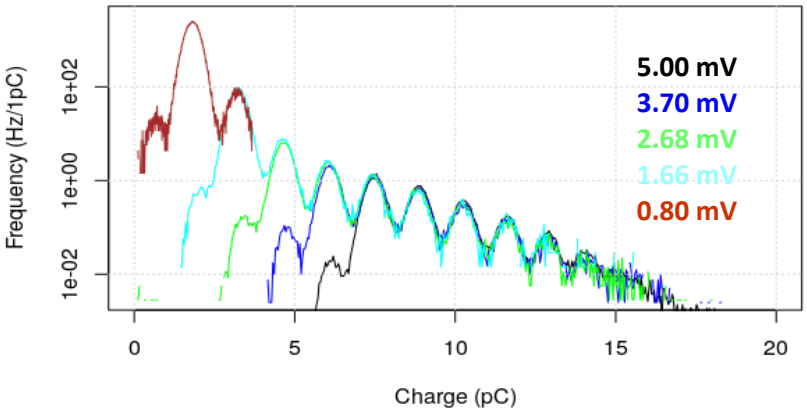

Figure 4.8 Center Position (~14mm from SiPM)

Having obtained a complete spectrum for each position, the three spectra are normalized taking as a reference the peak corresponding to a photoelectron. This allows us to understand how the spectra change as a function of distance and to approximately quantify the attenuation length.

Figure 4.9 shows, as an example of this procedure, the frequency graph as a function of charged for the three different positions of the source with respect to SiPM. Taking an arbitrary value of frequency (in this case 30Hz) it is possible to establish for each distance what is the number of photoelectrons corresponding to an event that occurs with that specific frequency. In particular, considering the "range" with a more linear trend, the average charge at the three points of the scintillator was calculated and whose values were inserted in the table on the right. In this way, it was possible to evaluate the attenuation length for the

scintillators with a diameter of 26mm and 4mm of thickness of p-terphenyl used in this series of measurements, which turned out to be of the order of one cm, compatible with the dimensions of the beam monitor to be realized for the calibration of the SK detector, verifying that a sparkling disk of this new material (p-terphenyl) and with this geometry is usable for our purposes.

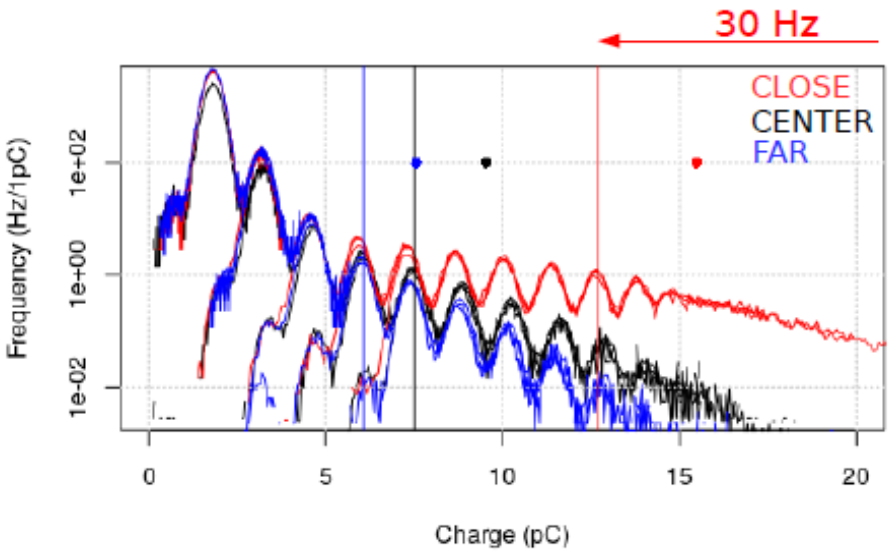

	Average 30Hz
CLOSE	15.48
CENTER	9.53
FAR	7.56

Figure 4.9 Compute the average charge for the upper tails of each distribution corresponding to 30Hz (arbitrarily chosen)

The attenuation length λ for p-terphenyl is of the order of one cm, compatible with the size of the new monitors for the calibration of SK, verifying that a scintillator disc of this new material (p-terphenyl) and with this geometry can be used for our purposes.

4.2 Simulation setup

I simulated, in the framework of GEANT4 [41], a configuration of the beam monitor referring to the campaign of experimental measurements on a series of scintillators coupled to some SiPMs, in order to evaluate the optimal parameters of these monitors for our purposes.

Geant4 (abbreviation for GEometry ANd Tracking) is a tool for Monte Carlo particle propagation and interaction simulations within a detector developed at CERN. As the name suggest, Geant4 includes tools for the definition and the treatment of geometry and detectors tracking and response: on one side it analyzes the physical arrangement of the experiment (detectors included) and it considers how this arrangement influences the path of the particles , on the other it simulates the passage of particles through matter assigning a probability to each of the possible interactions or the possible decay processes , and it finally records when a particle passes through the detectors volumes and how a real detector could respond. The advantage of this code compared to those previously used (Geant3 and Scidra) consists in the fact that, besides simulating the processes of interaction between radiation and matter (such as the photoelectric effect, Compton scattering, the production of pairs, ionization , the formation of Auger electrons, etc.), it allows to simulate the formation and transport of optical photons generated inside a scintillator.

For these purposes it provides a variety of interactions that may be included modularly into the simulation. The first step of a simulation is to create objects corresponding to the components of the detector. These so called Solids contain information about the object's geometry. Then a LogicalVolume is needed to store information about the material in the Solid. Additionally the volumes may be marked as sensitive volumes to generate Hits when a particle passes. These Hits provide functions for the user to gain information about the event when the

sensitive volume was hit. Finally the PhysicalVolume is created. This is the complete volume used for the simulation [41].

4.2.1 The scintillator and the SiPMs

Through simulations the properties related to the p-terphenyl scintillator for light collection by SiPMs were studied by varying some parameters:

- different sizes of a monocrystal disk scintillator (26mm diameter and 1-2-3-4-5mm thickness);
- different beam energy;
- different positon of the beam.
- the use of more photomultipliers coupled directly to the single plastic.

Scintillation photons are created uniformly in the solid angle and propagate arbitrarily through the scintillator. When they hit the surface of the scintillator on the inner side a part of the photons is reflected due to total internal reflection. To increase the number of scintillation photons that hit the SiPM the scintillator is wrapped in reflecting material because otherwise the photons that are being refracted would be lost. The reflectors used are a diffuse and a specular reflector, but to estimate the increase of detected photons when using a reflector measurements are taken with a scintillator wrapped in black felt. Small holes in the shape of the SiPM were cut into the wrappings to place the SiPM on the scintillator.

The entire process of image formation on the segmented SiPM can therefore be simulated through a single code, significantly reducing the timeframes and allowing simulating an increasing number of events to obtain better statistics.

To help the study of the performances for the monitor to be realized coupled with one or more SiPMs, some measurements were carried out with electron beams at well defined energies.

In fact, after the definition of the attenuation length parameter of the new material (the P -Terphenyl) and the study and the realization of the geometry of the detector, in this final phase I had to evaluate the behavior of the source, ie a beam of electrons with simulated radiation energy that can vary between 5 MeV and 18 MeV, as its position varies in relation to the geometry of the scintillator itself, in order to reconstruct the source track with the use of SiPMs.
The simulation tests that I carried out consist in modifying the source position which generated a certain number of photons, moving it to several points and studying the variation in the number of photons arriving at SiPMs.

4.2.1.a) Counting scintillation photons

A first simulation has been carried out considering a very simple geometry: this geometry consists of disks of scintillators of 2.6cm of diameter and variable thickness (1-2-3-4-5mm), simply inserted in a volume of air and equipped with a SiPM positioned on the perimeter; in this way it is possible to count the number of scintillation photons that the simulation predicts will arrive on it.
Simulations were performed with GEANT4 that allows to detect the number of photons collected by each SiPM. These photons are produced by electrons generated via particle gun and passing through the p-terphenyl disk: we could observe an increasing number of photons as the source approached SiPM and vice versa as it moved away.
By enabling only one photomultiplier at a time, I acquired the counts for each energy value at the three points established for the incident beam. After that, in order to verify that the simulation was returning similar results for both photomultipliers, I superimposed the graphs in which the number of photons is reported as a function dipending on the position (to do this, it was necessary to overturn one of the two curves). This test was necessary to verify the actual symmetry of the structure made in Geant4 and you can see an example in figure 4.10.

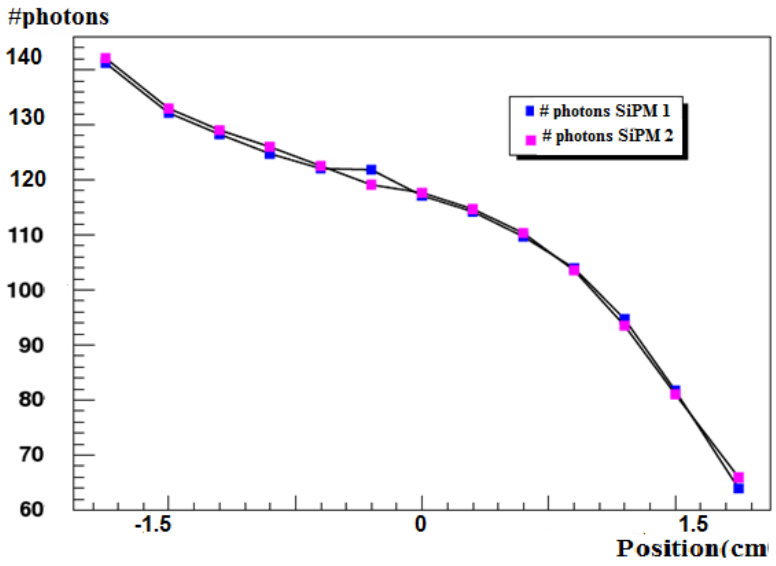

Figure 4.10: photons distribution simulation as a function of beam position in this case equal to 5 MeV, pointed in the CLOSE position(near SiPM)

4.2.1.b) Calculation of the charge barycentre

In a second phase, after having verifed the symmetrical behavior of the scintillator and considering it coupled to two SiPMs mounted in opposition, I simulated the behavior of the monitor by simultaneously acquiring the counts on both photomultipliers for the different energies of table 3.2 and in the different positions of Figure 4.4, in order to go back to the position of the energy release, with the calculation of the charge barycentre.

The reconstruction of the track position (example in figure 4.11) is obtained by comparing the amplitude of the signal acquired by the two SiPMs, in particular, the algorithm used is the weighted average of the signal amplitude between detectors:

$$Xrec = (w_1X_1 + w_2X_2+\ldots) / (w_1 + w_2+\ldots) \quad \text{(formula 1)}$$

where X_i are the nominal positions of each SiPM and wi is the pulse height . This formula is valid assuming that the height of the pulse w_i is proportional to

the photons path inside the scintillators, which is proportional to the energy deposited by the incident particle.

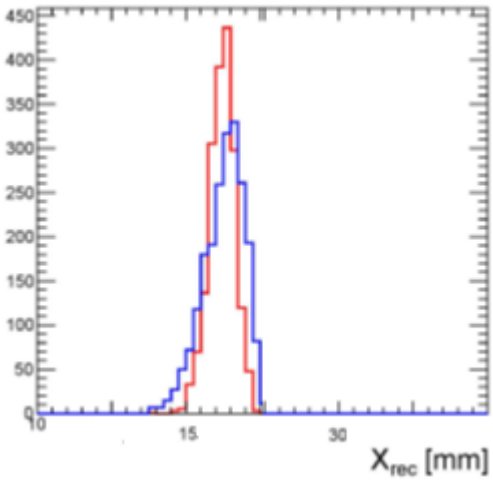

Figure 4.11: distribution of the reconstructed positions for events on two SiPMs in opposition:
The Xrec reconstructed position is reported taking the X axis origin in correlation of one of the external edges of the disk.

Other checks were carried out by placing at the ends of the scintillator further photomultipliers and performing new simulations in different points in order to increase the precision in the calculation of the barycentre, but at the expense of a further encumbrance which must be taken into account when mounting the beam monitor to the end of the SK beam pipe.

4.2.1.c) Reflectivity of the P-Terphenyl

Another of the parameters studied was the reflectivity of the P-Terphenyl disk walls: decreasing its value also reduces the number of photons that can reach the photocathode; this is explained by the fact that the decrease in reflectivity entails a lower number of photon reflections towards the interior and that is why they are lost because they exit the material before reaching SiPM (or being reabsorbed).

In this case, in figure 4.12, I reported an example of the tests made for a roughness value R equal to 0.005 of the scintillator disk (comparable to the parameter supplied by the manufacturer) and of reflectivity equal to 90%:

experimental tests allowed us to assign precise values to these parameters. We must recall that the roughness is a property of the surface of a body due of geometric micro imperfections normally present on the surface or even resulting from mechanical processing. In our case this parameter will characterize the surface of the scintillator. Reflectivity is a property of the material itself and it refers to the fraction of electromagnetic incident power that is reflected by an interface.

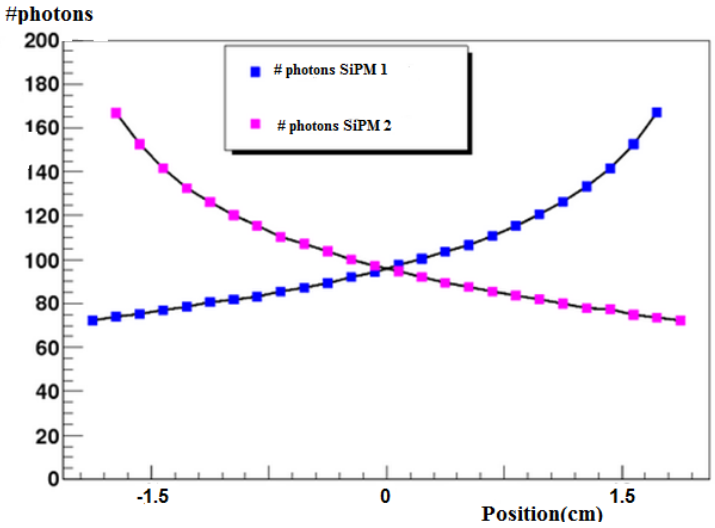

Figure 4.12: Number of photons revealed by two SiPMs as a function of the source position depending on the value of the roughness R=0.005 and reflectivity=90%.

4.2.2 Detector simulation

After a series of preliminary simulations, we moved on to the simulation of the monitor that will be inserted in the SK beam pipe, where we inserted the specific parameters of the p-terphenyl scintillator such as the attenuation length (1-1.5cm) and the light yeld (27000 photons/MeV).

For a more precise calculation of the barycentre, considering also the overall dimensions of the wiring, it was decided to exploit the p-terphenyl disk surface as much as possible using the largest number of photomultipliers, from 12 to 16 units.

The configurations used and which have been compared in order to have a better difference in the calculation of the barycentre position are summarized in table 4.1:

SiPM Position	N°SiPM	Thickness (mm)	Diameter (cm)
SIDE	12-16	1-2-3-4-5	2.6
UP	12-16	1-2-3-4-5	2.6

Table 4.1: Configurations and corresponding N° of SiPMs used in simulations, thicknesses and diameters of scintillators

In figure 4.13, instead, two possible configurations are drawn: a p-terphenyl disk coupled to 16 SiPMs placed on the top (UP configuration) and a p-terphenyl disk coupled again to 16 SiPMs but this time mounted on the edge of the disk (SIDE configuration).

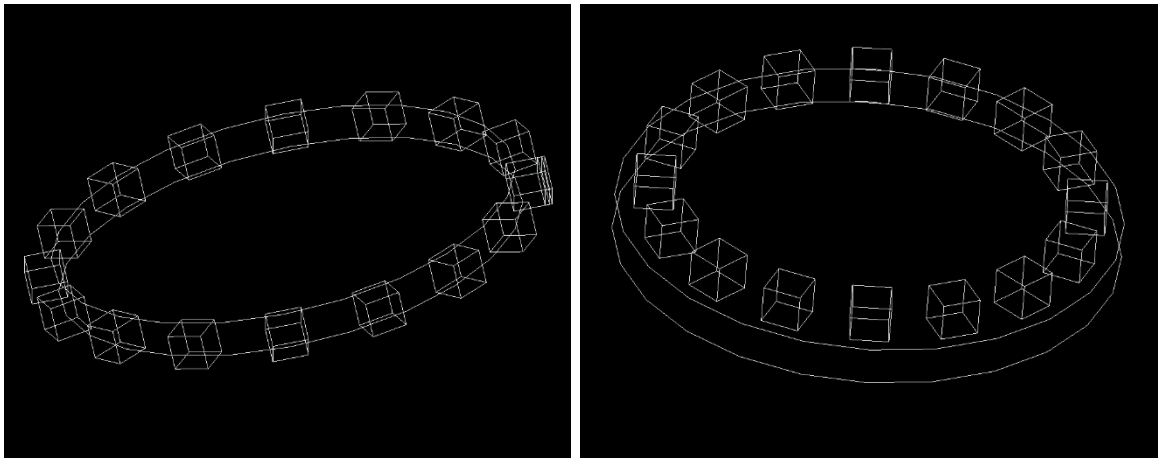

Figure 4.13

Configuration SIDE Configuration UP

Figure 4.14 shows one of the simulations carried out with 16 SiPMs in SIDE configuration, in figure 4.15 a simulations carried out with 16 SiPMs in UP configuration: it is possible to see the electron beam in RED, having in this case energy equal to 5 MeV and coordinates (0 cm, 0.8cm, -5cm) with respect to at

the origin of the Cartesian system corresponding to the center of the p-terphenyl disk.

Each SiPM represents a sensitive volume, within which a trace coming from the number of photon reflections within the scintillator could arrive and therefore be recorded.

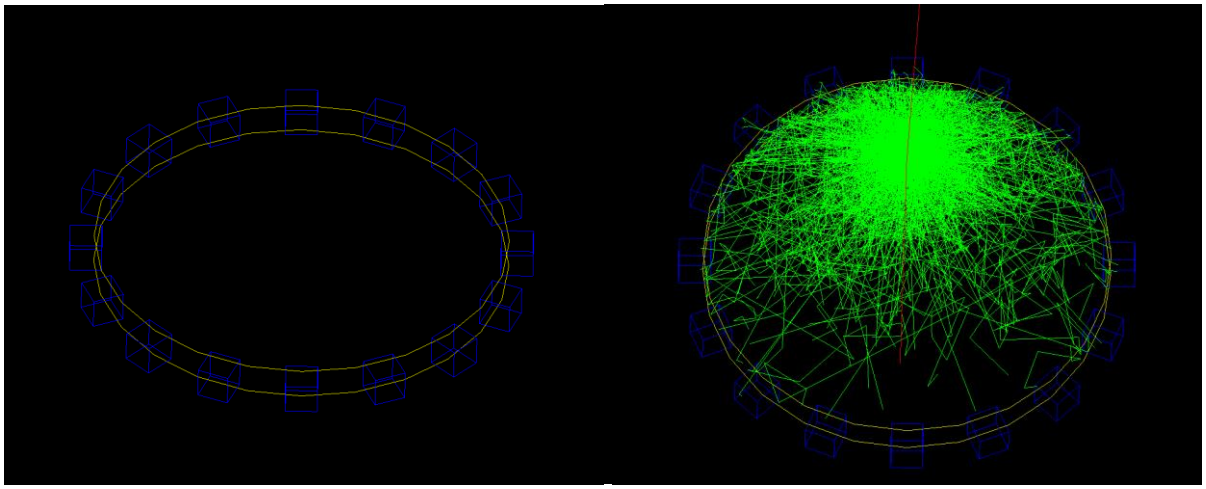

Figure 4.14 Visualization of scintillation photons collected by SiPMs (SIDE configuration)

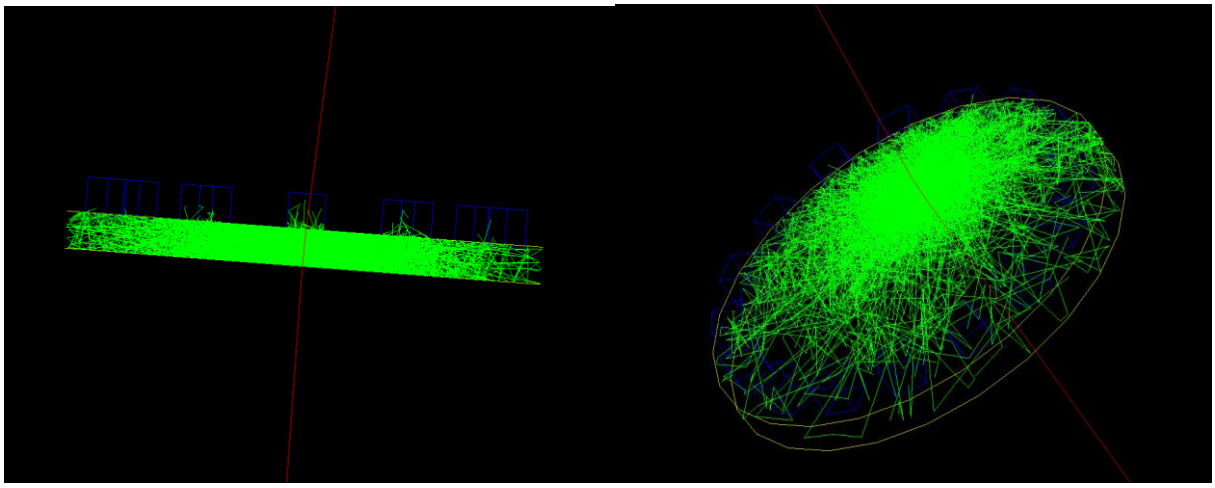

Figure 4.15 Visualization of scintillation photons collected by SiPMs (UP configuration)

I made a series of simulations like the ones in fig. 4.14 and 4.15, not only varying the number and position of the SiPMs (tab.4.1), but also varying the energy values and the beam position with respect to the origin of the Cartesian system corresponding to the center of the p-terphenyl disk, as shown in the following table 4.2:

SiPM Position	N°SiPM	Beam Energy (MeV)	Beam position (xmm,ymm)
SIDE	12-16	5-6-8-12-18	(0,0) (0,8) (8,0) (4,4)
UP	12-16	5-6-8-12-18	(0,0) (0,8) (8,0)(4,4)

Table 4.2: Configurations and corresponding N° of SiPMs used in simulations, thicknesses and diameters of scintillators

I analyzed the results coming from the simulation by using ROOT framework and for each simulation I created a plot like the one in figure 4.16 and 4.18 where it is possible visualize the number of scintillation photons recorded by each photomultiplier placed every 22.5°, considering the first SiPM at 0° corresponding to the position respect to the center of the p-terphenyl disk (11mm, 0mm).

Then, it was realized a histogram with the hits number depending on each SiPMs like in fig.4.17 and 4.19.

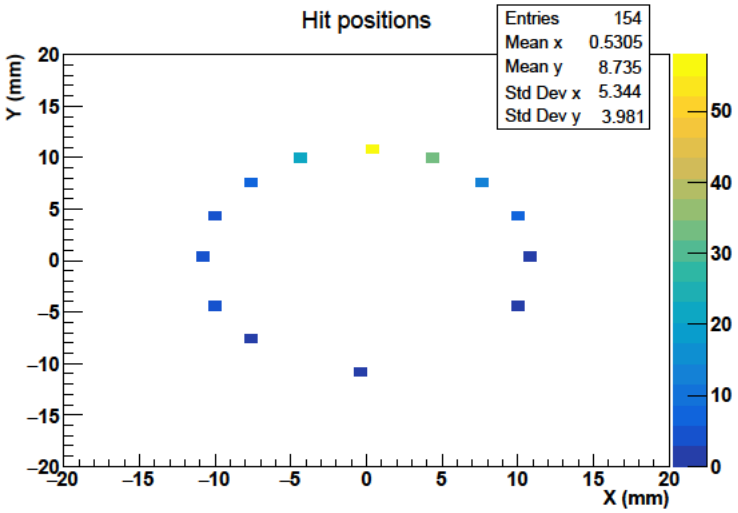

Figure 4.16 Two-dimensional plot of the number of scintillation photons recorded by each photomultiplier (UP configuration)

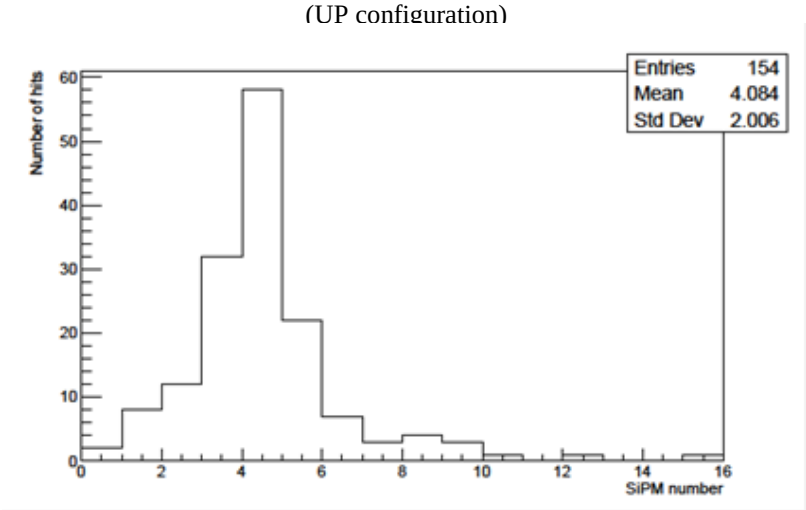

Figure 4.17 Histogram with #hits depending on each SiPMs (UP configuration)

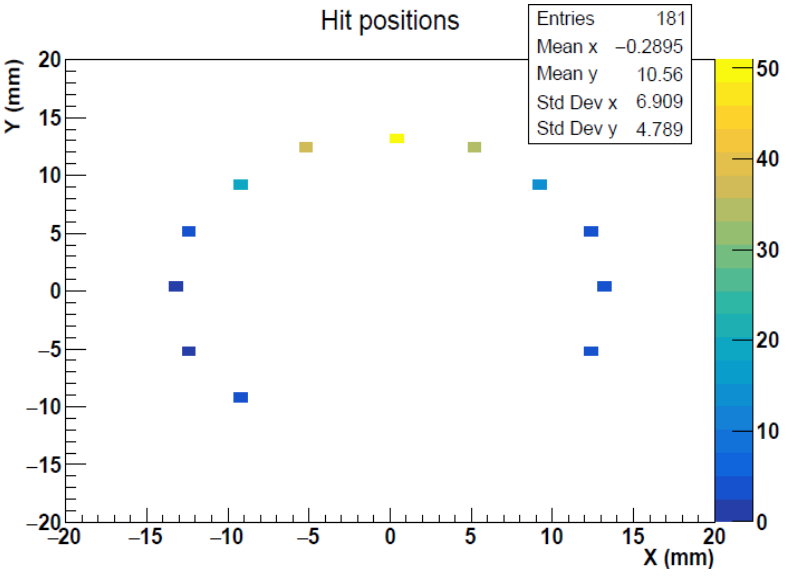

Figure 4.18 Two-dimensional plot of the number of scintillation photons recorded by each photomultiplier (SIDE configuration)

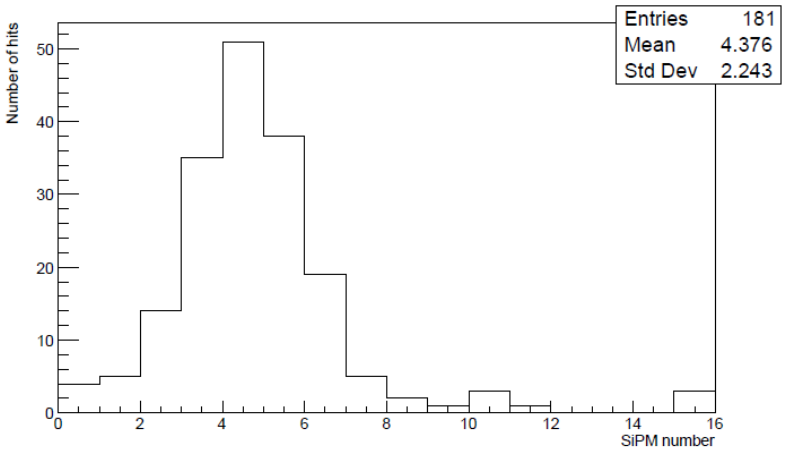

Figure 4.19 Histogram with #hits depending on each SiPMs (SIDE configuration)

With all the informations collected, I used formula (1) to reconstruct the beam position for each configuration for each configuration (UP and SIDE), for 12 or 16 SiPMs, each energy values and each beam position like in table 4.2.

Some examples are shown in figures 4.20, 4.21, 4.22.

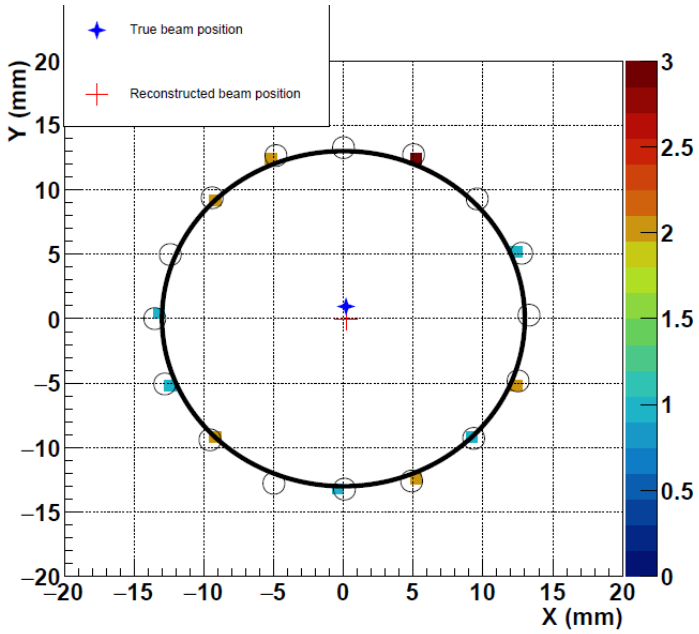

Figure 4.20 Plot related to a p-terphenyl disk with 16 SiPMs in SIDE configuration, with real beam position in (0,0) and position of the calculated barycentre

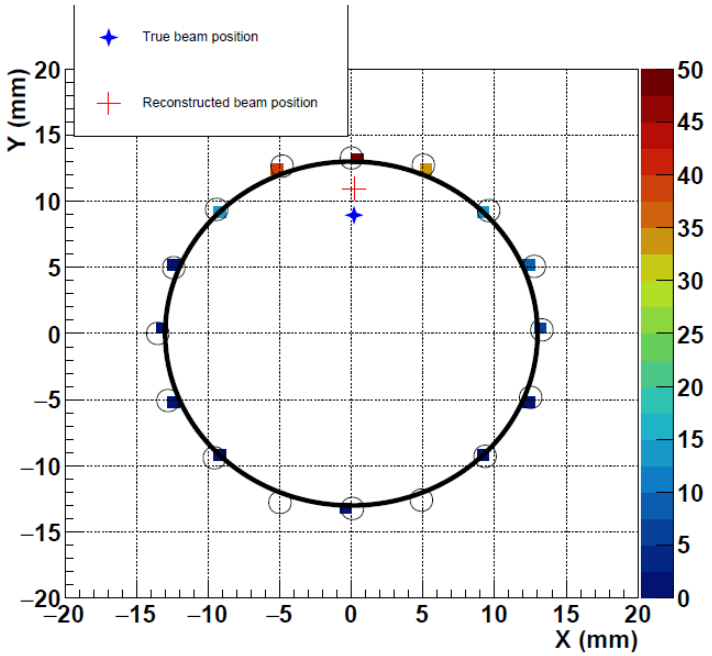

Figure 4.21 Plot related to a p-terphenyl disk with 16 SiPMs in SIDE configuration, with real beam position in (0mm,8mm) and position of the calculated barycentre

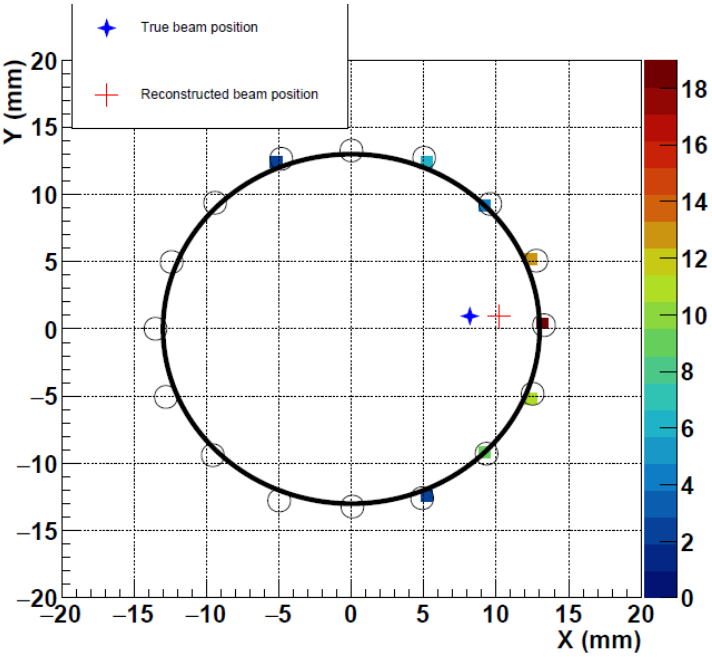

Figure 4.22 Plot related to a p-terphenyl disk with 16 SiPMs in SIDE configuration, with real beam position in (8mm,0mm) and position of the calculated barycentre

Finally, to evaluate the resolution on the beam position, 30 measurements were made for each configuration of table 4.2.

Thus, it was possible to evaluate the resolution on x and y (fig.4.23, 4.24, 4.25, 4.26) and the consequent the total resolution on the beam position for each configuration, calculated as standard deviation on 30 measurements.

In figures, the red line indicates the true value of the position of the beam inserted in Geant4.

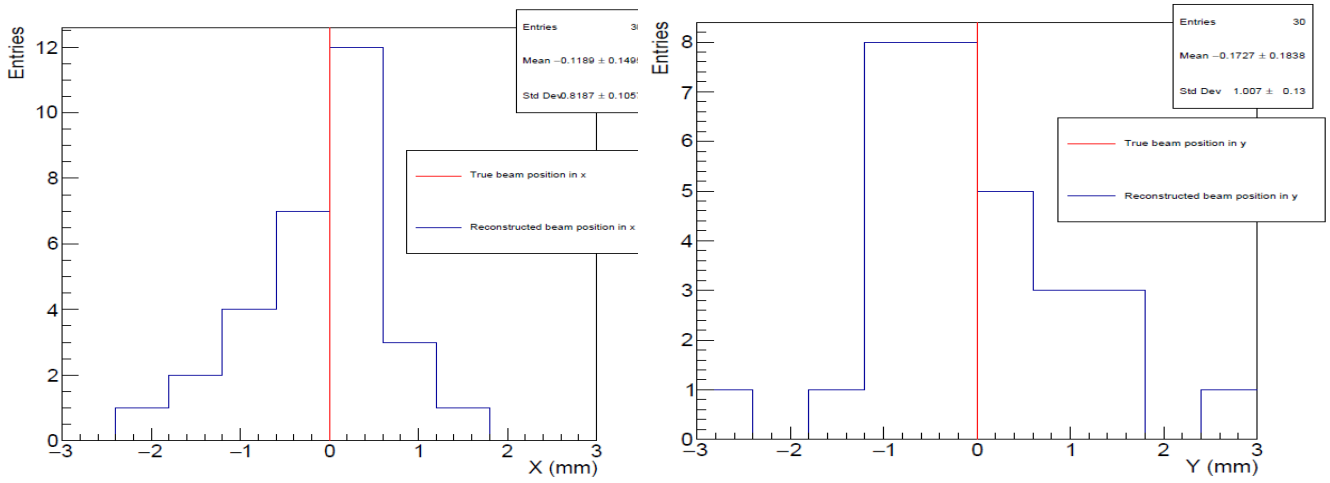

Figure 4.23 Example of histogram with reconstructed positions in x (left) and in y (right) after 30 measurements, configuration SIDE, with beam energy of 5 MeV, beam centered in (0,0).

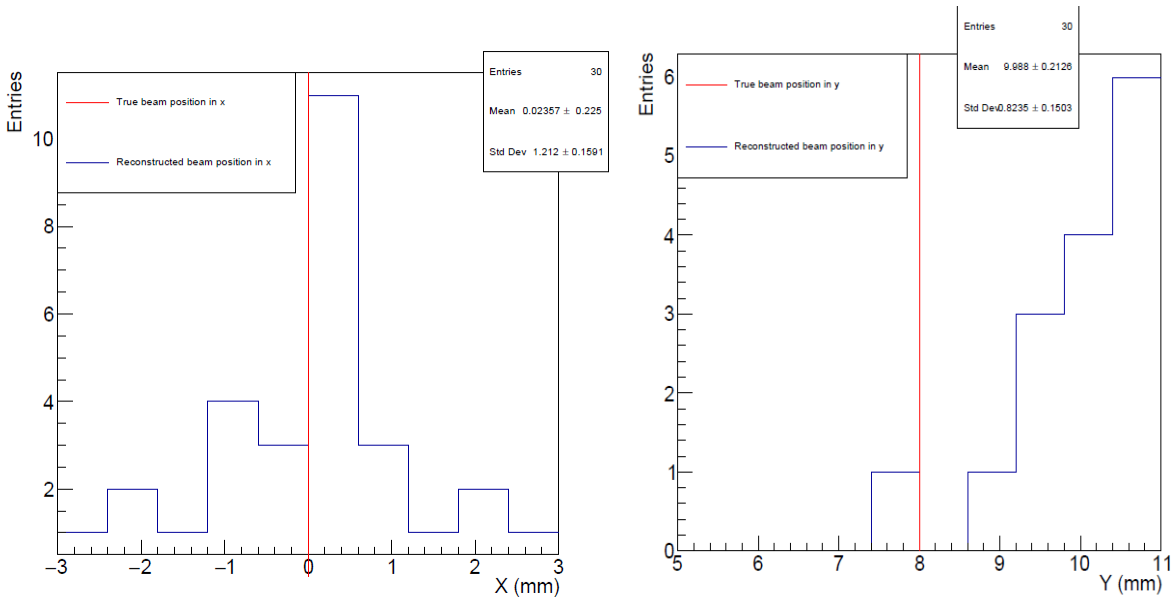

Figure 4.24 Example of histogram with reconstructed positions in x (left) and in y (right) after 30 measurements, configuration SIDE, with beam energy of 8 MeV, beam centered in (0,8).

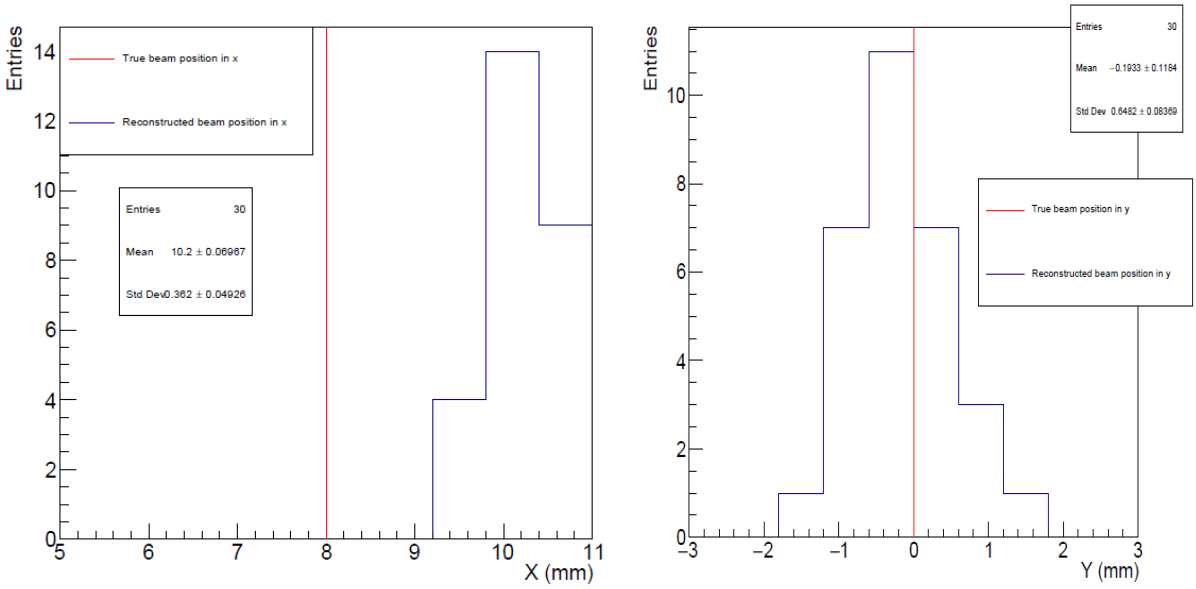

Figure 4.25 Example of histogram with reconstructed positions in x (left) and in y (right) after 30 measurements, configuration SIDE, with beam energy of 18 MeV, beam centered in (8,0).

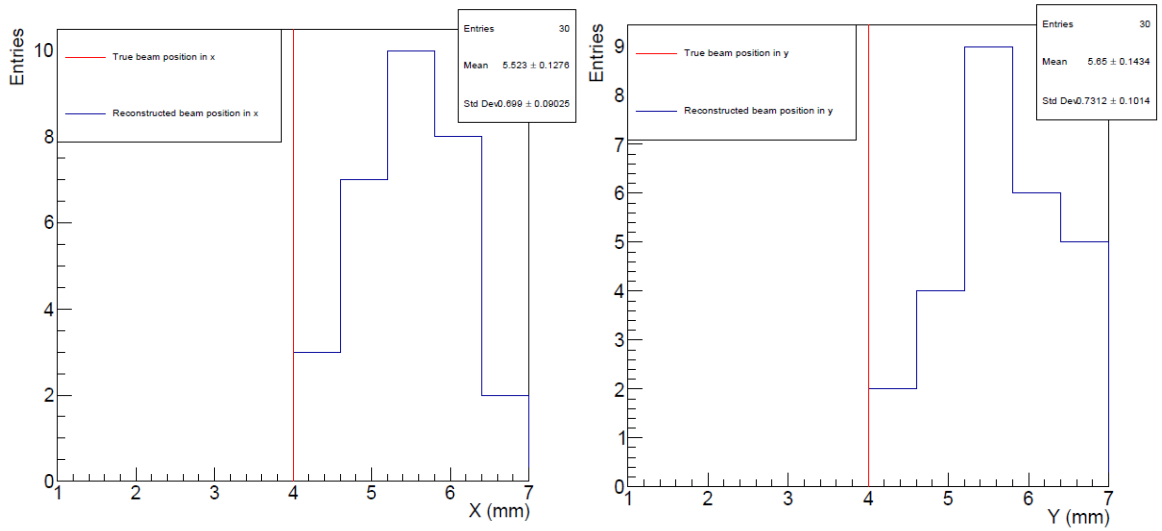

Figure 4.26 Example of histogram with reconstructed positions in x (left) and in y (right) after 30 measurements, configuration SIDE, with beam energy of 15 MeV, beam centered in (4,4).

All the results relating to the position of the resolution beam have been enclosed in the following tables: considering the two different configurations both for 12 (table 4.3 and 4.4) and for 16 SiPMs (table 4.5 and 4.6), based on the thickness of the scintillator, it was possible to derive the best configuration suitable for our purposes.

12 SiPMs (config. SIDE)	Beam energy 5MeV	Beam energy 6MeV	Beam energy 8MeV	Beam energy 12MeV	Beam energy 18MeV
Resolution on beam position (Thickness 1mm)	2.55±0.21mm	2.51.±0.25mm	2.35±0.74mm	2.37±0.42mm	2.25±0.08mm
Resolution on beam position (Thickness 2mm)	2.35±0.71mm	2.33.±0.35mm	2.33±0.04mm	2.27±0.17mm	2.23±0.15mm
Resolution on beam position (Thickness 3mm)	2.15±0.08mm	2.16.±0.05mm	2.15±0.11mm	2.09±0.24mm	2.10±0.08mm
Resolution on beam position (Thickness 4mm)	2.17±0.19mm	2.11.±0.15mm	2.15±0.29mm	2.12±0.38mm	2.11±0.44mm
Resolution on beam position (Thickness 5mm)	2.08±0.51mm	2.09.±0.65mm	2.09±0.69mm	1.99±0.45mm	1.98±0.33mm

Table 4.3: Resolution on beam position for 12 SiPMs (conf. SIDE) depending on the energy scale and thickness of scintillator (simulation values)

12 SiPMs (config. UP)	Beam energy 5MeV	Beam energy 6MeV	Beam energy 8MeV	Beam energy 12MeV	Beam energy 18MeV
Resolution on beam position (Thickness 1mm)	2.35±0.11mm	2.31.±0.15mm	2.25±0.09mm	2.22±0.27mm	2.18±0.17mm
Resolution on beam position (Thickness 2mm)	2.35±0.31mm	2.30.±0.25mm	2.32±0.16mm	2.29±0.77mm	2.28±0.57mm
Resolution on beam position (Thickness 3mm)	2.05±0.11mm	2.01.±0.58mm	2.05±0.52mm	2.00±0.22mm	2.01±0.03mm
Resolution on beam position (Thickness 4mm)	1.95±0.41mm	2.01.±0.20mm	2.01±0.44mm	1.97±0.28mm	1.85±0.03mm
Resolution on beam position (Thickness 5mm)	1.87±0.21mm	1.91.±0.05mm	1.25±0.79mm	1.73±0.49mm	1.75±0.38mm

Table 4.4: Resolution on beam position for 12 SiPMs (conf. UP) depending on the energy scale and thickness of scintillator (simulation values)

16 SiPMs (config. SIDE)	**Beam energy 5MeV**	**Beam energy 6MeV**	**Beam energy 8MeV**	**Beam energy 12MeV**	**Beam energy 18MeV**
Resolution on beam position (Thickness 1mm)	1.75±0.16mm	1.76.±0.25mm	1.72±0.39mm	1.52±0.09mm	1.58±0.22mm
Resolution on beam position (Thickness 2mm)	1.76±0.03mm	1.76.±0.45mm	1.74±0.13mm	1.72±0.32mm	1.68±0.12mm
Resolution on beam position (Thickness 3mm)	1.66±0.39mm	1.66.±0.52mm	1.67±0.40mm	1.62±0.12mm	1.58±0.20mm
Resolution on beam position (Thickness 4mm)	1.46±0.21mm	1.46.±0.17mm	1.44±0.65mm	1.42±0.44mm	1.38±0.22mm
Resolution on beam position (Thickness 5mm)	1.26±0.33mm	1.19.±0.45mm	1.18±0.09mm	1.23±0.02mm	1.18±0.12mm

Table 4.5: Resolution on beam position for 16 SiPMs (conf. SIDE) depending on the energy scale and thickness of scintillator (simulation values)

16 SiPMs (config. UP)	**Beam energy 5MeV**	**Beam energy 6MeV**	**Beam energy 8MeV**	**Beam energy 12MeV**	**Beam energy 18MeV**
Resolution on beam position (Thickness 1mm)	1.56±0.49mm	1.59.±0.76mm	1.58±0.73mm	1.53±0.22mm	1.48±0.37mm
Resolution on beam position (Thickness 2mm)	1.47±0.33mm	1.44.±0.52mm	1.48±0.43mm	1.43±0.72mm	1.38±0.16mm
Resolution on beam position (Thickness 3mm)	1.33±0.26mm	1.29.±0.45mm	1.28±0.09mm	1.27±0.66mm	1.18±0.32mm
Resolution on beam position (Thickness 4mm)	1.17±0.27mm	1.19.±0.45mm	1.18±0.19mm	1.13±0.02mm	1.13±0.12mm
Resolution on beam position (Thickness 5mm)	1.01±0.13mm	1.11.±0.45mm	1.1±0.15mm	0.95±0.22mm	0.94±0.19mm

Table 4.6: Resolution on beam position for 16 SiPMs (conf. UP) depending on the energy scale and thickness of scintillator (simulation values)

In fact, from the comparison between all the simulations carried out with thicknesses of different scintillators, different number of SiPMs placed in different positions, occurred that the best configuration is that of a 5mm-thick p-terphenyl disk, diameter of 2.6cm and with 16 SiPMs (UP) because in this case the calculation of the barycentre returns a error on the beam position of about 1mm.

In conclusion, the results obtained are more than satisfactory for the realization of a sequence of beam detectors capable of measuring the position of the beam profile with precision greater than the current one, allowing, moreover, to considerably shorten the time required for the alignment of the same.

Conclusion

The aim of this campaign of experimental measures and simulations was essentially to verify that, using a P-Terphenyl scintillator, the collection of light is sufficient for our purposes and that the attenuation length is of the same order of magnitude as the dimension of the monitor that will soon be installed on the SK.

This work has been divided into several phases. The first phase involved data analysis of the current calibration campaign which I took part in Super-Kamiokande, while in a second phase, after estimating the attenuation length in p-terphenyl after a series of measurements, I developed a simulation of the beam monitor system using the GEANT4 software developing a structure made of a P-Terphenyl scintillator connected first with one and then two and several SiPMs connected to its ends. An electron source, positioned along the scintillator, allowed us to acquire the data related to the photons of scintillation recorded by the photomultipliers.

We can conclude by highlighting how the studies carried out during the PhD thesis period allowing us to effectively characterize the behavior of a demonstrator that can be useful in the future for the realization of a set of 3 beam monitor used with the LINAC for the Super-Kamiokande calibration.

The optimal parameters for the scintillator and SiPMs have been chosen and the best configuration is made of a monocrystal P-Terphenil disk with a thickness of 5mm, a diameter of 2.6cm and 16 SiPMs in configuration UP: the position error is ~ 1mm.

This geometry will be optimal for our purposes and it will be possible to proceed with the assembly of the first detector which will also be used as a prototype for the next two monitors.

Bibliography

[1] E. Fermi, Zeitschr. f. Phys. 88 (1934) 161.

[2] F. Reines and C. L. Cowan, The neutrino, Nature, vol. 178, 446–449. .

[3] Bruno Pontecorvo. Mesonium and antimesonium. Zhur. Eksptl

[4] Ziro Maki, Masami Nakagawa, and Shoichi Sakata. Remarks on the unified model of elementary particles. Progress of Theoretical Physics, 28(5):870-880, 1962.

[5] Y. Fukuda et al. Evidence for oscillation of atmospheric neutrinos. Physical Review Letters.

[6] SNO Collaboration. Interactions Produced by B 8 Solar Neutrinos at the Sudbury Neutrino Observatory. Physical Review Letters, 87(7):071301, 2001

[7] P.W. Higgs. Broken symmetries, massless particles and gauge fields. Phys. Lett, 12(132), 1964.

[8] F. Englert and R. Brout. Broken symmetry and the mass of gauge vector mesons. Phys. Rev. Lett., 13(321), 1964.

[9] Ziro Maki, Masami Nakagawa, and Shoichi Sakata. “Remarks on the unified model of elementary particles”. In: Prog.Theor.Phys. 28 (1962), pp. 870–880. doi: 10.1143/PTP.28.870

[10] Y. Fukuda et al. (Super-Kamiokande collaboration), “Evidence for oscillation of atmospheric neutrinos”, Phys.Rev.Lett. vol. 81 pp. 1562–1567 (1998), doi:10.1103/PhysRevLett.81.1562

[11] Q.R. Ahmad et al. (SNO collaboration), “Direct evidence for neutrino flavor transformation from neutral current interactions in the Sudbury Neutrino Observatory”, Phys.Rev.Lett. vol. 89 p. 011301 (2002), doi:10.1103/PhysRevLett.89.011301

[12] K. Eguchi et al. (KamLAND collaboration), “First results from KamLAND: Evidence for reactor anti-neutrino disappearance”, Phys.Rev.Lett. vol. 90 p. 021802 (2003), doi:10.1103/PhysRevLett.90.021802

[13] F.P. An et al. (DAYA-BAY collaboration), “Observation of electron-antineutrino disappearance at Daya Bay”, Phys.Rev.Lett. vol. 108 p. 171803 (2012), doi:10.1103/PhysRevLett.108.171803

[14] K. Abe et al. (T2K collaboration), “Observation of Electron Neutrino Appearance in a Muon Neutrino Beam”, Phys.Rev.Lett. vol. 112 p. 061802 (2014), doi:10.1103/PhysRevLett.112.061802, 1311.4750

[15] Lincoln Wolfenstein. Neutrino oscillations in matter. Physical Review D, 17(9):2369, 1978.

[16] Raymond Davis Jr, Don S Harmer, and Kenneth C Hoffman. Search for neutrinos from the sun. Physical Review Letters, 20(21):1205, 1968.

[17] SAGE Collaboration. Measurement of the solar neutrino capture rate with gallium metal. Physical Review C, 60(5):055801, 1999.

[18] GALLEX Collaboration. GALLEX solar neutrino observations: Complete results for GALLEX II. Physics Letters B, 357(1):237-247, 1995.

[19] Y Fukuda, T Hayakawa, E Ichihara, K Inoue, K Ishihara, H Ishino, Y Itow, T Kajita, J Kameda, S Kasuga, et al. Evidence for oscillation of atmospheric neutrinos. Physical Review Letters, 81(8):1562, 1998.

[20] SNO Collaboration. Measurement of the Rate of νe+ d p+ p+ e- Interactions Produced by B 8 Solar Neutrinos at the Sudbury Neutrino Observatory. Physical Review Letters, 87(7):071301, 2001.

[21] M. H. Pinsonneault J. N. Bahcall and S. Basu. Solar models: current epoch and time dependences, neutrinos, and helioseismological properties. The Astrophysical Journal, 555(p.990-1012), 2001. (Cited on page 32.)

[22] MINOS Collaboration. Measurements of atmospheric neutrinos and antineutrinos in the MINOS far detector. Physical Review D, 86(5):052007, 2012.

[23]Proc Jpn Acad Ser B Phys Biol Sci. 2010 Apr; 86(4): 303–321. Atmospheric neutrinos and discovery of neutrino oscillations Takaaki Kajita et al.

[24]NOvA Collaboration. NOvA proposal to build a 30 kiloton o-axis detector to study neutrino oscillations in the fermilab NuMI beamline. arXiv preprint hep-ex/0503053, 2005.

[25] Hyper-Kamiokande Proto-Collaboration. Physics Potential of a Long Baseline Neutrino Oscillation Experiment Using J-PARC Neutrino Beam and Hyper-Kamiokande. arXiv preprint arXiv:1502.05199, 2015.

[26] Matthew Bass, Daniel Cherdack, and Robert J Wilson. Future Neutrino Oscillation Sensitivities for LBNE. arXiv preprint arXiv:1310.6812, 2013. LBNE is the predecessor of DUNE.

[27] K. Abe et al. (T2K Collaboration), "The T2K Experiment", Nucl. Instrum. Meth. A 659, 106 (2011), doi:10.1016/j.nima.2011.06.067

[28] S. Ahn et al. Detection of accelerator produced neutrinos at a distance of 250-km. Phys. Lett. B511 178–184 (2001).

[29] M. H. Ahn et al., Phys. Rev. D74, 072003 (2006).

[30] Y. Itow et al., (2001), hep-ex/0106019.

[31] R. Claus et al., Nucl. Instrum. Meth. A261, 540 (1987).

[32] "Y. Fukuda et al. "The Super-Kamiokande detector". Nucl. Instrum. Meth., A501:418–462, 2003.

[33] T. Tanimori et al., IEEE Trans.Nucl.Sci. 36, 497 (1989).

[34] A. Dziewonski and D. Anderson, Phys.Earth Planet.Interiors 25, 297 (1981).

[35] H. Ikeda et al. Front end hybrid circuit for super-kamiokande. Nucl. Instrum. Meth. A, 1992..

[36] Y. Fukuda, et al. Nuclear Instruments and Methods in Physics Research A501 418 (2003).

[37] K. Abe et al. "Calibration of the Super-Kamiokande Detector". Nucl. Instrum. Meth., A737:253–272, 2014.

[38] "Solar Neutrino Measurements in Super–Kamiokande–IV" K. Abe,1, et al.

[39] Calibration of Super-Kamiokande using an electron LINACM. Nakahata et al. /Nucl. Instr. and Meth. in Phys. Res. A 421 (1999)

[40] Super-Kamiokande collaboration, hep-ex/9805021(accepted for publication in Physical Review Letters).

[41]GEANT Detector Description and Simulation Tool, CERN Program Library W5013 (1994).

[42] Paul Papacz. Optimisation of the Particle Detection Efficiency for Scintillation Detectors with SiPM Readout. March 2010.

[43] Properties of para-terphenyl as detector for and α,β,γ radiation. physics.ins-det].2 May 2013 M. Angelonea, et al.